DISSERTATIONES
CHIMICAE
UNIVERSITATIS
TARTUENSIS
227

YOGESH KUMAR

$M\text{-}N_4$ macrocycle-based catalysts for electrocatalysis of oxygen reduction and oxygen evolution

DISSERTATIONES CHIMICAE UNIVERSITATIS TARTUENSIS
227

DISSERTATIONES CHIMICAE UNIVERSITATIS TARTUENSIS
227

YOGESH KUMAR

M-N_4 macrocycle-based catalysts for electrocatalysis of oxygen reduction and oxygen evolution

UNIVERSITY OF TARTU
Press
1632

Institute of Chemistry, Faculty of Science and Technology, University of Tartu, Estonia

The dissertation is accepted for the commencement of the degree of *Doctor Philosophiae* in Chemistry on 6 November 2023 by the Council of Institute of Chemistry, Faculty of Science and Technology, University of Tartu.

Supervisors: Prof. Kaido Tammeveski
Institute of Chemistry, University of Tartu, Estonia

Dr. Elo Kibena-Põldsepp
Institute of Chemistry, University of Tartu, Estonia

Dr. Srinu Akula
Institute of Chemistry, University of Tartu, Estonia

Opponent: Dr. Justus Masa
Max Planck Institute for Chemical Energy Conversion, Germany

Commencement: 21 December 2023 at 10:15 Ravila 14A-1020, Tartu (Chemicum) and Microsoft Teams (*online*)

This work has been partially supported by ASTRA project PER ASPERA Graduate School of Functional Materials and Technologies receiving funding from the European Regional Development Fund under project in University of Tartu, Estonia

ISSN 1406-0299 (print)
ISBN 978-9916-27-411-8 (print)
ISSN 2806-2159 (pdf)
ISBN 978-9916-27-412-5 (pdf)

University of Tartu Press
www.tyk.ee

TABLE OF CONTENTS

1. LIST OF ORIGINAL PUBLICATIONS

This thesis consists of six original articles listed below. The articles are referred in the text by Roman numerals I–VI.

I **Y. Kumar**, E. Kibena-Põldsepp, J. Kozlova, A. Kikas, M. Käärik, J. Aruväli, V. Kisand, J. Leis, A. Tamm, K. Tammeveski, Bimetal phthalocyanine-modified carbon nanotube-based bifunctional catalysts for zinc-air batteries. *ChemElectroChem* 8 (2021) 2662–2670.

II **Y. Kumar**, E. Kibena-Põldsepp, J. Kozlova, M. Rähn, A. Treshchalov, A. Kikas, V. Kisand, J. Aruväli, A. Tamm, J.C. Douglin, S.J. Folkman, I. Gelmetti, F.A. Garcés-Pineda, J.R. Galán-Mascarós, D.R. Dekel, K. Tammeveski, Bifunctional oxygen electrocatalysis on mixed metal phthalocyanine-modified carbon nanotubes prepared via pyrolysis. *ACS Applied Materials & Interfaces* 13 (2021) 41507–41516.

III **Y. Kumar**, E. Kibena-Põldsepp, M. Mooste, J. Kozlova, A. Kikas, J. Aruväli, M. Käärik, V. Kisand, J. Leis, A. Tamm, S. Holdcroft, J. H. Zagal, K. Tammeveski, Iron and nickel phthalocyanine-modified nanocarbon materials as cathode catalysts for anion-exchange membrane fuel cells and zinc-air batteries, *ChemElectroChem 9* (2022) e202200717.

IV **Y. Kumar**, E. Kibena-Põldsepp, S. Akula, J. Kozlova, A. Kikas, J. Aruväli, V. Kisand, K. Kukli, K. Tammeveski, The effect of additional nitrogen source on iron phthalocyanine-based catalysts for oxygen reduction reaction in acidic media. *Electrochemistry Communications* (2023, accepted)

V **Y. Kumar**, S. Akula, E. Kibena-Põldsepp, M. Käärik, J. Kozlova, A. Kikas, J. Aruväli, V. Kisand, J. Leis, A. Tamm, K. Tammeveski, Cobalt phthalocyanine-doped polymer-based electrocatalyst for rechargeable zinc-air batteries, *Materials* 16 (2023) 5105.

VI **Y. Kumar**, S. Akula, J. Kozlova, A. Kikas, J. Aruväli, M. Käärik, A. Treshchalov, J. Leis, V. Kisand, K. Kukli, E. Kibena-Põldsepp, K. Tammeveski, Zinc-assisted synthesis of polymer framework-based atomically dispersed bimetal catalysts for efficient oxygen electrocatalysis in rechargeable zinc-air batteries. (Manuscript submitted)

Author's contribution

Article I The author was responsible for the synthesis of catalysts, performed all electrochemical measurements and data analysis. The author is responsible for the interpretation of all testing results and primarily responsible for writing the manuscript.

Article II	The author was responsible for the synthesis of catalysts, performed all electrochemical measurements (except fuel cell and electrolyser experiments) and data analysis. The author is responsible for the interpretation of all testing results and primarily responsible for writing the manuscript.
Article III	The author was responsible for the synthesis of catalysts, performed all electrochemical measurements (except fuel cell experiments) and data analysis. The author is responsible for the interpretation of all testing results and primarily responsible for writing the manuscript.
Article IV	The author was responsible for the synthesis of catalysts, performed all electrochemical measurements and data analysis. The author is responsible for the interpretation of all testing results and primarily responsible for writing the manuscript.
Article V	The author was responsible for the synthesis of catalysts, performed all electrochemical measurements and data analysis. The author is responsible for the interpretation of all testing results and primarily responsible for writing the manuscript.
Article VI	The author was responsible for the synthesis of catalysts, performed all electrochemical measurements and data analysis. The author is responsible for the interpretation of all testing results and primarily responsible for writing the manuscript.

2. ABBREVIATIONS AND SYMBOLS

ADT	accelerated degradation test
AEM	anion exchange membrane
AEMEL	anion exchange membrane electrolyser
AEMFC	anion exchange membrane fuel cell
BET	Brunauer-Emmett-Teller
BF	bright field
CCL	cathode catalyst layer
CCM	catalyst-coated membrane
CDC	carbide-derived carbon
CoPc	cobalt phthalocyanine
CNTs	carbon nanotubes
CV	cyclic voltammetry
C_0	concentration of oxygen in the bulk solution
D_0	diffusion coefficient of oxygen
DCDA	dicyandiamide
E	electrode potential
E^0	standard potential
$E_{1/2}$	half-wave potential
E_{onset}	onset potential
$E_{j=10}$	potential required to reach 10 mA cm^{-2}
EDX	energy-dispersive X-ray spectroscopy
F	Faraday constant
FC	fuel cell
FePc	iron phthalocyanine
G	graphene
GC	glassy carbon
GDL	gas diffusion layer
HAADF	high-angle annular dark field
I	current
I_d	disk current
I_r	ring current
j	current density
j_d	diffusion-limited current density
j_k	kinetic current density
K-L	Koutecky-Levich
LSV	linear sweep voltammetry
MC	mesoporous carbon
MEA	membrane electrode assembly
M-N_x	metal-coordinated to nitrogen
M-N-C	metal-nitrogen-carbon
MPc	metal phthalocyanine
MnPc	manganese phthalocyanine

MOF	metal-organic framework
MWCNT	multiwalled carbon nanotube
N	collection efficiency of the ring electrode
n	number of electrons transferred per O_2 molecule
NiPc	nickel phthalocyanine
NPMC	non-precious metal catalyst
OCV	open circuit voltage
OER	oxygen evolution reaction
ORR	oxygen reduction reaction
PDF	phloroglucinol-dicyandiamide-formaldehyde
PFM	phloroglucinol-formaldehyde-methylimidazole
P_{max}	peak power density
PEM	proton exchange membrane
PEMFC	proton exchange membrane fuel cell
PGM	platinum-group metals
PSD	pore size distribution
RDE	rotating disk electrode
RHE	reversible hydrogen electrode
RRDE	rotating ring-disk electrode
RZAB	rechargeable zinc-air battery
S_{BET}	specific surface area
SCE	saturated calomel electrode
SEM	scanning electron microscopy
SHE	standard hydrogen electrode
STEM	scanning transmission electron microscopy
TEM	transmission electron microscopy
TM	transition metal
VC	Vulcan carbon
V_{μ}	micropore volume
V_{meso}	mesopore volume
V_{tot}	total pore volume
XPS	X-ray photoelectron spectroscopy
XRD	X-ray diffraction
v	kinematic viscosity of the solution
ω	rotation rate of the electrode
ZIF	zeolitic imidazolate framework

3. INTRODUCTION

In recent decades, the development of renewable energy storage and conversion devices has gained significant importance, primarily due to environmental concerns, the finite nature of fossil fuel resources and the escalating costs associated with fossil fuels. As per the findings of the International Energy Agency, global energy consumption continues to rise at an annual rate of approximately 1% [1,2]. A significant portion of this energy consumption is attributed to the transportation sector, which is swiftly emerging as the largest consumer of energy resources. Nevertheless, it is noteworthy that most energy utilised for transportation is still generated through the combustion of fossil fuels. However, many renewable energy sources, such as solar and wind, produce energy intermittently, highlighting the need for efficient energy storage solutions [3]. Among the array of alternatives, researchers are particularly inclined towards fuel cells (FCs) because of their impressive energy conversion capabilities and metal-air batteries are garnering attention for their sustainability and remarkable energy storage capacity [4,5]. One approach involves storing excess energy from the renewable energy sources in the form of chemical bonds, such as hydrogen (H_2) gas, which can later be converted into electric power using devices like FCs. These technologies are instrumental in meeting the growing energy demand. An added advantage of FCs over traditional batteries is their rapid refuelling capabilities, requiring only the replenishment of hydrogen or other suitable fuels. Within the realm of FCs, anion-exchange membrane fuel cells (AEMFCs) have gained attention due to their potential to use non-precious metal catalysts (NPMCs), particularly at the cathode [4]. This shift significantly reduces the cost of FCs in contrast to proton-exchange membrane fuel cells, which rely on costly Pt-based catalysts [6–8]. On the other hand, rechargeable zinc-air batteries (RZAB) offer an excellent alternative to lithium-ion batteries because of their high theoretical energy density (1086 Wh kg^{-1}), cost-effectiveness and inherent safety features [9]. In FCs, the oxygen reduction reaction (ORR) is a crucial electrochemical process, whereas in RZABs, both the ORR and the oxygen evolution reaction (OER) are pivotal processes [10,11]. However, the slow kinetics and substantial overpotential of the ORR and OER have a detrimental impact on overall efficiency, posing a significant challenge to the advancement of energy storage and conversion devices [12,13]. Platinum group metal (PGM)-based catalysts have been recognised for their efficiency in promoting the ORR and OER [14,15]. Nevertheless, their practical application is constrained by their limited availability, high cost and mediocre electrochemical stability.

Over the years, transition metal-based catalysts have emerged as promising nominees for oxygen electrocatalysis due to their exceptional electrocatalytic activity and stability in AEMFC and RZAB [9,12]. In this context, the discovery of M-N_4 macrocycle-based catalysts has opened exciting possibilities for advancing the field [16]. These macrocyclic structures with active centres,

composed of transition metal ions coordinated to four nitrogen atoms (N_4), have demonstrated remarkable electrocatalytic properties in various oxygen-related reactions [17,18]. They exhibit the potential to catalyse the ORR and OER with superior activity, selectivity and long-term stability, thus offering a pathway toward more efficient and sustainable energy conversion and storage technologies [19–23]. However, there are not many reports available for materials prepared from M-N_4 macrocycles for bifunctional electrocatalysts for the ORR and OER.

The aim of this PhD thesis was to investigate the electrocatalytic performance of various materials, including bimetal-doped carbon nanotubes [I,II], metal phthalocyanine-doped catalysts on different carbon supports [III,IV] and transition metal-doped carbon materials derived from polymer frameworks [V,VI], specifically for the ORR and OER application. The principal objectives included the development of improved catalysts based on these materials and the establishment of structure-property relationships. This research, spanning from the synthesis of novel catalyst materials to the comprehensive analysis of their electrochemical behaviour, aims to contribute to the dynamic field of electrocatalysis, with the aim of advancing sustainable energy technologies and reducing our dependence on fossil fuels.

4. LITERATURE OVERVIEW

4.1. Anion-exchange membrane fuel cells

A fuel cell (FC) serves as a device that directly transforms the chemical energy contained in fuel into electrical energy. There are numerous types of fuel cells with particular attention drawn to the H_2/O_2-fed FC due to its characteristics of low-temperature operation and a high energy-to-weight ratio [24]. Within the realm of hydrogen fuel cells, the proton exchange membrane fuel cell (PEMFC) has been extensively explored for decades, enjoying favourability when compared to the alkaline anion exchange membrane fuel cell (AEMFC) [25]. Currently, PEMFC is a mature technology, whereas AEMFC devices need further development [26–28]. PEMFCs capitalise on the enhanced diffusivity of protons (H^+) over hydroxide ions (OH^-), which translates into an advantage in achieving higher ionic conductivity [24]. However, PEMFCs face durability concerns, primarily arising from their acidic conditions, even when employing noble metal-based catalysts [29]. In contrast, AEMFCs operate in an alkaline environment, which facilitates the use of cost-effective non-noble metals and non-metal catalysts [4,10]. Studies have demonstrated that catalyst deactivation, particularly by the produced hydrogen peroxide (H_2O_2), is more pronounced in acidic media than in alkaline conditions [30]. Furthermore, unlike proton exchange membranes (PEM), anion exchange membranes (AEM) can be synthesised without the need for costly and toxic fluorinated compounds [31]. The oxygen reduction reaction (ORR) exhibits more favourable electrochemical kinetics in alkaline conditions, enabling a reduction in catalyst loading when utilising an alkaline medium [32]. Moreover, the alkaline environment is less corrosive, opening up possibilities for the application of a broader spectrum of non-noble metals for electrocatalysts [33,34]. These collective advantages position AEMFCs as a promising choice for various energy-related applications, making them a cost-effective, efficient and sustainable option in the realm of fuel cell technology [4,12,24,31].

In hydrogen fuel cells, H_2 serves as the fuel, while O_2 acts as the oxidising agent. Unlike PEMFCs, where H^+ ions are generated, AEMFCs produce OH^- ions and employ an AEM for OH^- ion transport. Practically, air is utilised as the source of O_2, but it necessitates purification due to potential impurities such as CO_2 and dust particles. This precaution is essential because CO_2 can neutralise the electrolyte (OH^-), resulting in the formation of weaker nucleophiles like carbonates and bicarbonates, consequently reducing the electrolyte concentration, deactivating the membrane and compromising cell performance [35–37]. However, the use of a solid alkaline-electrolyte membrane offers advantages of using NPMCs, excluding tolerance to CO_2 [38]. In an AEMFC, H_2 and O_2 are supplied at the anode and cathode sides, respectively. The schematic representation of an AEMFC is depicted in Figure 1. Electrochemical reactions occur at the triple-phase boundaries. In the presence of water, O_2 at the cathode undergoes reduction to produce OH^- ions, which then traverse the membrane to reach

the anode and engage in a reaction with H_2 to produce H_2O. This process leads to water consumption at the cathode and simultaneous water production at the anode. Therefore, maintaining proper water management is crucial to prevent cathode drying and anode flooding [39]. During the redox reaction, electrons generated at the anode are collected by the current collectors and conveyed to the cathode side through external circuits. The membrane is specifically chosen to enable the selective transport of OH^- ions.

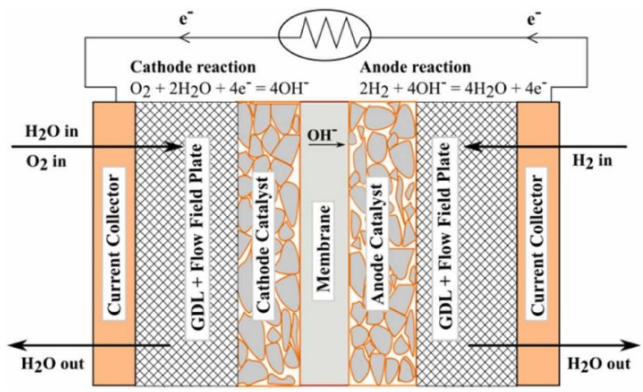

Figure 1. Schematic diagram of AEMFC [10].

4.2. Rechargeable zinc-air batteries

The origins of primary zinc-air batteries (PZAB) date back to the 1870s when the air cathode relied on an oxygen-consuming electrode, such as a silver wire [40]. This early electrode marked the beginning of catalytic "gas-diffusion electrodes" for ZAB. Later innovations, like the Walker-Wilkins battery, introduced a genuine gas diffusion electrode using porous carbon black [41]. In the 1930s, PZABs were commercialised and found applications in hearing aids during the 1970s [42,43]. However, the demand for rechargeable zinc-air batteries (RZABs) for hybrid/electric vehicles and power backups led to the upgrade of PZABs to meet these needs. Despite the advancements, RZABs face challenges, including low power density, limited cycling stability and poor discharge voltage plateaus, primarily due to the high overpotential on the air electrode [44]. This overpotential is influenced by the sluggish kinetics of the ORR/OER processes [45]. Consequently, there is a pressing need for cost-efficient, non-precious metal-based oxygen electrocatalysts to enhance ZAB performance [9,13,45]. Furthermore, distinct reaction mechanisms lead to differing requirements for the active sites in the ORR/OER processes. For instance, the OER activity is constrained by the HOO* and O* formation steps, while the ORR activity is limited by the OH* reduction step and O_2 reduction steps [46].

RZABs consist of various components (Figure 2): (i) the zinc (Zn) anode; (ii) the electrolyte that facilitates ion migration during charge-discharge cycles;

(iii) the separator, preventing physical crossover between the anode and cathode, while allowing the migration of charge-carrier ions; and (iv) the air electrode, functioning as the cathode for the O_2 electrochemistry, encompassing both ORR and OER. These reactions dictate the kinetics for discharge and charge processes. During discharge, the Zn anode undergoes oxidation to form soluble Zn hydroxides ($Zn(OH)_4^{2-}$ or zincate ions), which subsequently decompose into insoluble zinc oxide (ZnO). Conversely, at the cathode, O_2 from the atmosphere infiltrates the porous air electrode to participate in ORR. Upon charging, Zn is plated at the anode and OER occurs at the cathode. Due to the sluggish ORR and OER kinetics, there is a critical need for bifunctional air electrocatalysts that are both highly active and durable for O_2 electrochemistry. These efficient bifunctional electrocatalysts play a pivotal role in enhancing the performance, stability and recyclability of RZABs [9].

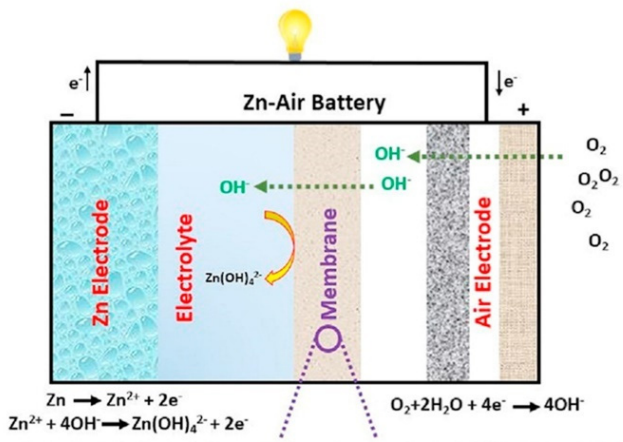

Figure 2. Schematic diagram of RZAB [47].

4.3. The oxygen reduction reaction

The electroreduction of oxygen is a crucial electrochemical reaction with wide-ranging significance. Beyond its role in generating energy through FCs and RZABs, this reaction is fundamental to biological respiration, sustaining life. It is worth noting that in alkaline conditions, the ORR can follow two distinct pathways. The direct 4-electron pathway:

$$O_2 + 2H_2O + 4e^- \rightarrow 4OH^- \qquad E_0 = 0.401\ \text{V} \qquad (1)$$

or 2-electron pathway:

$$O_2 + H_2O + 2e^- \rightarrow HO_2^- + OH^- \qquad E_0 = -0.065\ \text{V} \qquad (2)$$

followed by further reduction of hydroperoxide ion:

$$HO_2^- + H_2O + 2e^- \rightarrow 3OH^- \qquad E_0 = 0.867\ \text{V} \qquad (3)$$

With all the standard potential (E_0) values given versus the standard hydrogen electrode (SHE) at 25 °C.

The ORR stands as a fundamental electrochemical reaction in FCs, occurring at the cathode where atmospheric O_2 combines with H^+ ions and electrons (e^-) to form water (H_2O) [48]. It holds exceptional significance within fuel cells, as it profoundly influences their efficiency and overall performance. Enhanced ORR kinetics are imperative for sustaining a high FC voltage, a critical factor affecting the electrical power produced [12]. Sluggish ORR kinetics and the formation of HO_2^- can lead to voltage losses, thus diminishing the overall fuel cell efficiency [38]. Notably, in alkaline conditions, the chemisorption of O_2 faces hindrance due to specifically adsorbed OH^- ions [49]. Consequently, the initial ORR step may occur as an outer-sphere reaction, where O_2 is reduced to superoxide (O_2^-) anion [50]. This characteristic introduces a degree of flexibility to the surface on which this reduction reaction takes place, enabling a wider range of NPMCs in alkaline media compared to acidic ones [46,51]. The pursuit of enhanced ORR efficiency remains a pivotal element in the advancement of FC technology, propelling it towards a cleaner and more sustainable option for various applications, spanning electric vehicles to stationary power generation.

4.4. The oxygen evolution reaction

Commonly, the OER mechanisms are understood to proceed through two distinct pathways: the adsorbate evolution mechanism and the lattice-oxygen-mediated mechanism [52], as illustrated in Figure 3a and b, respectively. The adsorbate evolution mechanism generally involves a sequence of four co-ordinated proton-electron transfer reactions, centred around active metal sites [53]. As depicted in the Figure below, this process begins with the adsorption of a water molecule onto the metal (M) site through a one-electron oxidation step, leading to the formation of an adsorbed OH* on the M site [54]. Subsequently, OH* engages in proton coupling and electron removal, yielding O* species. The subsequent step involves the formation of an O-O bond, enabling O* to interact with another water molecule, ultimately producing HOO*. Finally, HOO* undergoes oxidation through a one-electron transfer process, liberating O_2 while restoring the initial M active site [51].

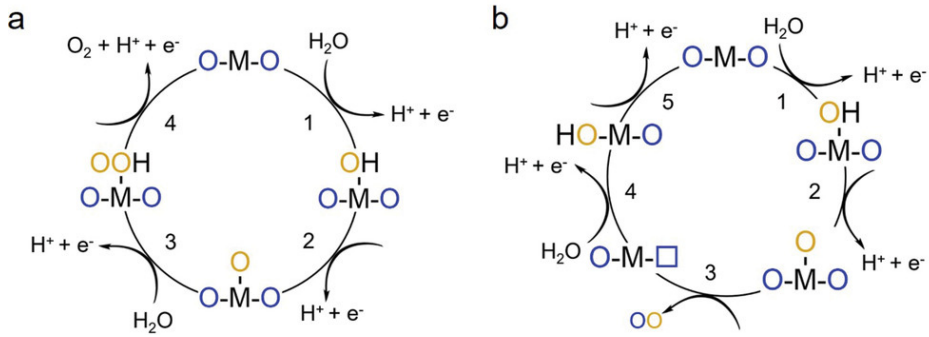

Figure 3. Proposed (a) adsorbate evolution mechanism and (b) lattice oxygen mechanism for OER [51].

The scaling relationship among the intermediates in the adsorbate evolution mechanism places a limit on OER, capping the theoretical overpotential at 0.37 V [51]. In contrast, the concept of the lattice-oxygen-mediated mechanism, in which lattice oxygen actively participates in the reaction, was initially proposed by Damjanovic and Jovanovic in 1976 [55]. In 2015, Binninger and colleagues provided a more comprehensive explanation, introducing the term "lattice oxygen evolution reaction" [56]. In the typical lattice-oxygen-mediated mechanism, the initial two steps mirror those of the adsorbate evolution mechanism, involving the creation of O*. Subsequently, O* interacts with the lattice oxygen to release O_2 molecules, simultaneously generating an oxygen vacancy within the lattice. The vacancy can then be refilled by the migration of OH^- ions from the solution. In the lattice-oxygen-mediated cycle, the limitation arising from the scaling relationship between OH* and HOO* can be circumvented, as HOO* does not form within this cycle [56].

4.5. Transition metal-based catalysts for ORR

As it is stated in the section 3, platinum-based catalysts are recognised as the most proficient electrocatalysts for the ORR. However, due to their prohibitive cost, limited availability and diminished stability, there is a pressing need to investigate more efficient and cost-effective alternatives among transition metal-based ORR catalysts. Over recent years, transition metal oxides, sulphides and transition metal-nitrogen-carbon (M-N-C) type catalysts have emerged as promising contenders to succeed Pt-based and other precious metal ORR electrocatalysts [57–61].

Transition metal oxides exhibit a notable trait in maintaining robust stability when exposed to acidic, alkaline and oxidising conditions. Moreover, they do possess some level of ORR activity in alkaline solutions. Nevertheless, there is an ongoing challenge associated with enhancing their ORR activity [62]. This lower ORR activity is primarily attributed to the inherent wide energy band of transition metal oxides, which results in reduced electrical conductivity and

limited capacity for adsorbing oxygen at their surfaces [63]. One effective strategy for enhancing the electrocatalytic ORR activity of transition metal oxides involve the introduction of defective structures into these materials. This approach entails modifying the coordination environment and electronic structure to induce a surface strain effect. This, in turn, optimises the adsorption energy of ORR intermediates on the catalyst's surface. As a result, Zhang and colleagues undertook the creation of manganese-deficient Mn_3O_4 by subjecting manganese glycolate to a calcination process [57]. The introduction of manganese defects in Mn_3O_4 instigated changes in its electronic structure, leading to improvements in electrical conductivity and electron delocalisation. The presence of these manganese defects significantly lowered the desorption energy of OH* and effectively reduced the change in Gibbs free energy and the theoretical overpotential during the rate-limiting step of the ORR [57]. Recently, in addition to single-component transition metal oxides, there has been a growing interest in cost-effective, NPMCs with structures such as perovskite (ABO_3) and spinel (AB_2O_4) mixed metal oxides [64,65]. Sun and collaborators employed a polyol-assisted solvothermal method to synthesise a range of $LaMn_xCo_{1-x}O_3$ (where x = 0, 0.25, 0.3, 0.35, 0.5, 1) electrocatalysts [58]. The $LaMn_{0.3}Co_{0.7}O_3$ electrocatalyst, optimised through this process, exhibited a significant enhancement in the half-wave potential ($E_{1/2}$) for ORR, surpassing the original $LaCoO_3$ catalyst by 0.72 V, representing a 52 mV improvement (from 0.67 V to 0.72 V) [58].

Transition metal sulphides represent a novel class of cluster crystals that originate from the interaction between metal and sulphur elements. These compounds offer a conducive environment for oxygen adsorption and electron transfer. The sulfidation of metals alters the surface chemistry of transition metal sulphides, preventing the oxidation of metal centres during electrocatalyst preparation, thereby enhancing their stability in comparison to metal oxides [59]. Furthermore, bimetallic sulphides exhibit elevated electrical conductivity and possess diverse valence states, endowing them with exceptional electrocatalytic capabilities [66].

Among the most promising catalysts are M-N-C materials, which have already demonstrated the ORR performance comparable to Pt/C catalysts. These electrocatalysts have emerged as viable alternatives due to their distinctive electronic characteristics and remarkable electrochemical stability [23,67–70]. To be more precise, the impressive electrocatalytic activity of M-N-C materials for ORR is believed to arise from the synergy of distinct active sites. This synergy encompasses (i) transition metal coordination with nitrogen [16,34,68, 69,71,72] and (ii) nitrogen functional groups, such as pyridinic-N and pyrrolic-N [73,74]. This enhanced activity is a consequence of the unique electronic structure of the metal centres, which facilitates the breaking of the O-O bond. Moreover, it involves the filled d_{xy} and d_{yz} orbitals, as well as the empty d_{z^2} orbitals, which form bonds with π*-electrons from O_2 molecules [75].

Various approaches exist for the synthesis of M-N-C type catalysts, with a particular focus on two methods: (i) one approach involves the combination of

transition metal and nitrogen-containing precursors through high-temperature pyrolysis, along with a carbon support and (ii) another method utilises transition metal macrocycles, such as metal porphyrins and phthalocyanines, as starting materials. First synthesis route can utilise various transition metal salts and nitrogen-rich sources, such as dicyandiamide, urea, melamine and others, as precursor materials [76–79]. For instance, in their work, Shang and colleagues employed manganese acetate as the precursor for Mn and utilised chitosan, a hydrophilic material rich in uncoordinated amino groups, as sources of nitrogen and carbon to create a Mn-N_2C_2-based electrocatalyst [61]. This carbon-based catalyst demonstrated excellent ORR properties in an alkaline environment, with onset potential (E_{onset}) and $E_{1/2}$ of 1.04 V and 0.915 V, respectively.

On the other hand, the coordination structure that arises from the central metal atom within metal phthalocyanine (MPc) molecules and the surrounding four nitrogen-containing groups is conventionally regarded as the active centre. The choice of the central coordination ion has a discernible impact on the catalytic performance of the phthalocyanine-based catalysts [80]. When comparing the half-wave potentials for ORR, it becomes apparent that the activity is influenced by the type of central ion, following the trend $Fe^{2+} > Co^{2+} > Mn^{2+} > Cu^{2+}$ [81]. This observation underscores the crucial role of transition metals in establishing the active sites responsible for facilitating the ORR. Notably, despite its effectiveness in forming active sites, Cu-N-C exhibits significantly lower ORR activity than Co-N-C and Fe-N-C catalysts [81]. In the research, the Dodelet group employed a direct heat-treatment process using precursor macrocycles containing M-N_4 sites, wherein they used carbon black impregnated with varying amounts of iron acetate as precursor materials [82]. This led to the creation of diverse nitrogen-coordinated iron species referred to as Fe-N_x moieties, which made a substantial contribution to enhancing the ORR electrocatalytic activity.

Moreover, bimetallic M-N-C catalysts for the ORR have emerged as a promising avenue of research in the field of electrocatalysis [83,84]. These catalysts combine the benefits of two different transition metals, enhancing their catalytic performance and stability. Bimetallic M-N-C catalysts typically consist of a combination of transition metals, such as Fe, Co or Mn, along with nitrogen atoms coordinated on a carbon support (Table 1). The synergy between these metals and the nitrogen-doped carbon matrix allows for a highly efficient electrochemical reduction of oxygen [85–87].

4.6. Transition metal-based catalysts for OER

Transition metal-based OER electrocatalysts can be mainly classified into transition metal (TM) oxides, sulphides and phosphides. Further, this selection can be divided into mono-metal and bimetal catalysts.

The OER activity of TM oxides significantly depends on factors like the type of metal, oxidation states and the support material. For instance, CoO_x catalysts have garnered substantial attention for OER, thanks to the mixed valence states

of Co cations, including +2, +3 and +4 [88]. Similarly, the investigation of iron-based oxides has shown promise as efficient OER electrocatalysts, as iron is one of the most abundant metallic elements on Earth [89]. Smith and colleagues adopted a photochemical metal-organic deposition technique to synthesise amorphous iron oxide (a-Fe_2O_3) and demonstrated its noteworthy OER electrocatalytic activity [90]. Moreover, manganese-based oxides can also be prepared and serve as excellent OER catalysts. Huynh et al. demonstrated that by employing a combination of treatments, manganese oxides with pedal- or plate-like morphology can undergo a transformation into an amorphous state, showcasing exceptional OER activity [91]. In the realm of NPMCs for OER, nickel oxide (NiO_x) stands out due to its favourable electronic configuration. It has been established that optimal OER activity can be achieved when the 3d electron e_g occupancy is close to unity [92]. For instance, Ni-based species with a valence state of +3 can serve as an ideal material for OER because of the favourable e_g configuration of Ni^{3+} ($t_{2g}^6e_g^1$). However, it is worth noting that Ni^{3+} exhibits limited stability. To enhance the catalytic activity of transition metal oxides, the utilisation of bimetallic oxides is particularly appealing due to their synergistic effects [93]. For example, Geng and co-workers introduced amorphous $Fe_6Ni_{10}O_x$ through an aerosol-spray-assisted method for the OER [94]. In a similar vein, Zhang et al. successfully synthesised amorphous $Fe_3Ni_7O_x$ [95]. The optimised $Fe_3Ni_7O_x$ material demonstrated exceptional OER performance, surpassing that of pure NiO_x or FeO_x. Furthermore, Guo et al. employed a straightforward hydrothermal approach to synthesise amorphous $CoMoO_x$ with a core-shell structure [96]. The inclusion of Co resulted in the catalyst displaying a reduced overpotential (340 mV at 10 mA cm^{-2}) for OER.

Similar to TM oxides, transition metal sulphides and phosphides also exhibit outstanding electrocatalytic activity for the OER. Notably, unlike metal oxide-based nanomaterials, metal sulphide materials often possess excellent electrical conductivity [97]. Currently, numerous researchers have highlighted that the structure of sulphide catalysts can be prone to instability and are susceptible to oxidation during the OER process in alkaline solutions, leading to their transformation into the corresponding oxide or (oxy)hydroxide [98–100]. Some scientists contend that the remaining sulphur can be incorporated into the metal (oxygen) hydroxide and theoretical calculations have supported this by demonstrating that sulphur doping reduces the energy barrier for each reaction step, thus facilitating the OER process [101]. In contrast, TM phosphides offer superior OER activity owing to the presence of lone pair electrons and vacancies in the 3p orbital. This unique configuration enables phosphorus atoms to form moderate bonds with reaction intermediates, making it easier for them to serve as proton or hydride acceptors on phosphide-based electrocatalysts [102]. As a result, TM phosphides exhibit exceptional activity when utilised as catalysts for water splitting, particularly in the context of the OER. Pyrolysis of macrocycles can also provide good OER active site due to some oxidation of metal site and degradation of macrocycles at high temperatures to form TM-oxides and metal nanoparticles.

4.7. Role of carbon supports

Carbon supports play a crucial role in the electrocatalysis of ORR and OER. Carbon supports serve as a platform for anchoring and supporting electrocatalytic materials, enhancing their performance in several ways:

(i) Catalyst immobilisation: carbon support provides a stable and conductive substrate for anchoring ORR- and OER-active sites. The carbon support prevents the aggregation and leaching of these active sites, ensuring long-term stability and activity [103].

(ii) Improved electron transport: carbon materials, especially highly conductive ones like carbon black, graphene or carbon nanotubes, facilitate the rapid transport of electrons between the catalyst and the electrode. This ensures efficient charge transfer during the ORR and OER processes, enhancing the overall electrocatalytic activity.

(iii) Enhanced mass transport: carbon supports often have porous structures that can improve the mass transport of reactants and products to and from the catalyst sites. This helps to maintain a high concentration of reactants at the catalyst's active sites, promoting more effective ORR and OER reactions [104].

(iv) Tuning of surface properties: carbon supports can be modified to control their textural properties. Functionalisation or doping of carbon materials with heteroatoms can influence the interaction between the catalyst and the reactants, improving electrocatalytic performance [105].

(v) Cost-effectiveness: carbon supports are relatively inexpensive, making them attractive for commercial electrocatalysis applications. They offer a cost-effective way to enhance the performance of catalyst materials.

4.8. AEMFCs using transition metal-based cathode catalysts

Firstly, anion exchange membranes (AEMs) play a vital role in AEMFCs as they facilitate the transfer of OH^- ions from the cathode to the anode. One of the primary advantages of using AEMs is the prevention of carbonate precipitates due to the absence of free cations and reduced gas crossover. Ionic conductivity within AEMs occurs through aqueous domains that surround the fixed cationic group. It was observed that while the ion exchange capacity and water uptake of AEMs and proton-exchange membranes (PEMs) were similar, AEMs exhibited lower conductivity compared to PEMs, possibly due to a higher activation energy [106]. AEMs typically incorporate various cationic groups, including quaternary ammonium, imidazolium, phosphonium, sulfonium and organic metal cation-based groups, with quaternary ammonium and imidazolium groups being prominent subjects of research [107–111]. Danks et al. employed a radiation grafting method to functionalise poly(vinylidene fluoride) and poly(tetrafluoroethylene-co-hexafluoropropylene) polymers with benzyl trimethyl ammonium groups, resulting in membranes for direct methanol fuel cells with a room

temperature conductivity of 20 mS cm^{-1} [112]. High stability in alkaline conditions has been achieved with side-chain-type poly(terphenylene)-based membranes and polyfluorene membranes [113]. Nucleophilic substitution was used to create side-chain-type 6-azaspiro[5.5]undecanium-poly(phenylene oxide), which exhibited remarkable stability (>1500 h) in an alkaline environment and a conductivity of 92 mS cm^{-1} [114]. Bauer et al. reported that quaternary ammonium groups displayed superior stability compared to phosphonium- and sulfonium-based groups [115]. A polysulfone AEM based on tris(2,4,6-trimethoxyphenyl) quaternary phosphonium exhibited a conductivity of 27 mS cm^{-1} at 20 °C. Methyl tris(2,4,6-triethylphenyl) phosphonium demonstrated over 5000 h of stability at 80 °C [116]. Kwasny and Tew conducted a study on AEMs containing metal cations, revealing that the metal ions did not significantly affect mechanical properties and water uptake while exhibiting excellent stability in alkaline environments [117]. Aemion+® developed by Holdcroft's group has shown promising results in AEMFC due to its improved chemical stability, water permeability and lower dimensional swelling [118]. Thinner membranes have lower ohmic resistance but may exhibit higher fuel and reactant crossover. Improving the molecular weight of the polymer can enhance the mechanical stability of polymeric membranes, reducing interfacial contact resistance due to the formation of thinner membranes [28].

While the AEMFC field has experienced significant growth in recent years, there is relatively less published data on NPMC materials employed as cathodes or anodes in AEMFCs than in PEMFCs. The ORR in alkaline conditions presents a more intricate picture than in acidic conditions due to the presence of both inner- and outer-sphere reactions [50]. This complexity, however, allows for a broader range of NPMCs to efficiently catalyse the ORR. Notably, the Pt group metal-free transition metal-nitrogen-carbon (M–N–C) catalysts (M = Fe, Co, Cu) have shown better ORR performance in alkaline media compared to acidic media [I-VI] [10,16,24]. The peak power density (P_{max}) of AEMFCs utilising Fe–N–C as cathode catalysts has seen substantial improvements, rising from 0.107 W cm^{-2} in 2015 to 1.44 W cm^{-2} in 2020 [4,119]. Studies by Ren et al. revealed that varying the thickness of the Fe–N–C cathode layer can impact P_{max}, with values ranging from 0.287 to 0.450 W cm^{-2} when the cathode catalyst loading increased from 1 to 2 mg cm^{-2} [120]. Additionally, Khan et al. synthesised Cr and Mn-based catalysts, achieving a P_{max} of 309 mW cm^{-2} and a current density of 610 mA cm^{-2} in AEMFC testing [121]. Lilloja et al. reported the preparation of CoFe-N-CDC/CNT catalyst, which displayed exceptional AEMFC performance at 1120 mW cm^{-2} [122]. Woo et al. synthesised iron and nitrogen co-doped carbon catalysts using a silica coating-mediated synthetic strategy, with the P_{max} of 635 mW cm^{-2} for the Fe-S-Phen-CNT catalyst [71].

Table 1. Comparison of TM-based cathode catalysts for AEMFC.

	RDE Test Data		H_2/O_2 AEMFC Fuel Cell Test Data		Ref
Catalyst	E_{onset} (V vs RHE)	$E_{1/2}$ (V vs RHE)	OCV (V)	P_{max} (mW cm^{-2})	
FeCoN-MWCNT	0.93	0.86	0.98	692	[II]
FeMnN-MWCNT	0.93	0.85	0.95	582	[II]
FeNiN-MWCNT	0.94	0.87	0.96	406	[III]
FeNiN-MC	0.94	0.88	1.00	386	[III]
FeCoNC-at	0.96	0.83	1.04	415	[123]
Fe-Co-N-C	0.90	0.76	0.90	420	[124]
CoFe-N-CDC/CNT	0.96	0.83	0.90	1120	[122]
0.14Co0.01FeCB	0.96	0.86	0.99	304	[125]
FeMn-N-MPC	0.98	0.89	0.99	474	[126]
FeCu1.0NC	1.00	0.92	1.01	294	[127]
NiCo/NCNT	0.98	0.88	0.96	65.0	[128]
Zn-Co/N/C-IL20	0.93	0.84	0.94	300	[129]
Fe-N-C	0.99	0.89	1.02	220	[130]
SiCDC/CNT(1:3)/CoPc	0.91	0.81	0.94	473	[131]
Co-N-CDC/CNT mel	0.95	0.82	0.96	577	[132]
Fe-NMG	0.96	0.83	1.05	218	[72]
TiCDC/CNT(1:3)/FePc	0.93	0.77	1.00	182	[133]
CNT/PC (Fe–N/C)	0.96	0.88	0.95	350	[70]
Fe-N-C	1.00	0.88	0.97	1800	[134]
FeN_x-CNTs	1.08	0.94	0.85	1150	[135]
FeCu-NC	-	0.882	-	910	[136]
Fe-N-C Act	-	0.90	-	786	[137]
Co_1/CNH 700	-	0.833	-	472	[138]
FeCo-NCH	-	0.889	-	569	[139]
Fe-Mn-N-C	1.0	0.79	-	1321	[140]
Fe-S-phen/CNT	-	0.90	-	635	[71]
FeFPc@BP2000	1.01	0.93	0.98	165	[141]
Co_3N/C	0.94	0.86	0.91	700	[142]
CoCu/PNC-900	0.91	0.81	0.74	62	[143]
CF-VC	0.78	0.71	0.85	1350	[144]
$Fe_{0.1}$-CNT@NHC	0.89	0.80	1.46	106	[145]
Fe-EDTA-Graphene	1.03	0.86	0.97	330	[146]

Additionally, as depicted in Table 1, a diverse array of cathode catalysts has been employed in AEMFCs, encompassing different dopants and carbon supports. Regarding transition metals, there does not appear to be a single superior transition metal; nevertheless, numerous bimetallic catalysts have exhibited noteworthy AEMFC performance. It is worth noting that alongside the selection of the AEM, the preparation of the membrane-electrode assembly and the various test parameters, including gas flow rates, backpressure, gas humidity

and fuel cell temperature, exert significant influences on the AEMFC performance [147].

4.9. RZABs using transition metal-based air-electrode catalysts

Precious metal-based catalysts, such as Pt, RuO_2 and IrO_2, exhibit high electrocatalytic activity for oxygen-involved reactions, their lack of bifunctional electrocatalytic properties limits their application in RZABs [148]. Transition metal-based catalysts can be divided into four categories: metal-organic framework/covalent organic framework (MOF/COF)-based catalysts [149], transition metal oxide catalysts [150], transition metal alloy catalysts [151]and transition metal sulphide/nitride/phosphide catalysts [152].

The bifunctional electrocatalysts can be primarily divided into two groups: (i) catalysts featuring a single type of active metal site for both the ORR and OER and (ii) catalysts with distinct active sites for ORR and OER. For instance, Liu et al. developed a highly active and stable electrocatalyst incorporating cobalt phosphide (Co_2P) embedded in Co, N, P-doped carbon (CoNPC) using zeolitic imidazolate frameworks (ZIF). In RZABs, Co_2P/CoNPC achieved a P_{max} of 116 mW cm^{-2} and an open-circuit voltage (OCV) of 1.425 V [153]. Similarly, Zhou et al. synthesised Co@hNCTs derived from ZIF-67 through a tube-directed templating strategy, resulting in a P_{max} of 149 mW cm^{-2} and long-term stability over 500 hours in RZABs operating at 5 mA cm^{-2} [154]. Moreover, a 1D carbon nanotube derived from MOF during pyrolysis was connected with 2D graphene oxide to create a 3D free-standing film (Ni@N-HCGHF) [155]. This Ni@N-HCGHF-based liquid-state RZAB exhibited a P_{max} of 117.1 mW cm^{-2}, high specific capacity of 706 mAh g_{Zn}^{-1} at 10 mA cm^{-2} and impressive stability for 100 cycles at 10 mA cm^{-2} [155].

Several other electrocatalysts have shown remarkable performance in RZABs, including NP-Co_3O_4/CC-based RZAB with an ultrahigh power density of 200 mW cm^{-2} and 400 h of runtime at 5 mA cm^{-2} [156]. CoNi/N-FLG catalysts demonstrated remarkable stability with a negligible increase in voltage gap after 2000 cycles at 10 mA cm^{-2} [151]. Additionally, the use of cobalt oxide (CoO_x) and cobalt nitride (CoN_y) nanoparticles to create CoO_x/CoN_y@CN_z catalysts resulted in excellent RZAB performance, with a P_{max} of 204.8 mW cm^{-2} [157]. FeNi/TNCF-2-based RZABs displayed stable charge–discharge processes and achieved P_{max} and OCV values of 150 mW cm^{-2} and 1.47 V, respectively [158]. Furthermore, FeCo alloy NPs embedded in N,P-co-doped carbon-coated NCNTs (NPC/FeCo@NCNT) exhibited a P_{max} of 151.3 mW cm^{-2} and an OCV of 1.429 V [159]. In a study by Lyu et al., cobalt sulphide (Co_9S_8) nanoparticles encapsulated in an N,S-co-doped carbon matrix (Co_9S_8@N,S–C) yielded promising results with a P_{max} of 259 mW cm^{-2} and stable charge–discharge cycling for over 110 h [160]. Many other works utilising transition metal-based materials as RZAB air electrode catalyst have been done (Table 2).

Table 2. The ORR, OER and RZABs performance of TM-based catalysts.

Catalyst	$E_{1/2}$ (V)	$E_{j=10}$ (V)	OCV (V)	P_{max} (mW cm^{-2})	Stability /Duration @*j* (mA cm^{-2})	Ref.
NiCoN-CNT	0.89	1.61	1.338	-	13 h @ 1	[I]
FeNiN-MWCNT	0.87	1.59	1.45	84.5	48 h @ 1	[III]
FeNiN-MC	0.88	1.58	1.47	71.9	48 h @ 1	[III]
CoN-PC-2	0.81	1.70	1.47	158	45 h @ 5	[V]
FeCoN-PDF-T_2-2	0.85	1.6	1.53	258	25 h @ 10	[VI]
CoSA/N,S-HCS	0.85	1.536	1.5	173.1	1000 cycle@10	[161]
FeCoMoS@NG	0.83	1.468	1.44	118	70 h @ 2	[162]
CuSA@HNCNx	0.91	1.55	1.51	212	300 h @ 10	[163]
NFO@PNC-700	0.85	1.447	1.45	130	180 h @ 5	[164]
LDH-POF	0.8	1.48	-	185	400 cycle @ 5	[165]
VO-CMON@NCN	0.857	1.47	1.404	143.7	500 h @ 5	[166]
S-CFZ	0.82	1.52	-	178	500 h @ 25	[167]
CMO–U@CC	0.81	1.482	1.42	135	45 h @ 10	[168]
Vo-CoFe/$CoFe_2O_4$@NC	0.858	1.59	1.53	139.5	45 h @ 10	[169]
Co/$ZnCo_2O_4$@NC-CNT	0.9	1.6	1.47	305	103 h @ 5	[170]
NiFe/bNCNT	0.8	1.56	1.52	224	330 h @ 10	[171]
Co/CoS/Fe-HSNC	0.9	1.48	-	213	50 h @ 2	[172]
CoDNG900	0.864	1.613	1.45	205	667 h @ 10	[173]
FeNi-SAs@NC	0.907	1.528	1.54	260	100 h @ 20	[174]
Co_3O4/Co@NCs	0.92	1.55	1.5	123.4	600 h @ 10	[175]
CoFe-Co@PNC	0.887	1.55	1.46	152.8	200 h @ 10	[176]
Co/N@CNTs@CNMF	0.86	1.54	1.52	133	190 h @ 10	[177]
Fe,Mn/N–C	0.928	1.62	1.4	160.8	81 h @ 5	[178]
FeNi/N-CPCF-950	0.89	1.585	1.478	160.6	640 h @ 10	[179]
BFC-FC-0.2	0.9	1.6	1.49	160	100 h @ 2	[180]
CoNi/Co-N@HNC	0.86	1.58	1.43	179.1	350 h @ 20	[181]
CoFe/Co@NCNT/NG	0.876	1.611	1.4	161	300 cycle @ 2	[182]
Fe-N-C/N-OMC	0.93	1.761	-	113	4000 min@10	[183]
H-Co@FeCo/N/C	0.91	1.608	1.45	125.2	200 h @ 10	[184]

Despite the significant progress, several challenges must be addressed to develop highly efficient RZAB systems in the near future. Firstly, the primary challenge with transition metal-based carbon catalysts is their limited stability during long-term use, particularly in the OER. To overcome this, techniques like increasing the degree of graphitisation in the carbon matrix, heteroatom doping and active site encapsulation can enhance the stability of these catalysts [185–187]. Secondly, many electrocatalysts have been produced using MOFs, which are costly, complex to synthesise and have low yields, limiting their scalability. Therefore, research should focus on discovering low-cost precursor-based catalyst synthesis methods to create highly active bifunctional catalysts suitable for mass production. Thirdly, it is crucial to conduct systematic post-mortem ana-

lysis of the catalysts after RZAB test to understand their transformation during the charging and discharging processes. Furthermore, additional developments are required for other components, such as the zinc electrode and electrolyte. Corrosion and passivation issues observed in the zinc electrode, partly due to the highly concentrated alkaline electrolyte, can be addressed by finding zinc alloys to prevent corrosion and passivation or by employing neutral electrolytes or solid polymer electrolytes. Finally, a universal RZAB setup and criteria need to be established. Currently, homemade RZABs with diverse configurations are commonly used in experiments, leading to varying performance results that are difficult to compare.

5. AIM OF THE STUDY

The objective of this PhD thesis was to develop innovative electrocatalysts, investigate the performance of transition metal-based catalysts using advanced nanocarbon supports or polymer-derived carbon for the bifunctional oxygen electrocatalysts and assess their suitability as electrode materials in AEMFCs and RZABs. The primary goal was to establish correlations between synthesis methods, material structures and electrocatalytic activities. The thesis was structured into three main components, each with specific objectives:

1. To develop the bimetallic, nitrogen-doped MWCNT, characterise their physico-chemical properties and electrocatalytic activity towards the ORR and OER and as AEMFC and RZAB electrode [I,II].
2. To study the effect of different carbon supports on the ORR and OER [III] and develop the transition metal-doped CDC/G composite for the ORR in acidic media [IV], characterise their physico-chemical properties and electrocatalytic activity towards the ORR and OER.
3. To develop carbon supports for the ORR and OER from polymer framework and study their electrocatalytic activity and physico-chemical properties and test in RZAB [V,VI].

6. EXPERIMENTAL

6.1. Synthesis of bimetallic phthalocyanine-doped carbon catalysts

The synthesise of bimetallic-doped carbon nanotubes, NiCoN-CNT [I] and FeMnN-MWCNT [II], the following procedure was followed: For the NiCoN-CNT, 20 mg of multiwalled carbon nanotubes (CNT [I] or MWCNT [II], Nanocyl S.A., Belgium), 10 mg of nickel phthalocyanine (FePc, Alfa Aesar) and 10 mg of cobalt phthalocyanine (CoPc, Alfa Aesar) was mixed in 5 mL of ethanol. The mixture was sonicated for 1 h to obtain a homogeneous suspension. Ethanol was evaporated in an oven at 60 °C. Then, the mixture was pyrolysed at 800 °C for 1 h in N_2 atmosphere. Other catalysts, namely, NiMnN-CNT, MnCoN-CNT in work [I] and FeMnN-MWCNT, FeCoN-MWCNT and FeNiN-MWCNT in work [III] were also prepared by the same method, using respective metal phthalocyanine were employed (Table 3).

Table 3. Preparation of bimetallic and nitrogen-containing CNT-based electrocatalysts [I,II]

Catalyst	FePc (mg)	MnPc (mg)	CoPc (mg)	NiPc (mg)	CNT/MWCNT (mg)
NiCoN-CNT	-	-	10	10	20
MnCoN-CNT	-	10	10	-	20
MnNiN-CNT	-	10	-	10	20
FeMnN-MWCNT	10	10	-	-	20
FeCoN-MWCNT	10	-	10	-	20
FeNiN-MWCNT	10	-	-	10	20

For comparing the effect of different carbon supports on bimetal-doped electrocatalysts [III], the prescribed protocol was followed: 5 mg of both metal phthalocyanines (FePc and NiPc) and 30 mg of corresponding carbon supports, including, MWCNT, graphene (G, Strem Chemicals), carbide-derived carbon (CDC, Skeleton Technologies), Vulcan carbon (VC, Cabot Corp.), graphene nanoflakes (Gr, Graphene Supermarket) and mesoporous carbon (MC, Pajarito Powder) were added to 5 mL of ethanol in a beaker. Prior to utilisation, the acquired CDC was pulverised by wet ball milling at 400 rpm for a period of 2 h, (4×30 min intervals, 5 min halt each). Then, the mixture was sonicated for 1 h to achieve a uniform suspension. The suspension was transferred to a Petri-dish and kept in an oven at 60 °C for drying. The mixture was pyrolysed for 1 h at 800 °C in N_2 atmosphere to prepare the desired catalysts, namely, FeNiN-MWCNT, FeNiN-G, FeNiN-CDC, FeNiN-VC, FeNiN-Gr and FeNiN-MC [III].

6.2. Synthesis of Fe-doped carbide-derived carbon and graphene composite

For the synthesis of FeN-CDC/G/DCDA [IV], the CDC was subjected to wet ball milling at 400 rpm for a duration of 2 h, with intermittent 30 min intervals of milling using ZrO_2 balls (diameter = 0.5 mm). Subsequently, a composite consisting of 40 mg of CDC (Skeleton Technologies) and graphene (G, Graphene Supermarket) in a weight ratio of 3:1 was prepared and subjected to 30 min of sonication in 40 mL of ethanol. Following this, 5 mg of FePc (Alfa Aesar) was introduced into the mixture and subjected to an additional hour of sonication. To this composite, 400 mg of dicyandiamide (DCDA, Sigma Aldrich) was added, followed by an additional 30 min of sonication. The resulting reaction mixture was then subjected to drying under constant stirring. Ultimately, the reaction mixture underwent pyrolysis at 800 °C for a duration of 1 h in an inert atmosphere, yielding the final product denoted as FeN-CDC/G/DCDA. FeN-CDC/G and N-CDC/G/ DCDA were also synthesised for comparative purposes, with FeN-CDC/G excluding DCDA and N-CDC/G/DCDA excluding FePc, respectively.

6.3. Synthesis of Co-doped phloroglucinol polymer-derived carbon catalysts

For a standard synthesis procedure for phloroglucinol polymer [V], 2.2 g of phloroglucinol (Alfa Aesar) was dissolved in 20 mL of Milli-Q water in a beaker at 45 °C. Then, 10 g of formaldehyde solution (37%, Thermo Fisher Chemical) was mixed with phloroglucinol solution under continuous stirring for 30 min. The reaction between phloroglucinol and formaldehyde took place, forming a yellowish-orange precipitate. Next, 4.4 g of 2-methylimidazole was dissolved in another beaker containing 40 mL water at 45 °C. Then, both solutions were mixed and stirred for 12 h at 60 °C. Subsequently, the product underwent filtration, followed by multiple water rinses and drying at 60 °C, resulting in the production of the phloroglucinol-formaldehyde-methylimidazole (PFM) framework. For the synthesis of CoN-PC-1, 100 mg of PFM powder and 5 mg of CoPc (Alfa Aesar) were suspended in 25 mL of ethanol by sonication for 1 h. Then, the mixture was dried out at 60 °C followed by pyrolysis at 800 °C under an inert atmosphere to get the CoN-PC-1. The CoN-PC-2 was also prepared via a similar route by changing the amount of CoPc to 10 mg and PC-800 was prepared by pyrolysing the PFM polymer at 800 °C without adding CoPc.

6.4. Synthesis of Zn-assisted Fe and Co-doped PDF polymer derived carbon catalysts

In a typical synthesis of FeCoN-PDF-T_2-2 [VI], the following procedure was employed: 1 g of phloroglucinol and 2 g of DCDA were mixed in 20 mL of formaldehyde solution (37%, Thermo Fisher Chemical) by mortar and pestle for about 30 min. Then, a certain amount of solutions of iron and cobalt nitrate salts (ratio 1:1 wt.%, Sigma Aldrich) were added to the mixture and grinded about 30 min. Further, the obtained solid was exposed to 150 °C for 8 h in a muffle furnace for curing to get the Fe- and Co-containing phloroglucinol-dicyandiamide-formaldehyde (PDF) polymer (FeCo-PDF-2). To achieve the high surface area porous materials, as-prepared PDF materials were mixed with zinc nitrate salt (Sigma Aldrich) at 1:2 wt.% ratio while 1 mL ethanol was also added for homogeneous mixing. The resultant dried mixture was then pyrolysed at 950 °C for 1 h in N_2 atmosphere to obtain the final product, FeCoN-PDF-T_2-2 [VI].

6.5. Electrode preparation and electrochemical measurements

The electrochemical ORR and OER measurements were performed at room temperature with a potentiostat/galvanostat PGSTAT30 (Metrohm Autolab, The Netherlands) in a conventional three-electrode system using a platinum wire, saturated calomel electrode (SCE) and catalyst-coated glassy carbon (GC) rotating disk electrode (geometric area = 0.196 cm^2) as a counter electrode, reference electrode and the working electrode, respectively. The electrochemical cell was filled with 0.1 M KOH (Merck) or 0.5 M H_2SO_4 solution (Merck), which was saturated with oxygen (99.99%, Linde Gas) or argon (99.99%, Linde Gas) was used to carry out the experiments at room temperature. A polished GC disk was drop-cast with 10 µL of a uniform suspension of 4 mg of prepared catalyst in 1000 µL of 2-propanol: water: Nafion solution (1:1:0.03) and dried at 60 °C to achieve the 0.2 mg cm^{-2} [I,II,III,V,VI] or 0.8 mg cm^{-2} [IV] catalyst loading.

All potentials were converted against the reversible hydrogen electrode (RHE) using the equation $E_{RHE} = E_{SCE} + 0.242 + 0.059 \times pH$ and the electrochemical data given in this work were *i*R-corrected using the positive feedback method. To measure the background current, cyclic voltammograms (CV) were recorded in an Ar-saturated electrolyte at a potential scan rate (v) of 10 mV s^{-1}. Furthermore, the rotating disk electrode (RDE) technique was used to investigate the ORR and OER activity of the catalysts. To change the electrode rotation rate (between 360 and 3100 rpm), a speed control unit (CTV101) was attached to a rotator (EDI101, Radiometer). The ORR onset potential (E_{onset}) is defined as the potential at which the current density reaches −0.1 mA cm^{-2}. Measurements of the OER polarisation curves were carried out in an Ar-saturated 0.1 M KOH [I,II,III,V] or 1 M KOH [VI] at a rotation rate of 1600 rpm and a scan rate of

10 mV s^{-1}. $E_{j=10}$ is denoted as the potential at which the OER current density reaches 10 mA cm^{-2}. Accelerated degradation test (ADT) was used for ORR stability of the catalysts, the working electrode was cycled 10,000 times between 1.0 and 0.6 V vs. RHE at 100 mV s^{-1} in O_2-saturated 0.1 M KOH solution. Before and during the stability test, the RDE polarisation curves were measured at either 1900 or 1600 rpm at 10 mV s^{-1}.

The RDE experimental data were analysed by the Koutecky-Levich (K-L) equation. The number of electrons (n) were calculated by the following equations:

$$j^{-1} = j_k^{-1} + j_d^{-1} \quad (4)$$

$$j_d = 0.62nFD_0^{2/3}v^{-1/6}C_0\omega^{1/2} \quad (5)$$

where j, j_k and j_d represent the measured, kinetic-limited and diffusion-limited current densities, respectively. n is the number of electrons transferred per O_2 molecule, F is the Faraday constant (96,485 C mol^{-1}), D_0 is the O_2 diffusion coefficient in 0.1 M KOH (1.9×10^{-5} cm^2 s^{-1}), v is the kinematic viscosity of the electrolyte solution (0.01 cm^2 s^{-1}), C_0 is the concentration of O_2 in bulk solution (1.2×10^{-6} mol cm^{-3}) and ω is the rotation rate of the electrode (rad s^{-1}).

To detect the presence of a peroxide intermediate (H_2O_2) in acidic electrolyte during the rotating ring-disk electrode (RRDE) measurements in the study [IV], the Pt ring electrode was held at a constant potential of 1.2 V. Before recording the ORR polarisation curve, the Pt ring was electrochemically cleaned by applying three potential cycles ranging from 0.05 to 1.65 V at a scan rate of 100 mV s^{-1}. The collection efficiency (N) of the Pt ring electrode was determined to be 0.22, based on the hexacyanoferrate(III) reduction reaction. The RRDE data were then utilised to calculate the yield of peroxide and the number of electrons transferred (n). The percentage yield of H_2O_2 formation at the disk electrode was determined using equation (6). The number of electrons transferred per O_2 molecule (n) was calculated from the RRDE results using equation (7), where I_d represents the disk current, I_r is the ring current and N is the collection efficiency of the ring electrode.

$$\%H_2O_2 = \frac{(200I_r)}{(I_dN+I_r)} \quad (6)$$

$$n = \frac{4I_d}{(I_d+I_r/N)} \quad (7)$$

6.6. Preparation of RZAB

The activity and stability of catalysts prepared in this study was investigated in solid-state RZAB [I] and liquid-state RZAB [III,V,VI].

Solid-state RZAB: The anode was composed of a clean Zn foil and the electrolyte used was a KOH-polyvinyl alcohol (KOH-PVA) polymer gel. The KOH-PVA polymer electrolyte gel was prepared as follows: 5 g of PVA and 183 mg of zinc acetate (0.2 M, Sigma Aldrich) were dissolved in 48 mL of Milli-Q water at 95 °C for 1 h. Subsequently, 6 g of KOH solution (1 g/mL) was added dropwise. The mixture was stirred at 95 °C for 30 min and then cooled down to room temperature. The resulting mixture was poured into a petri dish to create a 5 mm thick membrane, which was then frozen for 16 h. Afterward, the gel was left at room temperature for 6 h to thaw before use. To prepare the air-cathode, a catalyst suspension was created using 10 mg of the catalyst in 1 mL of 2-propanol and 10 μL of a 5 wt.% Nafion solution was added as a binder. This catalyst suspension was then drop-casted onto a carbon cloth.

Liquid-state RZAB: A home-made rechargeable zinc-air battery device was employed to assess the electrocatalyst's performance and stability in battery applications. The battery's electrolyte consisted of a solution containing 6 M KOH and 0.2 M $Zn(CH_3COO)_2$. To prepare the catalyst ink, 7 mg of catalyst was dispersed in a solution consisting of 20 μL of Nafion solution and 800 μL of a water-ethanol mixture with a volume ratio of 1:3. This mixture was sonicated for a minimum of 60 min to ensure the formation of a uniform ink. The catalyst ink was then drop-cast onto a gas diffusion layer (GDL) with an area of 3.5 cm^2 (Sigracet 39 BB) to achieve a catalyst loading of 2 mg cm^{-2}. For the anode, a polished zinc foil with a thickness of 0.2 mm was utilised. Both the Zn foil and the GDL coated with catalyst had an exposed area to the electrolyte solution of 0.79 cm^2 [III,V] or 1 cm^2 [VI]. As a point of reference, a Pt−Ru/C catalyst was also prepared with a catalyst loading of 1 mg cm^{-2} and tested using the same procedure.

6.7. MEA preparation for AEMFCs and AEMEL

The activity of the catalysts prepared in this study was investigated in AEMFCs [II,III]. For testing the activity of FeCoN-MWCNT and FeMnN-MWCNT [II], the gas diffusion electrode (GDE) method was employed to create both the anode (ACL) and cathode catalyst layers (CCL) for testing in AEMFCs. Before applying the catalyst layers to the gas diffusion layers, a thin 17 μm micro-porous carbon layer was deposited to help elucidate flooding in the mass transport region of the fuel cells, particularly at higher current densities [188]. The PtRu (Alfa Aesar) loading for all anodes was maintained at 0.7 ± 0.03 mg_{PtRu} cm^{-2}, resulting in an ACL with a thickness of 69 μm. In contrast, the M-N-C cathodes were loaded to 0.745 mg cm^{-2}, yielding CCLs with a thickness of 38 μm. To prepare the electrodes, as well as two pieces of 9 cm^2 FAA-3-05-rf anion-exchange membrane (based on FAA-3 polymer reinforced with porous ePTFE-film, provided by Fumatech, Germany), they were each immersed separately in Petri dishes containing 1 M KOH aqueous solution for 1 h. The solution in each Petri dish was refreshed every 20 min to ensure complete conversion of the AEM into its hydroxide form. Two AEMFCs were assembled

using pairs of 5 cm^2 single-serpentine graphite bipolar flow fields with PTFE gaskets, resulting in a compression level of 25% and they were torqued to 4.5 Nm. The cells were evaluated using an 850E Scribner Associates Fuel Cell test station under different gas compositions: H_2–O_2 and subsequently H_2-air (CO_2-free) were directed to the anode and cathode, respectively. All tests were conducted at a cell temperature of 60 °C with similar operating conditions to enable a fair and unbiased comparison of the catalysts. These AEMFC tests were performed by J.C. Douglin at Technion, Israel Institute of Technology (Israel). For the AEMFCs activity of FeNiN-C [III], the membrane-electrode assembly (MEA) was prepared using the catalyst coated GDL (Sigracet 39 BB) and AF2-HLE8-10-X (AEMION+ 10 μm, Ionomr Innovations) AEM. The 3 wt.% ionomer solution was prepared by dissolving hexamethyl-p-terphenyl poly(benzimidazolium) (HMT-PMBI) in methanol [189]. The cathode GDL was coated with the catalyst ink prepared by dispersing 12.5 mg of catalyst material in 1422 μL of methanol, 430 μL of Milli-Q water and 195 μL of 3 wt.% ionomer solution. For the anode GDL, the catalyst ink was prepared from 6.7 mg of Pt−Ru/C (50:25:25, Alfa Aesar), 689 μL of methanol, 196 μL of Milli-Q water and 49 μL of 3 wt.% ionomer solution. After the sonication for 1.5 h to get the homogeneous suspension, the catalyst ink was dropcast onto the corresponding GDL and dried in an oven at 52 °C. After evaporation of the solvents, the catalyst loadings of 2 mg cm^{-2} and 0.8 mg_{PtRu} cm^{-2} were obtained on the cathode and anode, respectively. The prepared GDL and the AEM were soaked in 3 M KOH for one and four days before use in AEMFC, respectively. The 3 M KOH for AEM was replaced every 24 h to make sure the complete conversion of AEM to the hydroxide form. The AEM and electrodes with silicone gaskets (250 μm) were sandwiched together using a torque of 9 Nm into a 5 cm^2 cell (Fuel Cell Technologies Inc., USA). A Greenlight Fuel Cell Test Station (G40 Fuel Cell System, Hydrogenics, Canada) was used for the single-cell AEMFC experiments. The cell was fed using 1 NLPM gas flow rate and humidified (65 % RH) H_2 and O_2 gases at 65 °C with the backpressure set for 200 kPa.

For anion exchange membrane electrolyser (AEMEL) in work [II], MEA were prepared by spray-depositing catalyst inks onto a Fumasep VM-FAA-3-10-rf 10 μm thick AEM. Two catalysts, FeNiN-MWCNT and RuO_2, were used. The inks were prepared with catalyst powder mixed with ionomer solution (activated FAA-3) and spray-deposited onto the membrane. After determining catalyst loading (between 1.8 and 1.9 mg cm^{-2} for both catalysts), the membranes were hot-pressed, and for the cathodic reaction, a platinum on carbon GDL (Baltic FuelCells) was used. The assemblies were encased, pressurised, and activated with 0.1 M KOH. FeNiN-MWCNT and RuO_2 performance was evaluated in AEM electrolysis at 60 °C. The series resistance was ~0.6 Ω cm^2, and LSV was conducted up to 2 V. Stability testing of FeNiN-MWCNT was performed through chronoamperometry at 1.8 V for 2 h.

6.8. Physical characterisation methods

For N_2 physisorption experiments, the catalyst materials were dried in vacuum overnight at 300 °C prior to analysis. The NovaTouch LX2 instrument (Quantachrome) was used for the analysis and TouchWin 1.11 software was used for all calculations. The specific surface area (S_{BET}) was calculated utilising the Brunauer–Emmett–Teller method in the P/P_0 range of 0.02–0.2. The quenched solid density functional theory (QSDFT) equilibria model for slit-type pores was utilised for the calculation of the volume of micropores (V_μ) and pore size distribution (PSD). The total pore volume (V_{tot}) was evaluated at the N_2 saturation pressure ($P/P_0 = 0.97$). The catalysts' crystallinity was determined by X-ray diffraction (XRD) analysis. The XRD measurements were conducted on a Bruker D8 Advance diffractometer with Ni-filtered Cu Kα radiation (λ = 1.54184 Å). Scanning steps of 0.0126° were used to obtain the diffraction patterns in 2θ range of 5–90°. X-ray photoelectron spectroscopy (XPS) was used to determine the surface elemental composition using the electron energy analyser SCIENTA SES-100 and Mg Kα X-rays (1.2536 keV) from Thermo XR3E2, a twin-anode X-ray tube. The survey scan was measured in the range from 1000 to 0 eV with a 0.5 eV step size, 0.2 s step duration and an average of five scans. The core-level spectra were averaged with a 0.2 eV step size and 0.2 s step duration over the course of thirty scans. The Gauss–Lorentz hybrid function (GL 70, Gauss 30%, Lorentz 70%) was utilised for the data analysis on CasaXPS software (version 2.3.17). Micro-Raman spectra were recorded in the back-scattering geometry on an inVia Renishaw spectrometer together with an Olympus confocal microscope (50× objective) and an argon-ion laser operated at 514.5 nm. To avoid thermal decomposition of the sample, the laser power density was minimised by decreasing the laser power and defocusing laser spot to about 15 μm. The surface morphology of the prepared catalysts was assessed using a Helios Nanolab 600, FEI scanning electron microscope (SEM). The bulk elemental composition of the catalyst materials was determined using the energy dispersive X-ray (EDX) spectrometer from Oxford Instruments, coupled to the same scanning electron microscope. Catalyst suspension was drop-casted onto polished glassy carbon (GC) discs to prepare SEM samples. Transmission electron microscopy analysis was performed in the scanning mode (STEM) at 200 kV using a Cs-probe-corrected transmission electron microscope (FEI Titan Themis 200). The distribution of the elements in the material was visualised using STEM-EDX mapping conducted in Titan Themis 200 microscope using the SuperX EDX system (Bruker/FEI). For STEM measurements, the catalyst materials were suspended in 2-propanol and drop-casted onto lacey carbon-coated copper TEM grids.

7. RESULTS AND DISCUSSION

7.1. Electrocatalysis on bimetallic, nitrogen-doped CNT-based catalysts

The first part of the PhD thesis deals with the electrocatalytic activity of bimetallic, nitrogen-doped carbon nanotubes towards ORR/OER. This first chapter deals with the bifunctional activity of the bimetal-doped (except Fe) CNT materials in alkaline media and applied as solid-state RZABs electrode material [I], while the second chapter is dedicated to Fe-containing bimetal-doped MWCNTs and utilised as AEMFCs cathode materials [II].

7.1.1. Bimetal phthalocyanine-modified CNT-based bifunctional catalysts

Transition metal phthalocyanines are highly regarded as exceptional dopants for creating active sites in electrocatalytic reactions, as elaborated in chapter 4.5 and 4.6. Multiwalled carbon nanotubes were chosen as the carbon support due to their superior electrical conductivity and high graphitisation levels [190]. Bimetallic dopants play a crucial role in furnishing active sites that facilitate both the ORR and OER processes.

The crystallographic structure of the prepared catalysts was investigated by XRD. The XRD patterns of the different catalysts unveiled a prominent peak at ca. 25.6°, which could be attributed to the (002) plane of graphitic carbon (Figure 4a). Additionally, there were smaller diffraction peaks at around 43° and 53°, which were associated with graphitic 2H(100) planes, transition metal nanoparticles (Mn, Co, Ni) and metal alloy nanoparticles (NiCo and MnNi) [191].

N_2 physisorption analysis was carried out to determine the specific surface area (S_{BET}) and porosity of the synthesised catalysts. The N_2 adsorption-desorption isotherms for all three catalysts, exhibited a similar shape, as illustrated in Figure 4b, which corresponds to a combination of types I and III with H3 hysteresis according to IUPAC classification [192]. This indicates that the materials possess a micro-mesoporous nature with a smaller proportion of micropores. The specific surface area for all the catalyst materials was approximately 200 $m^2\,g^{-1}$ (shown in Table 4). Furthermore, all three catalyst materials exhibited similar porous structures, with a total pore volume (V_{tot}) ranging from 0.30 to 0.45 $cm^3\,g^{-1}$ and a micropore volume (V_{μ}) of around 0.03 to 0.05 $cm^3\,g^{-1}$.

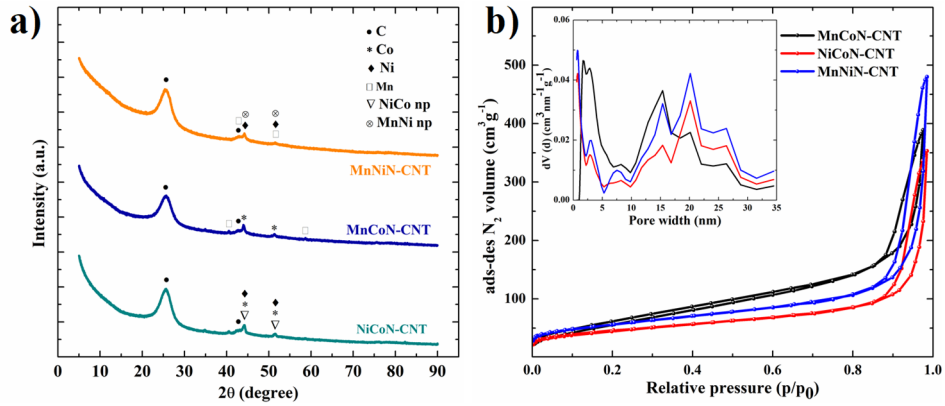

Figure 4. (a) XRD patterns (np stands for nanoparticles); (b) N_2 adsorption-desorption isotherms and pore size distribution (the inset) of MnCoN-CNT, NiCoN-CNT and MnNiN-CNT materials.

Table 4. Specific surface area and total pore volume of the as-synthesised catalysts.

Catalyst	S_{BET} (m^2 g^{-1})	S_{dft} (m^2 g^{-1})	V_{tot} (cm^3 g^{-1})
MnCoN-CNT	224	158	0.45
MnNiN-CNT	200	187	0.40
NiCoN-CNT	159	151	0.29

Furthermore, we conducted a surface morphology analysis of the prepared catalysts using SEM. As depicted in Figure 5, all the prepared catalysts exhibit a similar structure resembling CNTs. High-magnification SEM images reveal that these CNTs are oriented in random directions, forming a three-dimensional (3D) network. Some CNTs cluster together, likely due to the presence of metal nanoparticles (visible as lighter spots in Figure 5c) on the catalyst surfaces. In Figures 5d, e, f, the EDX mapping images of the prepared catalysts demonstrate that the elements, including the corresponding metals and nitrogen, are distributed relatively uniformly across the carbon matrix. The elemental composition was determined and is provided in Table 5. According to the EDX analysis, the total metal content of the bimetallic catalysts was approximately 6 wt.%. It is worth noting that all the prepared catalysts exhibited a similar structure, suggesting that the specific transition metal phthalocyanine used did not significantly impact the observable structure of the catalyst materials.

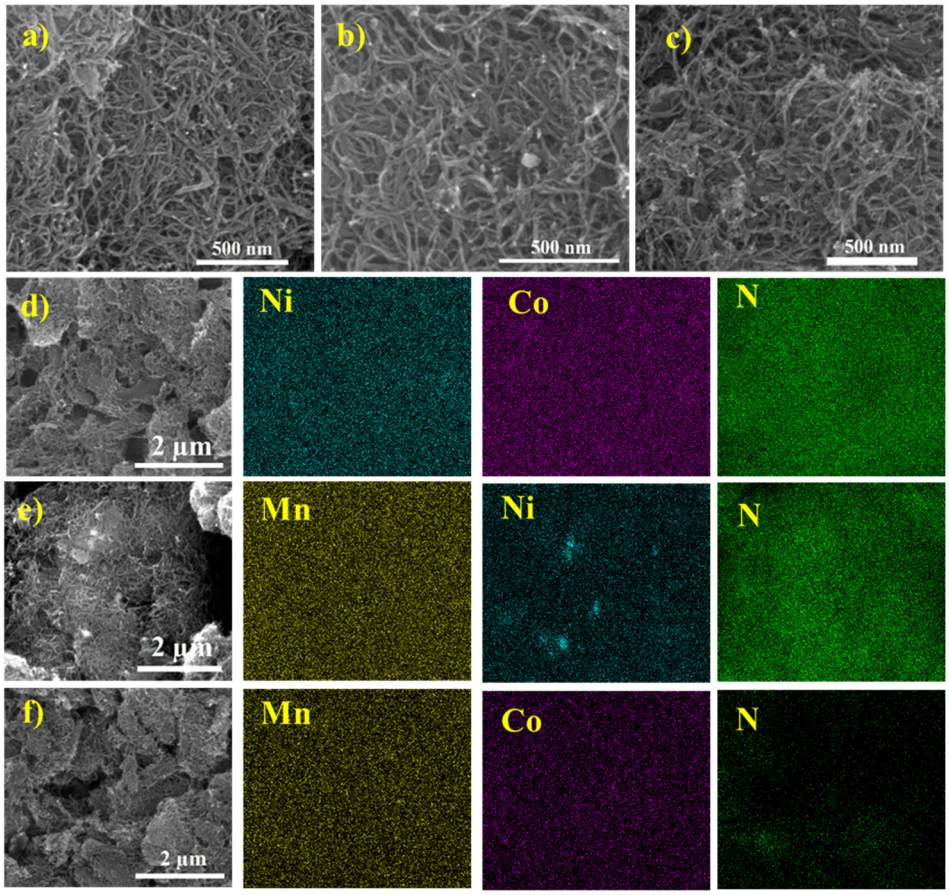

Figure 5. SEM images of (a) NiCoN-CNT, (b) MnNiN-CNT and (c) MnCoN-CNT materials. SEM-EDX images (SEM image and the corresponding elemental maps of Mn, Co and N in the shown area) of (d) NiCoN-CNT, (e) MnNiN-CNT and (f) MnCoN-CNT materials.

Table 5. Elemental composition of prepared catalysts estimated by SEM-EDX (wt.%).

Catalyst	C	N	O	Mn/Co/Ni
MnCoN-CNT	78.4	7.3	7.2	3.5 (Mn) 2.7 (Co)
MnNiN-CNT	81.8	7.7	5.1	2.8 (Mn) 2.0 (Ni)
NiCoN-CNT	82.9	8.0	2.9	2.7 (Ni) 2.8 (Co)

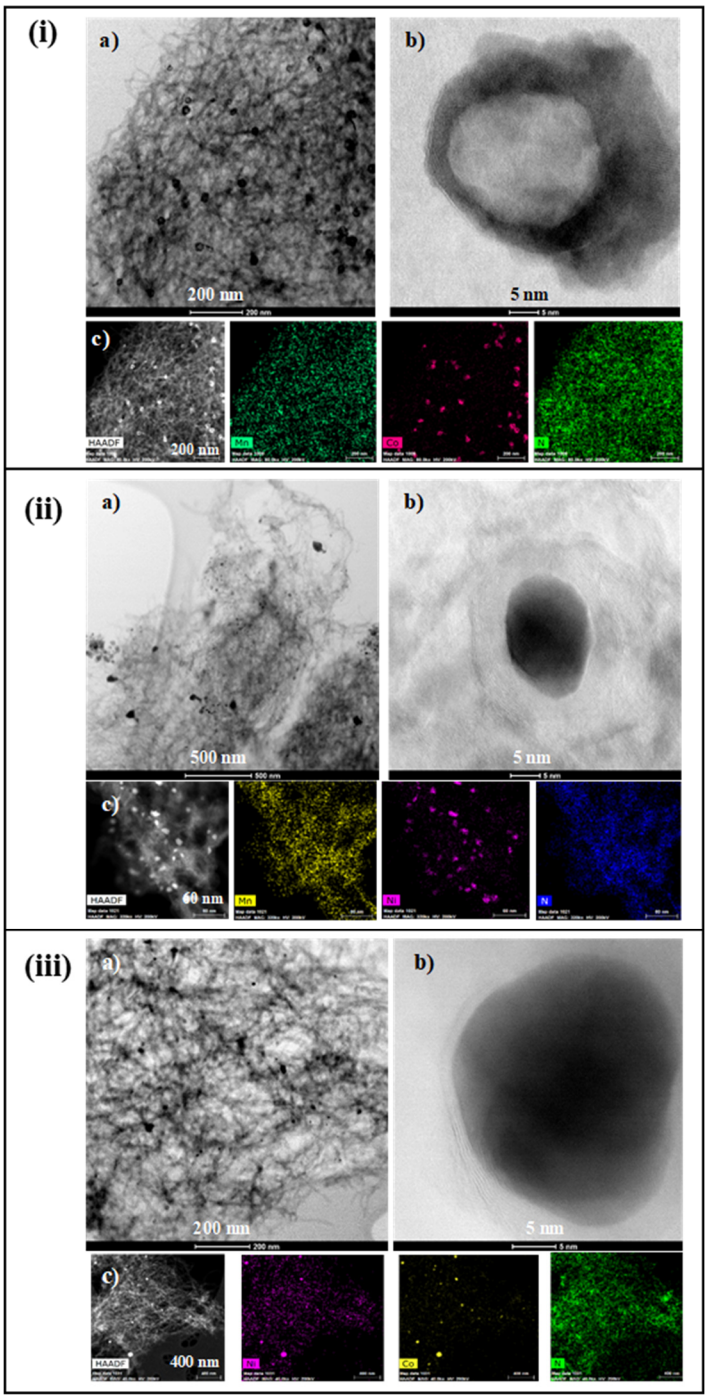

Figure 6. TEM images (a,b) and HAADF-STEM images (c) along with EDX elemental mapping images from the area shown in (c) of (i) MnCoN-CNT; (ii) MnNiN-CNT and (iii) NiCoN-CNT materials.

In addition, we employed STEM for a more comprehensive characterisation of the catalysts (Figure 6). As anticipated from the SEM micrographs, the STEM images reveal CNTs adorned with nanoparticles (Figure 6 (i)-a, (ii)-a, (iii)-a). The nanoparticles that are clearly discernible exhibit sizes ranging from several to a few tens of nanometres. Through EDX mapping of the MnCoN-CNT and MnNiN-CNT catalysts, we observed that cobalt and nickel existed in the form of nanoparticles, ranging in size from several to a few tens of nanometres, while manganese was distributed more uniformly. Notably, in the MnCoN-CNT catalyst, the cobalt nanoparticles took on the form of hollow spheres (Figure 6 (i)-b). In contrast, in the NiCoN-CNT catalyst, instead of distinct cobalt or nickel nanoparticles, Co-Ni alloy nanoparticles were formed (Figure 6iii). Furthermore, all the recorded STEM-EDX maps exhibited a prominent nitrogen signal, as shown in Figure 6.

The XPS analysis was carried out to delve deeper into the surface elemental composition of the catalyst materials. The XPS survey spectrum revealed that the prepared catalysts consist of five different elements, including the corresponding transition metals, as well as carbon (C), nitrogen (N) and oxygen (O), as illustrated in Figure 7. The N 1s core-level XPS spectra were deconvoluted into six distinct peaks, which include N-pyridinic, metal-coordinated nitrogen ($M\text{-}N_x$), N-pyrrolic, N-graphitic, bulk N-H and N-O. The results indicate that N-pyridinic type was the most abundant, followed by N-pyrrolic and $M\text{-}N_x$. It has been proposed that N-pyridinic and $M\text{-}N_x$ species could enhance the ORR activity, while N-graphitic species within the carbon matrix could facilitate electron transfer [69,193]. The presence of $M\text{-}N_x$ moieties confirms the successful doping of MPcs onto CNTs, a factor favourable for the ORR. To gain a better understanding of the coordination between transition metals and oxygen, the O 1s XPS spectrum was further analysed (Figure 3c). Notably, a peak for metal oxide is evident, signifying the coordination between metal and oxygen species. Additionally, the presence of metal oxides contributes to the enhancement of electrocatalytic performance in both the ORR and OER, as substantiated by prior studies in the literature [194–197].

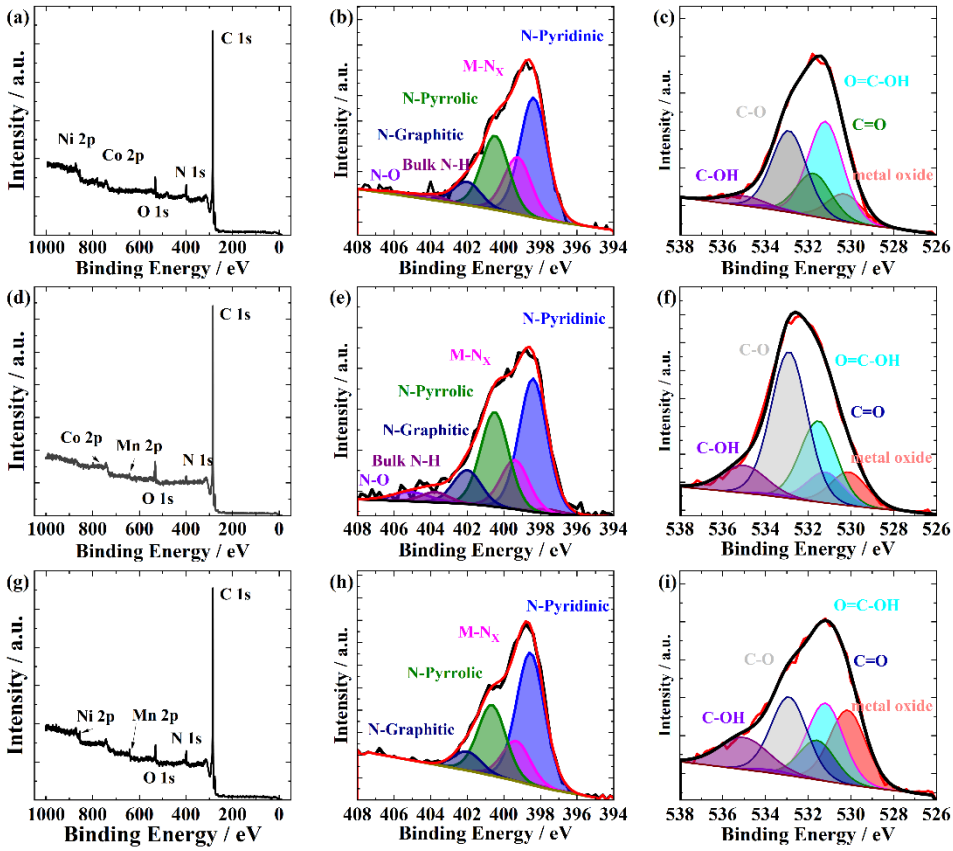

Figure 7. (a, d, g) XPS spectra, (b, e, h) N 1s and (c, f, i) O 1s high-resolution XPS spectra of NiCoN-CNT, MnCoN-CNT and MnNiN-CNT catalysts, respectively.

Initially, the electrocatalytic activity for the ORR was examined in bimetallic and nitrogen-doped CNT catalysts. CV was performed in a 0.1 M KOH solution saturated with argon (Ar) or oxygen (O_2). The CV profiles of MnCoN-CNT, MnNiN-CNT and NiCoN-CNT electrocatalysts all exhibited a distinct peak around 0.8 V during the cathodic scan, confirming their intrinsic ORR activity (Figure 8a). Subsequently, the ORR performance of these catalysts was investigated in an O_2-saturated 0.1 M KOH solution using the RDE method (Figure 8b). Notably, among the various bimetallic and nitrogen-doped CNT catalysts, MnCoN-CNT displayed exceptional ORR activity. It demonstrated E_{onset} of 0.90 V and $E_{1/2}$ of 0.84 V, the latter of which was comparable to the $E_{1/2}$ value of 20 wt.% Pt/C (0.85 V). The E_{onset} and $E_{1/2}$ values for the other catalysts were slightly lower (Table 6). In general, the favourable ORR activity of these prepared catalysts can be attributed to their micro-mesoporous nature and the presence of M-N_x centres and N-pyridinic moieties, as confirmed by XPS and N_2 physisorption analyses [20,198].

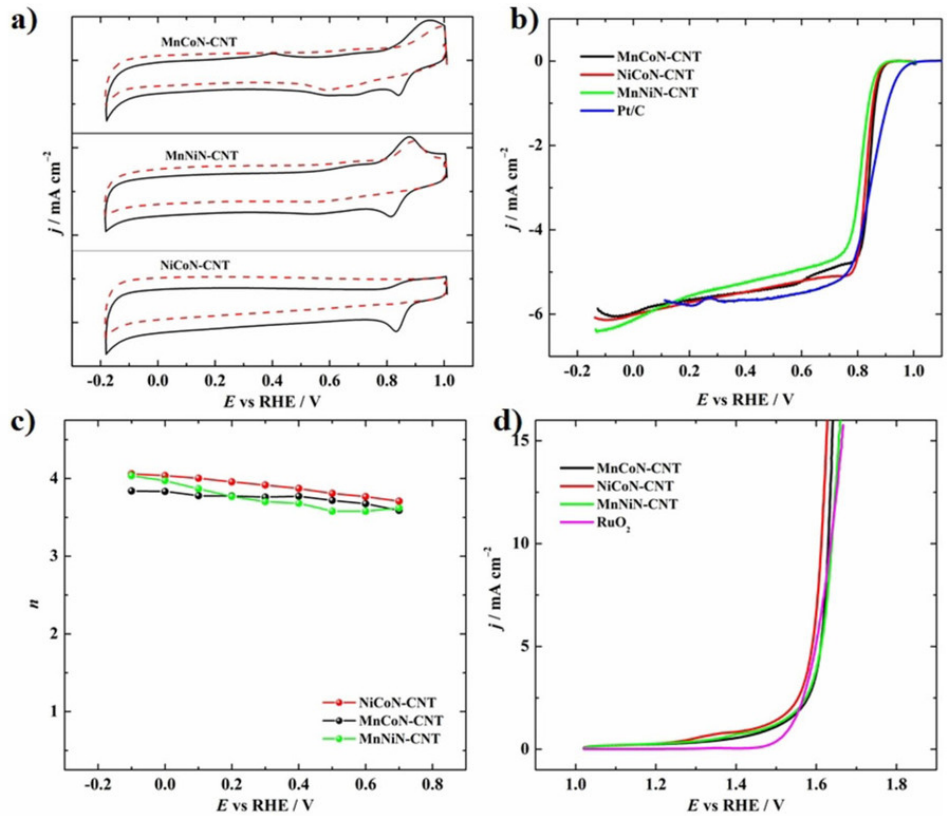

Figure 8. (a) CV of MnCoN-CNT, MnNiN-CNT and NiCoN-CNT in Ar-saturated (red dashed line) and O_2-saturated (black line) 0.1 M KOH at 10 mV s^{-1}; (b) ORR polarisation curves of several catalysts recorded in O_2-saturated 0.1 M KOH at 1900 rpm (v=10 mV s^{-1}); (c) number of electrons transferred as a function of potential; (d) OER polarisation curves recorded in Ar-saturated 0.1 M KOH electrolyte at 10 mV s^{-1} for the NPMCs and RuO_2.

Linear sweep voltammetry (LSV) curves at varying rotation rates and the corresponding K−L plots for O_2 reduction on these prepared catalysts are illustrated in Figure 9. These Figures demonstrate that as the rotation rate increases, the limiting current density also increases and the K−L plots at various potentials exhibit linear behaviour, indicating first-order reaction kinetics for the ORR.

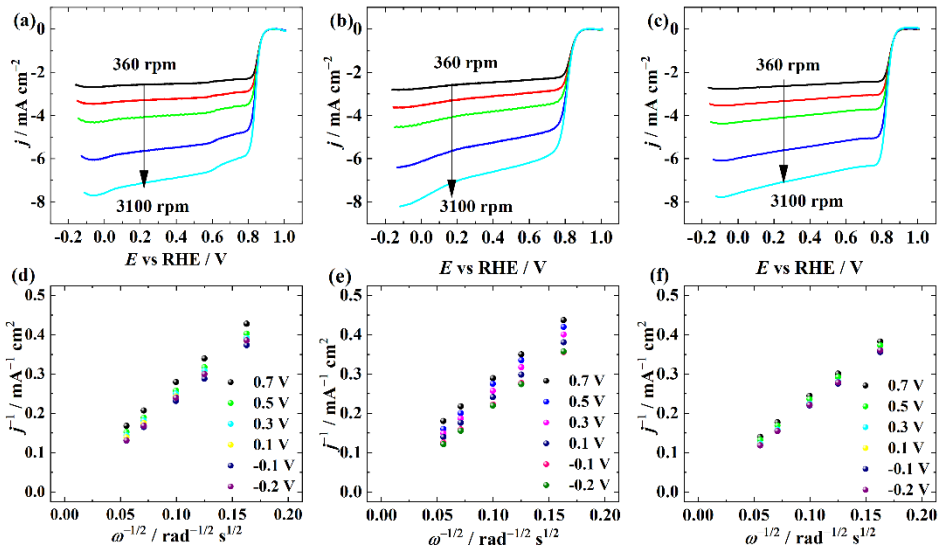

Figure 9. ORR polarisation curves for (a) MnCoN-CNT, (b) NiCoN-CNT and (c) MnNiN-CNT. Koutecky-Levich plots (derived from the corresponding RDE data) for (d) MnCoN-CNT, (e) NiCoN-CNT and (f) MnNiN-CNT catalysts in O_2-saturated 0.1 M KOH solution.

The electron transfer number was calculated using the K−L equation, as depicted in Figure 8c. It is noteworthy that all the electrocatalysts predominantly adhere to a 4-electron pathway for the reduction of oxygen. This underscores the significance of porosity and the presence of transition metal and heteroatom active sites in facilitating the adsorption and reduction of O_2. However, it is important to keep in mind that the preparation process for catalysts can be time-consuming and relatively intricate [21,125,149]. In contrast, our approach involved the straightforward one-step pyrolysis process, resulting in the synthesis of micro-mesoporous bimetallic nitrogen-doped CNTs catalysts that exhibited similar ORR performance.

Furthermore, the performance of all the prepared catalysts in the OER was assessed, as illustrated in Figure 8d. The OER performance of the as-prepared catalysts was determined at the required potential ($E_{j=10}$) for the oxidation of water to show a current density of 10 mA cm^{-2}. As shown in Figure 8d, the NiCoN-CNT catalyst displayed an $E_{j=10}$ of 1.61 V, which is comparable to that of RuO_2 (1.61 V). To assess the bifunctional oxygen electrocatalysis, the difference between the $E_{1/2}$ and $E_{j=10}$ values (ΔE) was calculated and is presented in Table 6. The NiCoN-CNT catalyst exhibited a ΔE value of 0.78 V, which was the lowest among the prepared catalysts. Both Figure 8d and Table 6 make it clear that the NiCoN-CNT catalyst demonstrated the highest OER activity and, consequently, showcased the most effective overall oxygen electrocatalysis. Previous studies have reported that transition metal oxides, such as NiO_x and

CoO_x, serve as electrocatalytically active sites for the OER [199]. At the same time, heteroatom-doped carbon materials also exhibit excellent OER activity in alkaline media [200]. Hence, it can be hypothesised that metal oxides and N moieties present in the prepared catalysts would synergistically improve the OER performance.

Table 6. Electrochemical results of as-synthesised catalysts in 0.1 M KOH solution.

Catalyst	E_{onset} (V)	$E_{1/2}$ (V)	$E_{j=10}$ (V)	ΔE (V)
NiCoN-CNT	0.89	0.83	1.61	0.78
MnCoN-CNT	0.90	0.84	1.63	0.79
MnNiN-CNT	0.88	0.80	1.64	0.84
MnN-CNT	0.93	0.86	1.69	0.83
NiN-CNT	0.86	0.79	1.61	0.82
CoN-CNT	0.91	0.83	1.63	0.80

Single metal phthalocyanine-modified CNTs were also subjected to testing for both the ORR and the OER and the results are provided in Table 6. In the cases of MnN-CNT and CoN-CNT catalysts, their ORR performance was comparable to that of the bimetal phthalocyanine-modified catalysts. However, for the OER, CoN-CNT and MnN-CNT exhibited lower activity compared to the bimetallic catalysts. Conversely, NiN-CNT displayed high activity for the OER, achieving an $E_{j=10}$ of 1.61 V, which was identical to the performance of the NiCoN-CNT catalyst. However, NiN-CNT exhibited the lowest ORR activity among all the prepared catalysts. The importance of having both active sites for ORR and OER to create an effective bifunctional electrocatalyst was demonstrated by the NiCoN-CNT catalyst [I]. In general, in this study, NiCoN-CNT achieved better ORR/OER electrocatalytic activity among the prepared catalysts that can be attributed to the presence of metal species such as M-N_x, NiO_x, CoO_x and NiCo alloy nanoparticles and nitrogen-doped carbon sites.

The stability of the electrocatalysts is very important factor for the application in metal-air batteries. Since the NiCoN-CNT exhibited the best bifunctional properties amongst other prepared catalysts, NiCoN-CNT was selected for both the ORR and OER stability test. For the ORR, very small change was observed in E_{onset} (12 mV) and $E_{1/2}$ (5 mV) after 10,000 ADT potential cycles, as shown in Figure 10a. High stability of NiCoN-CNT could be featured towards the low amount of peroxide produced during the ORR process, since peroxide is known to degrade the ORR-active sites [201]. In addition, a small change was observed in $E_{j=10}$ (14 mV) after 1000 potential cycles between 1.0 and 1.8 V (Figure 10b). The small decrease in the OER activity can be attributed to the oxidation of carbon materials at more positive potentials, which can lead to loss of active sites in materials [202]. Other factor that can possibly interfere the OER activity of the catalyst is the formation of micro-bubbles of O_2, which can block some of the active sites.

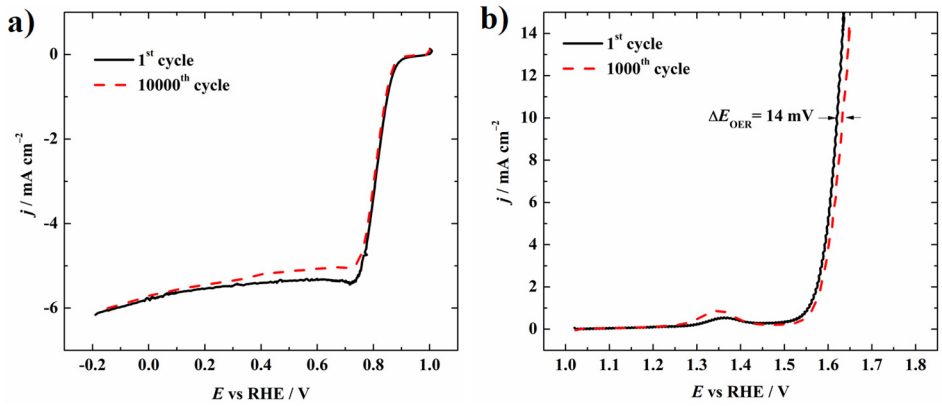

Figure 10. (a) ORR polarisation curves before and after 10000 ADT potential cycles and (b) OER polarisation curves before and after 1000 potential cycles in (a) O_2-saturated and (b) N_2-saturated 0.1 M KOH at 100 mV s^{-1} in case of NiCoN-CNT. ω=1900 rpm, v=10 mV s^{-1}.

Considering the promising electrocatalytic activities for both the ORR and the OER of NiCoN-CNT, this catalyst was evaluated as a cathode material for a solid-state RZAB. In Figure 11a, it can be observed that the NiCoN-CNT-based ZAB setup achieved an open-circuit voltage (OCV) of 1.338 V, which is approximately 0.3 V lower than the theoretical limit of ZABs. Additionally, the durability of the solid-state ZAB was evaluated by charging and discharging it at a current density of 1 mA cm^{-2} with a cycling period of 10 min. The NiCoN-CNT-based RZAB exhibited stable operation for over 13 h (Figure 11b). It is worth noting that using KOH-PVA gel as an electrolyte has the drawback of gradually drying out over time, which can reduce the battery's efficiency. After several hours of operation, the PVA gel started to dry. As depicted in Figure 11b, the initial potential gap between the charging and discharging potentials of the NiCoN-CNT-based ZAB was 0.55 V (1.75 V for charging and 1.2 V for discharging). After 13 h of cycling tests, the potential gap increased to 0.9 V, particularly for the discharge potential, indicating some degradation of active sites and/or exposure of the gel electrolyte during the cycling tests.

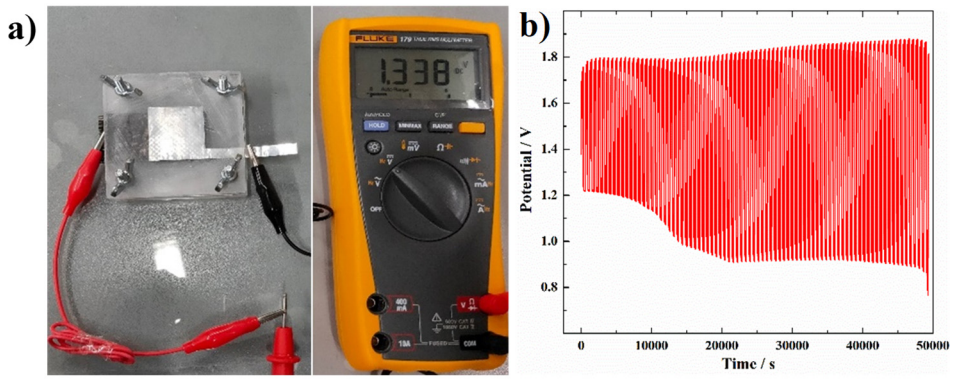

Figure 11. (a) Photograph of solid-state RZAB using NiCoN-CNT as the air cathode catalyst showing measured OCV of 1.338 V; (b) Cycling performance of the solid-state ZAB tested at 1 mA cm^{-2}.

7.1.2. Fe, M (Mn, Co) phthalocyanine-modified MWCNT materials

Owing to the good bifunctional electrocatalytic activity of NiCo-CNT in [I], other combination of transition metal was utilised and Fe-doped MWCNT along with other metal (Mn, Co and Ni) was prepared. These materials were tested in AEMFCs [II].

The microstructure and morphology of the prepared catalysts, namely FeMnN-MWCNT, FeCoN-MWCNT and FeNiN-MWCNT, were thoroughly examined by SEM. The SEM images (Figure 12) reveal that all the prepared catalysts share a similar structure consisting of carbon nanotubes. Upon closer examination at higher magnification (Figure 12), it becomes apparent that these carbon nanotubes are oriented in various directions and some of them aggregate at locations where metal nanoparticles are present. This observation is further supported by the elemental analysis. For instance, the EDX analysis results indicate that all the elements (Fe, Mn, N) are uniformly distributed on the carbon nanotubes, particularly in the case of FeMnN-MWCNT. Additionally, the elemental composition of the catalysts was quantified and the results are provided in Table 7. The total metal content determined through EDX analysis closely aligns with the anticipated value of nearly 5 wt.%, as calculated theoretically. Notably, the prepared bimetallic catalysts exhibit a consistent surface morphology, indicating that different metal phthalocyanines do not significantly influence the morphology of the catalyst materials.

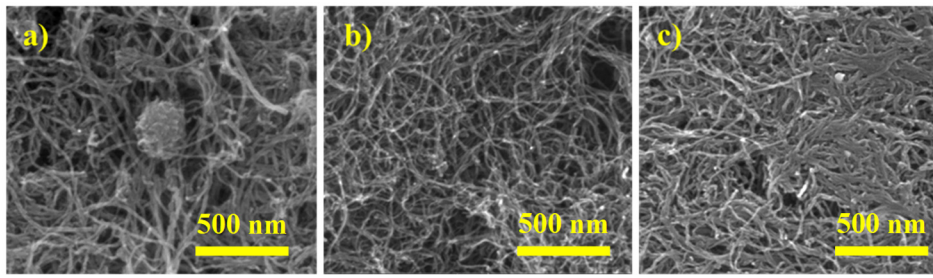

Figure 12. SEM images of (a) FeMnN-MWCNT, (b) FeCoN-MWCNT and (c) FeNiN-MWCNT catalysts.

Table 7. Elemental composition of as-synthesised catalysts determined by SEM-EDX (wt.%).

Element	FeMnN-MWCNT	FeCoN-MWCNT	FeNiN-MWCNT
C	82.6	81.7	83.6
N	5.9	8.5	6.5
O	6.9	5.0	4.7
Fe	1.9	2.5	2.9
Mn / Co / Ni	2.4	2.1	2.3

Furthermore, STEM was employed to gain further insights into the prepared catalysts (refer to Figure 13). The STEM images reveal that the metals are present in the form of nanoparticles, which appear as small clusters or bundles when viewed microscopically. As discussed in previous part (section 7.1.1.) metal nanoparticles tend to increase the electrocatalytic activity of materials in alkaline media. Upon closer inspection, fringes can be observed around these nanoparticles, providing evidence of the presence of metal nanoparticles embedded within the carbon matrix which can increase the conductivity of carbon materials [203].

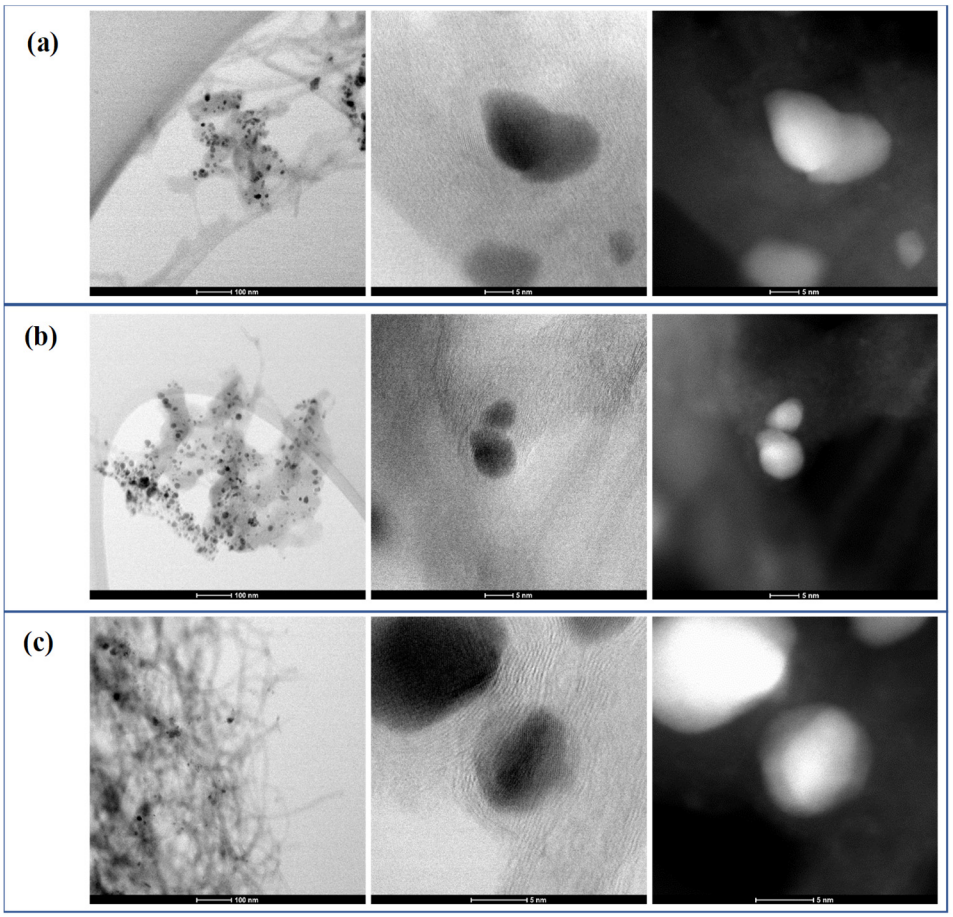

Figure 13. Bright field high-angle annular dark field (HAADF) images of (a) FeMnN-MWCNT, (b) FeCoN-MWCNT and (c) FeNiN-MWCNT materials.

The surface elemental compositions of the FeMnN-MWCNT, FeCoN-MWCNT and FeNiN-MWCNT catalysts were subjected to analysis using XPS and the findings are presented in Figure 14. The XPS analysis reveals the presence of five elements on the surface of these bimetallic catalysts, which include carbon (C), nitrogen (N), oxygen (O) and the corresponding metals. In the high-resolution XPS spectra within the N 1s region, various nitrogen species are observed, including N-graphitic, N–O, bulk N–H and M-N_x (Figure 14). In all cases of the bimetallic catalysts, N-pyridinic type nitrogen is found in the highest abundance, followed by N-pyrrolic and then M-N_x sites. It is worth noting that both N-pyridinic and M-N_x nitrogen species are considered as the most active sites for the ORR [12]. The XPS analysis provides evidence of the successful doping with MPc, as reflected in the presence of M-N_x moieties in all catalysts.

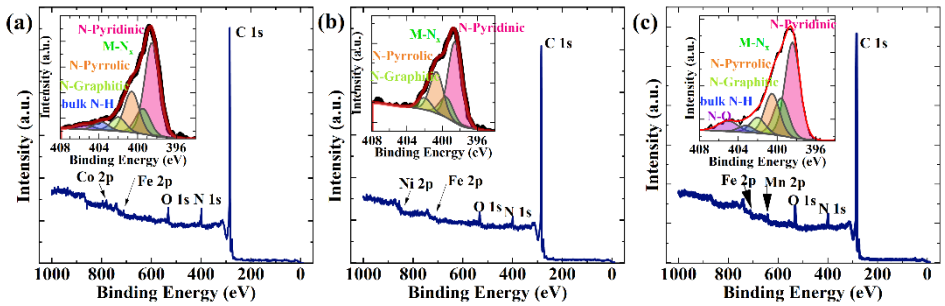

Figure 14. XPS survey spectra and N 1s high-resolution XPS spectra (inset) of (a) FeMnN-MWCNT, (b) FeCoN-MWCNT and (c) FeNiN-MWCNT.

Additionally, XRD analysis was employed to investigate the crystallographic structure of the prepared catalysts. Figure 15a presents the XRD patterns of various Fe-based catalysts. The most prominent peak, situated at approximately 25.6°, corresponds to the (002) plane of graphitic carbon [193]. Other diffraction peaks in the range of 40–50° indicate the presence of graphite, metal carbide, metal oxide and metal alloys (also visible in STEM images, Figure 13). Furthermore, Raman spectra were acquired for both pristine and as-synthesised catalysts (Figure 15b). In comparison to the unmodified MWCNTs, the pyrolysis of mixed metal phthalocyanines in conjunction with MWCNTs results in a significant broadening of the D and G bands. This broadening is attributed to the formation of defects introduced in the carbon matrix through transition-metal and heteroatom doping, as confirmed by XPS analysis. These defects contribute to the distortion of the carbon nanotube structure.

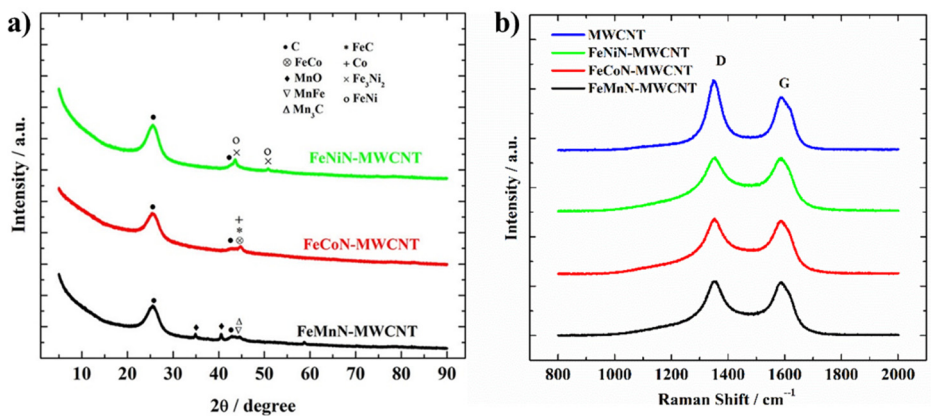

Figure 15. (a) XRD patterns and (b) Raman spectra of the as-synthesised catalysts.

The ORR activity of the catalysts was assessed in an O_2-saturated 0.1 M KOH electrolyte. To provide a benchmark for comparison, the ORR performance of

the 20 wt.% Pt/C catalyst was also evaluated under identical conditions. Initially, CV were recorded in both O_2- and Ar-saturated electrolytes (Figure 16). As demonstrated in Figure 16, all the electrocatalysts exhibit distinct ORR cathodic peaks around 0.8 V in the presence of O_2 in the 0.1 M KOH solution. However, no such peak is observed in the Ar-saturated solution. An oxidation peak in the range of 0.2 to 0.4 V has been observed, which could be associated with the formation of $Fe(OH)_2$ [204].

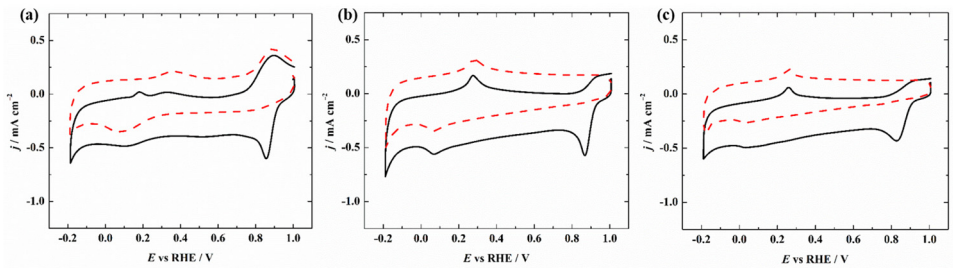

Figure 16. Cyclic voltammograms of (a) FeMnN-MWCNT, (b) FeCoN-MWCNT and (c) FeNiN-MWCNT in Ar-saturated (red dashed line) and O_2-saturated (black solid line) 0.1 M KOH electrolyte at 10 mV s^{-1}.

The ORR performance of these electrocatalysts was further investigated using the RDE method (Figure 17a). Among the mixed metal phthalocyanine-modified MWCNT catalysts, FeCoN-MWCNT exhibits the highest ORR activity in terms of E_{onset} and $E_{1/2}$. Specifically, FeCoN-MWCNT achieves an E_{onset} of 0.93 V, which is 50 mV lower than that of the 20 wt.% Pt/C catalyst (0.98 V). The E_{onset} values for FeMnN-MWCNT and FeNiN-MWCNT are 0.93 and 0.92 V, respectively (Table 8). Notably, the $E_{1/2}$ for the ORR on FeCoN-MWCNT is 0.86 V, surpassing that of the commercial 20 wt.% Pt/C catalyst ($E_{1/2}$ = 0.85 V). The excellent ORR electrocatalytic activity of the FeCoN-MWCNT catalyst can be attributed to the presence of M-N_x centres and N-pyridinic species within the prepared catalyst, as confirmed by XPS analysis. The number of electrons involved in the ORR was calculated by the K–L equation from the slopes. All the catalysts mainly follow a four-electron ORR pathway (Figure 17b).

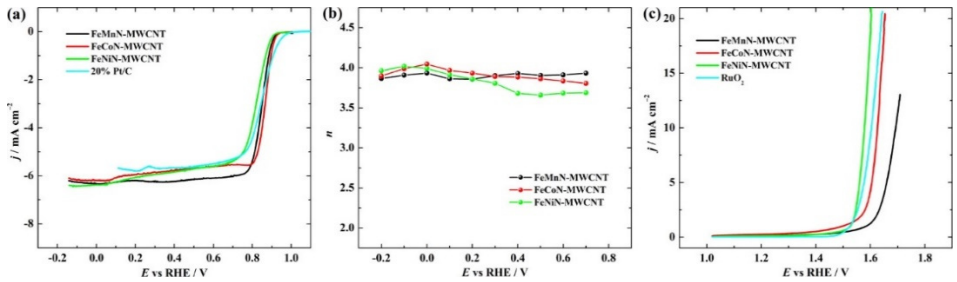

Figure 17. (a) ORR polarisation curves recorded in O_2-saturated 0.1 M KOH (v = 10 mV s^{-1}) at 1900 rpm; (b) n value as a function of potential; and (c) OER polarisation curves recorded in Ar-saturated 0.1 M KOH electrolyte (v = 10 mV s^{-1}) for prepared catalysts.

Table 8. Electrochemical results of as-synthesised catalysts.

Catalysts	E_{onset} (V)	$E_{1/2}$ (V)	$E_{j=10}$ (V)	ΔE (V)
FeMnN-MWCNT	0.93	0.85	1.69	0.84
FeCoN-MWCNT	0.93	0.86	1.63	0.77
FeNiN-MWCNT	0.92	0.82	1.58	0.76

Furthermore, the performance of all catalysts was assessed for the OER, as illustrated in Figure 17c. Among the catalysts, FeNiN-MWCNT exhibited the most remarkable OER performance, necessitating only 1.58 V to achieve 10 mA cm^{-2}. The difference between the $E_{1/2}$ for the ORR and the $E_{j=10}$ was calculated to assess the overall oxygen electrode activity (Table 8). FeNiN-MWCNT demonstrated a ΔE value of 0.76 V, while FeMnN-MWCNT and FeCoN-MWCNT had ΔE values of 0.84 and 0.77 V, respectively. Smaller ΔE values indicate that the catalyst is closer to the ideal oxygen electrode. Figure 17c and Table 8 highlight the superior OER activity of FeNiN-MWCNT. This bifunctional electrocatalytic of FeNiN-MWCNT refers to the ORR-active Fe-sites and OER-active Ni-sites [205,206]. Additionally, results for RuO_2 were obtained for comparative purposes and the $E_{j=10}$ for RuO_2 was determined to be 1.61 V.

Stability assessments were conducted to determine the catalytic stability of FeCoN-MWCNT and FeMnN-MWCNT for the ORR and FeNiN-MWCNT and FeCoN-MWCNT for the OER. After 10,000 potential cycles in O_2-saturated 0.1 M KOH solution, minimal changes of 10 and 20 mV were observed in E_{onset} and $E_{1/2}$ for both FeCoN-MWCNT and FeMnN-MWCNT, respectively. Regarding the OER stability test, chronoamperometric measurements were carried out at 1.6 V in 0.1 M KOH. The results indicated that FeNiN-MWCNT retained 82%, while FeCoN-MWCNT retained 81% of their initial OER current densities after 10,000 seconds. These findings underscore the electrochemical activity and stability of both electrocatalysts, FeCoN-MWCNT and FeNiN-MWCNT, in their respective roles for the ORR and OER.

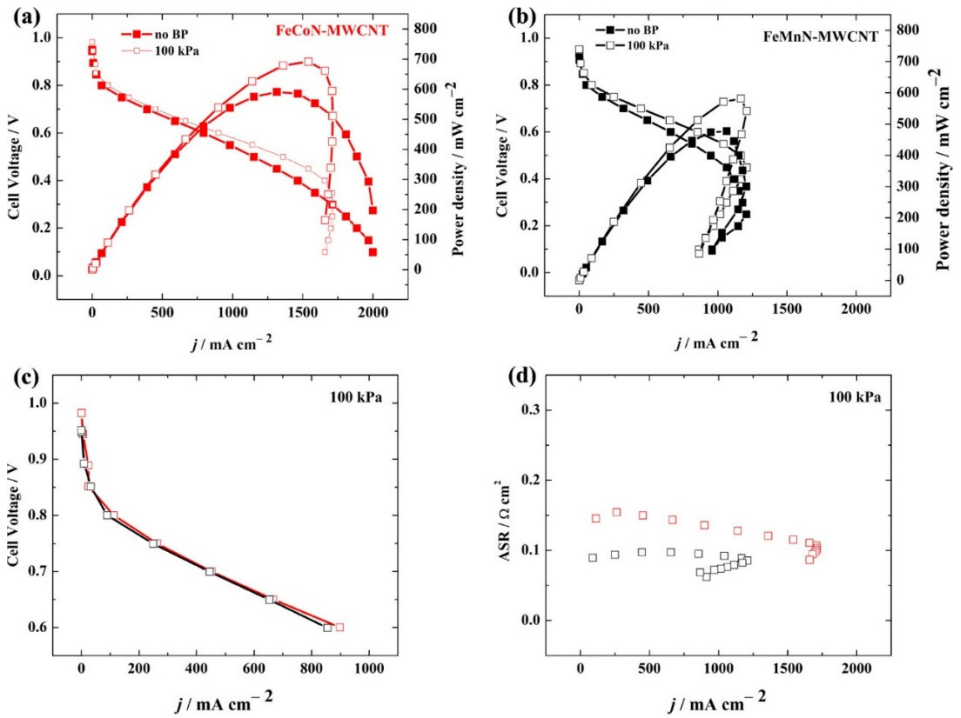

Figure 18. Polarisation and power density curves using (a) FeCoN-MWCNT and (b) FeMnN-MWCNT cathode catalysts with cell/cathode/anode temperatures of 60/58/57 °C under H_2/O_2 flows of 1 slpm at atmospheric pressure and 100 kPa back-pressurisation on both anode and cathode. (c) Comparison of catalytic and ohmic regions and (d) comparisons of the ASRs, of the AEMFCs under 100 kPa back-pressure.

Considering the promising ORR activities of FeCoN-MWCNT and FeMnN-MWCNT, we assessed their performance as cathodes in H_2-AEMFCs under similar conditions, both with oxygen (Figure 18) and air (Figure 19). A comparison of the H_2–O_2 polarisation and power density curves of the AEMFCs is presented in Figure 18a,b. At a cell temperature of 60 °C, the AEMFC using the FeCoN-MWCNT catalyst achieved the best performance under back-pressurisation. It reached a P_{max} of 692 mW cm^{-2}, a current density of 898 mA cm^{-2} at 0.6 V and an OCV of 0.98 V. The AEMFC employing FeMnN-MWCNT under the same conditions achieved a P_{max} of 582 mW cm^{-2}, a current density of 855 mA cm^{-2} at 0.6 V and an OCV of 0.95 V. To our knowledge, these power and current density values are among the highest reported in the literature for M-N_4 macrocycle-derived electrocatalysts at the cathode of AEMFC as can be seen in Table 1. Both fuel cells exhibited similar performance in the catalytic and ohmic regions of the AEMFC, as depicted in Figure 18c, with only a slight difference in current densities at 0.6 V, favouring FeCoN-MWCNT. In Figure 18d, it is evident that the area-specific resistance (ASR) in the FeMnN-MWCNT cell was slightly lower than in the FeCoN-MWCNT cell, indicating

that the membranes were adequately hydrated, allowing for efficient hydroxide conduction and water back-diffusion. In both atmospheric pressure and 100 kPa cases, the mass transport regions of the FeMnN-MWCNT did not extend to high current densities beyond 1250 mA cm^{-2}, in contrast to the FeCoN-MWCNT. It is our conjecture that further optimisation of the catalyst-coated membrane (CCM) could enhance its ability to reduce flooding and retain back-diffused water for participation in the ORR process [39]. After the acquisition of the H_2–O_2 polarisation curves, the oxidant was switched to (CO_2-free) air, while all the other fuel cell conditions were maintained. The H_2-air polarisation curves shown in Figure 19 exhibit a similar trend, wherein FeCoN-MWCNT AEMFC performed better than FeMnN-MWCNT AEMFC in terms of P_{max} and current density at 0.6 V.

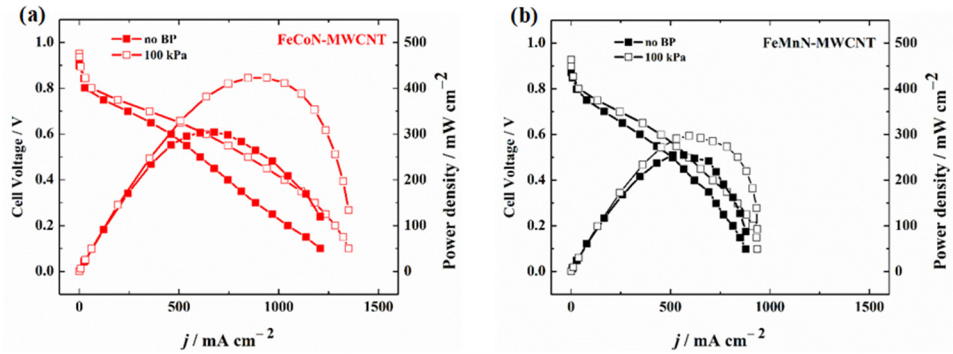

Figure 19. Polarisation and power density curves using (a) FeCoN-MWCNT and (b) FeMnN-MWCNT cathode catalyst with fuel cell/cathode/anode temperatures of 60/58/57 °C under H_2/(CO_2-free) air flows of 1 slpm at atmospheric pressure and 100 kPa back-pressurisation on both anode and cathode.

To test the performance of the FeNiN-MWCNT and RuO_2 anion-exchange membrane electrolyser (AEMEL) cells, LSV was conducted. The cells show similar response to the RDE linear sweep voltammetry (Figure 17c) in that FeNiN-MWCNT showed slightly higher current than the RuO_2 catalyst at similar catalyst loading (Figure 20a). Chronoamperometry was conducted using both FeNiN-MWCNT and RuO_2 cells at 1.8 V. The cell based on RuO_2 began with current around 110 mA cm^{-2}, but the current increased and stabilised around 140 mA cm^{-2}, possibly due to membrane break-in (Figure 20b). The observed current density of the FeNiN-MWCNT cell showed an initial current around 120 mA cm^{-2}, which decayed over 2 h to ~70 mA cm^{-2} (Figure 20b), possibly due to oxidative degradation of the FeNiN catalyst or the MWCNT substrate. In comparison with other state-of-the-art AEMEL systems, the benchmark material RuO_2 used herein has slightly lower current density than expected, for example, IrO_2 has an observed current density of 399 mA cm^{-2} under comparable conditions [207]. The lower current density is a result of un-

optimised AEMEL conditions such as ionomer:catalyst ratio, membrane thickness and GDL electrical contact/gas removal efficiency. Nonetheless, FeNiN-MWCNT compares well with the state-of-the-art RuO_2 benchmarking conducted herein and its performance assumed to be improved by further optimisation.

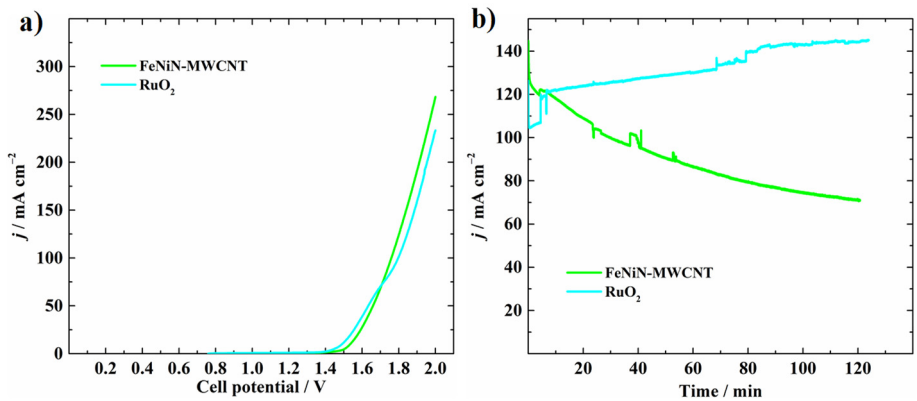

Figure 20. (a) Linear sweep voltammetry and (b) chronoamperometry of FeNiN-MWCNT and RuO_2 of MEAs conducting on VM-FAA-3-10-rf anion exchange membrane, Pt/C cathode, in 0.1 M KOH at 60 °C.

7.2. Role of carbon supports for oxygen electrocatalysis

The first chapter of this part deals with the role of carbons supports for ORR and OER in FeNi-doped carbon materials [III] in alkaline media for AEMFCs and RZABs. Carbon materials were used as support materials to increase the conductivity of prepared materials and stabilise the metal phthalocyanine structures as discussed in section 4.7. Second part deals with effect of additional nitrogen source in preparation of ORR electrocatalysts from FePc and CDC/graphene composite [IV].

7.2.1. Fe and Ni phthalocyanine-modified nanocarbon materials

In previous part, oxygen electrocatalysis on different bimetal and nitrogen-doped MWCNTs using MPc as precursors and the catalyst materials were tested in AEMFC and RZAB were studied [I, II]. The combination of FePc and NiPc based catalysts showed the highest bifunctional activity for ORR/OER among the different metal phthalocyanines. Thus, this part extended the study of bifunctional electrocatalysts by preparing the catalysts by one-step pyrolysis of a mixture of FePc and NiPc as transition metal and nitrogen sources along with different nanocarbon supports: MWCNTs, graphene, Vulcan carbon, carbide-derived carbon (CDC) and a mesoporous carbon [III].

Figure 21 displays the XRD patterns of the catalysts, revealing several important features. A broad, high-intensity diffraction peak at approximately 25.6° (2θ) is observed, corresponding to the (002) plane of graphitic carbon, while lower-intensity peaks at 44° resemble the 2H (100) graphitic carbon. Another small peak at 43.5° is attributed to the presence of FeNi alloy nanoparticles in the catalysts. In the case of FeNiN-CDC, an additional small peak at around 27° corresponds to the residual TiO_2 originating from the TiC-CDC. It is noteworthy that the annealing of metal phthalocyanines at 800 °C has led to the formation of nanoparticles, thereby enhancing the electrocatalytic activity.

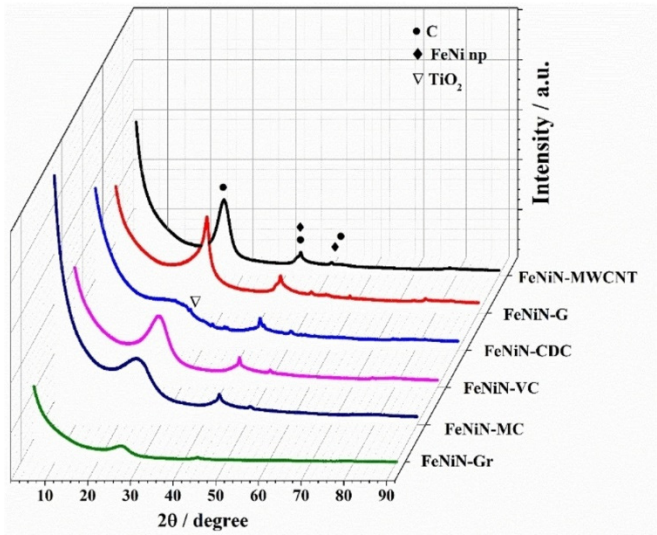

Figure 21. XRD patterns of the catalysts prepared using different nanocarbon supports.

SEM analysis was employed to reveal the surface morphology and microstructure of the prepared catalysts. The SEM micrographs, shown in Figure 22, indicate that the prepared catalysts possess surface morphology like the nanocarbon supports used in the synthesis (the data for the nanocarbon supports are not presented here). All six catalysts exhibit differences in morphology from each other. For instance, the MWCNTs display various alignments in different directions, graphene nanoplatelets and CDC particles vary in size and the Vulcan carbon particles has a characteristic spherical shape (Figure 22). Figure 22e demonstrates the morphology of the FeNiN-Gr material, characterised by significantly larger graphene flakes compared to FeNiN-G, along with observable stacking of graphene layers. This stacking may contribute to a decrease in the ORR/OER activity, as discussed in the following section. The highly porous structure of mesoporous carbon is evident in Figure 22f. The SEM images collectively indicate that the carbon supports maintain their intrinsic structure with no significant changes after pyrolysis with MPcs. Additionally, the graphitic nature of the carbon supports, as observed in MWCNT, G and Gr in

Figure 22, respectively, may facilitate better dispersion of FePc on the carbon matrix following pyrolysis. Table 9 presents the bulk elemental composition of the catalyst materials, as determined by SEM-EDX. It is apparent that Fe, Ni and N are successfully incorporated into the nanocarbon materials. The EDX mapping in SEM further reveals that Fe, Ni and N are rather uniformly dispersed on the carbon matrix, except for FeNiN-CDC and FeNiN-VC, where small clusters of Fe and Ni also observed.

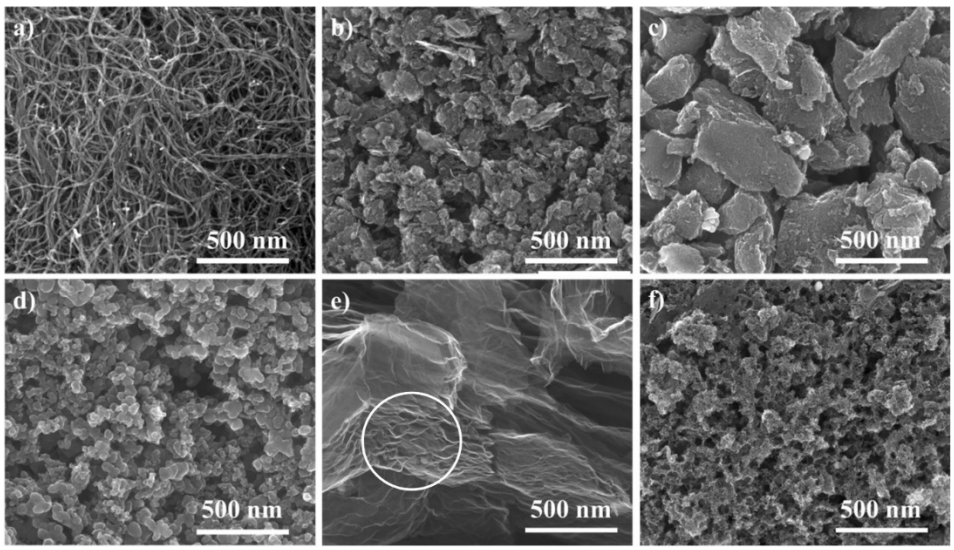

Figure 22. SEM images of (a) FeNiN-MWCNT, (b) FeNiN-G, (c) FeNiN-CDC, (d) FeNiN-VC, (e) FeNiN-Gr, circle shows the stacking of graphene layers and (f) FeNiN-MC catalysts.

Table 9. Elemental composition of the prepared catalysts determined by SEM-EDX (wt.%).

Catalyst	C	N	O	Fe	Ni
FeNiN-MWCNT	88.9	5.1	3.2	1.2	1.2
FeNiN-G	85.4	6.0	5.1	1.3	1.5
FeNiN-CDC	86.1	4.1	5.8	1.6	1.4
FeNiN-VC	89.3	4.5	3.0	1.1	1.2
FeNiN-Gr	87.2	4.7	3.5	1.1	1.2
FeNiN-MC	85.6	6.2	4.6	1.5	1.6

STEM analysis of the FeNiN-MWCNT and FeNiN-MC materials was conducted to examine the distribution of FeNi nanoparticles within the nanocarbons. As shown in Figure 23, both catalysts contain small FeNi nanoparticles in the size range from 5 to 10 nm. This structure, characterised by small-sized nanoparticles within the carbon matrix, is conducive to fast electron transport be-

tween the carbon matrix and nanoparticles [208]. Such efficient electron transport contributes to the catalysts' effectiveness in ORR/OER performance. Notably, Figure 23d demonstrates that FeNiN-MC contains larger nanoparticles, some of which can reach sizes of several tens of nanometres. In contrast, the FeNiN-MWCNT sample consistently exhibits nanoparticles with a maximum size of around 20 nm. Additionally, the STEM images reveal a mesoporous structure within the FeNiN-MC, as depicted in Figure 23c. The high-resolution STEM (HR-STEM) images show that metal nanoparticles are covered with short-range ordered, graphitised carbon (Figure 23b). It has been previously reported that transition metal or oxide phases encapsulated in graphitised carbon are considered to be conductive and significantly improve the electrocatalytic activity of catalysts [209,210]. Additionally, STEM-EDX elemental mapping has been performed to check the dispersion of metals and nitrogen in these two catalysts with high spatial resolution (Figures 23e, f). It was found that elements are rather uniformly distributed, but in some places a local increase of Fe and Ni concentration can be observed due to the formation of larger metal nanoparticles. In Figure 23, areas with increased Fe concentration also show increased Ni content, which indicates the presence of FeNi nanoparticles in the samples, in agreement with the XRD results.

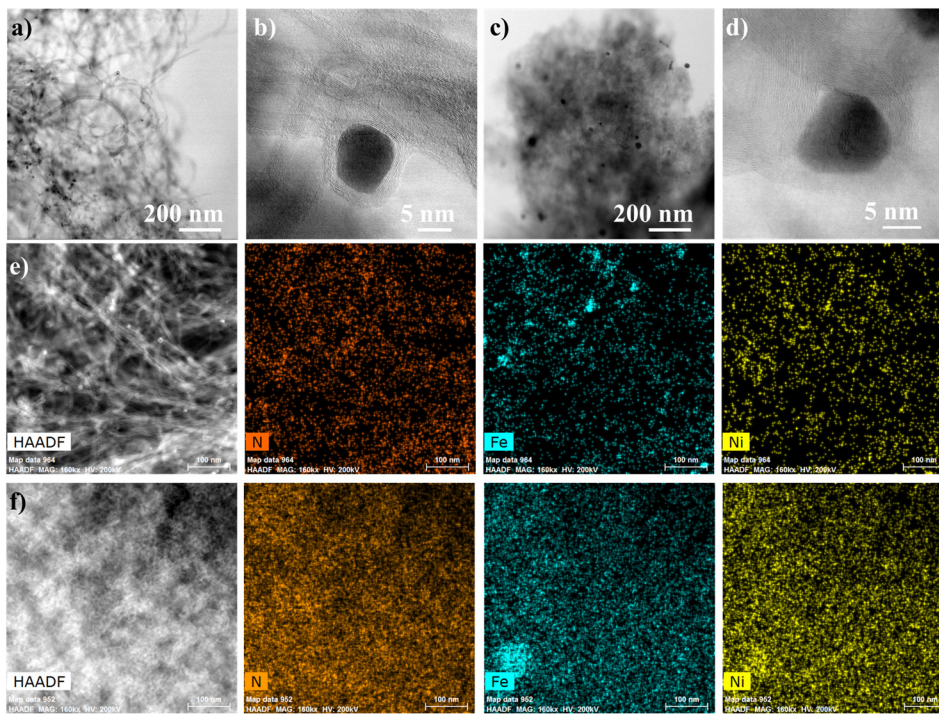

Figure 23. STEM bright field (BF) images of (a,b) FeNiN-MWCNT and (c,d) FeNiN-MC materials. HAADF-STEM and STEM-EDX mapping images of (e) FeNiN-MWCNT and (f) FeNiN-MC materials.

Surface elemental composition of the prepared catalysts was analysed using XPS. As evident from Figure 24, multiple peaks corresponding to different elements are observed, including C 1s (~284.3 eV), N 1s (~398.5 eV), O 1s (~532.9 eV), Ni 2p (854.0 eV) and Fe 2p (710.0 eV). The high-resolution XPS spectra in the N 1s region reveal the presence of various nitrogen species, primarily pyridinic-N, graphitic-N, pyrrolic-N and transition metal-coordinated N (M-N_x) (inset Figure 24). Pyridinic-N is the dominant nitrogen species. It is worth noting that M-N_x sites are known to be highly active for ORR [68]. Additionally, pyridinic-N and pyrrolic-N can significantly increase the E_{onset}, while graphitic-N can increase the limiting current density of ORR [211]. In contrast, other nitrogen species have a limited impact on the electrochemical performance of heteroatom-doped carbon materials. A noteworthy observation is the relatively low atomic percentage of M-N_x species present on the surface of FeNiN-MC and FeNiN-CDC materials compared to other catalysts. This phenomenon could be attributed to the highly porous structures of MC and CDC, which can accommodate M-N_x centres within their pores, making it challenging to detect these species via XPS. The O 1s high-resolution XPS spectra exhibit a metal oxide peak around 530.3 eV. It is suggested that the presence of metal oxide can enhance the electrocatalytic activity for both the OER and ORR [212].

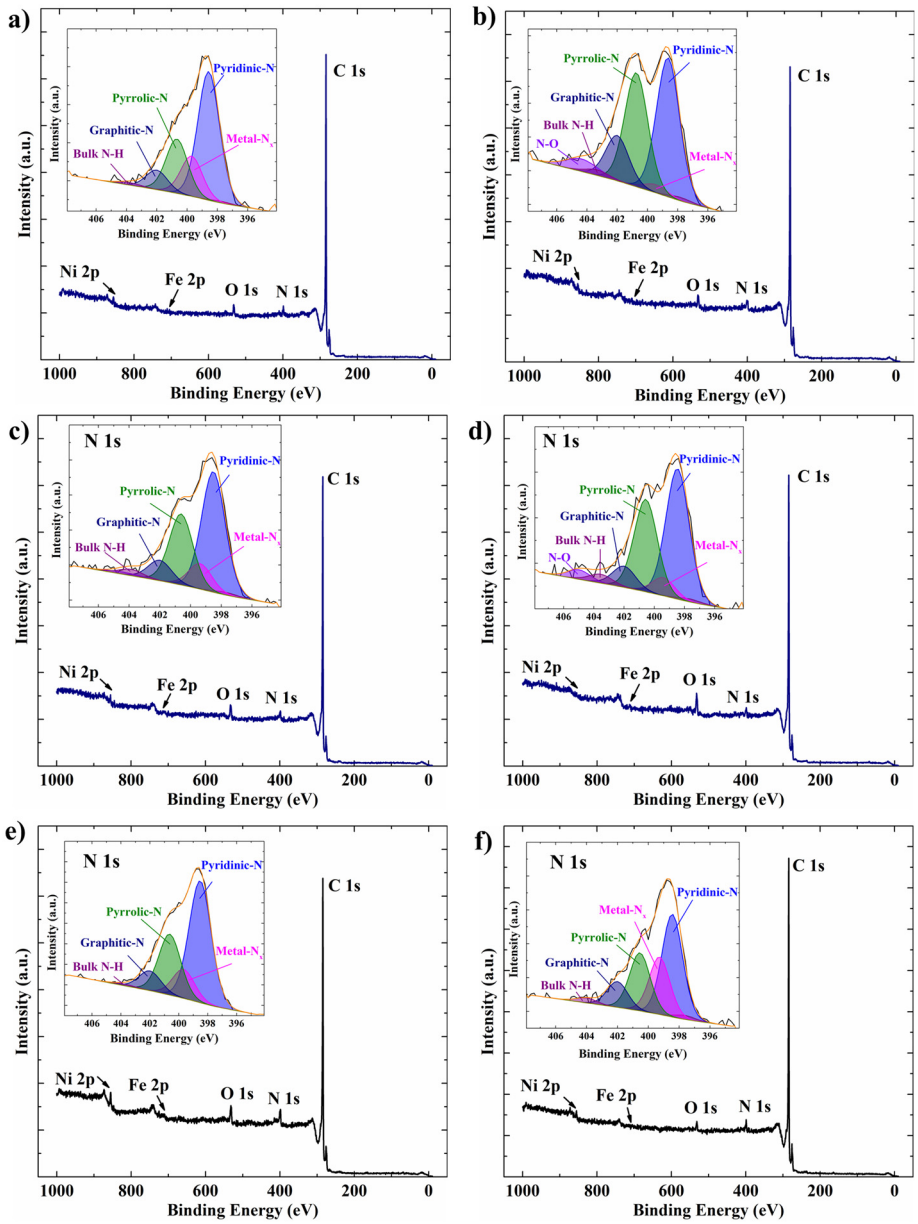

Figure 24. XPS survey spectra and N 1s high-resolution spectra (inset) of (a) FeNiN-MWCNT; (b) FeNiN-MC; (c) FeNiN-G; (d) FeNiN-CDC; (e) FeNiN-VC; and (f) FeNiN-Gr catalysts.

N_2 adsorption-desorption measurements were conducted to gain a deeper understanding of the porosity and specific surface area of all the prepared catalysts. As depicted in Figure 25, the N_2 physisorption isotherms of the catalysts display a combination of type I and III with H3 hysteresis, as per IUPAC classification,

except for FeNiN-CDC, which exhibits a type I isotherm. This hysteresis loop suggests a micro-mesoporous structure, which is not observed in FeNiN-CDC, consistent with the pore size distribution (PSD). Table 10 lists data showing the Brunauer-Emmett-Teller (BET) surface area (S_{BET}) of the catalysts. FeNiN-VC exhibits the lowest S_{BET} of 152 $m^2 g^{-1}$, followed by FeNiN-MWCNT (231 $m^2 g^{-1}$), FeNiN-G (364 $m^2 g^{-1}$), FeNiN-MC (464 $m^2 g^{-1}$), FeNiN-Gr (477 $m^2 g^{-1}$) and FeNiN-CDC (675 $m^2 g^{-1}$). It is evident that the S_{BET} of the catalysts was reduced to half that of the corresponding carbon support after the successful doping with metal phthalocyanines (details not shown). The PSD plot in Figure 25 highlights that FeNiN-CDC primarily possesses a microporous structure with average pore size of 0.85 nm. However, the other catalyst materials show variety of pores, with distribution centred around approximately 1 nm and 3–5 nm. The broader pore size distribution of mesopores between 10–30 nm is more pronounced in FeNiN-MWCNT, FeNiN-MC and FeNiN-Gr. Comparing the total pore volume (V_{tot}) and micropore volume (V_{μ}) of the catalysts, it is evident that FeNiN-MC and FeNiN-Gr have the largest pore volume (V_{tot}=~0.99 $cm^3 g^{-1}$), followed by FeNiN-G, FeNiN-MWCNT, FeNiN-CDC and FeNiN-VC. Additionally, the percentage of pore volume corresponding to micropores indicates that FeNiN-CDC (57.5%) primarily consists of micropores (Table 10). In contrast, FeNiN-MC, FeNiN-G, FeNiN-Gr, FeNiN-VC and FeNiN-MWCNT consist mainly of mesopores with a smaller proportion of micropores, as revealed in the PSD graph.

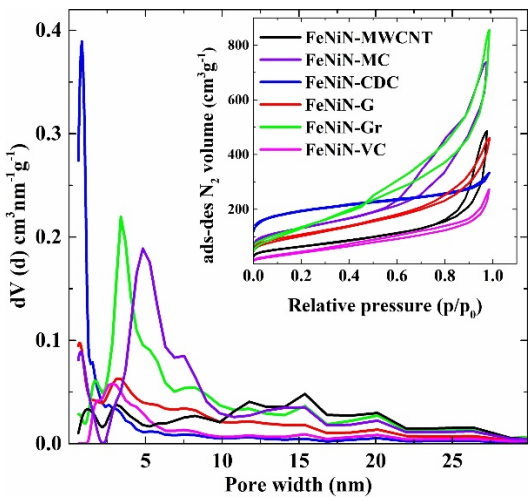

Figure 25. Pore size distribution and N_2 sorption isotherms (inset) of prepared catalysts.

Table 10. Specific surface area (S_{BET} and S_{dft}), total pore volume (V_{tot}) and micropore volume (V_{μ}) of the catalysts.

Catalyst	S_{BET} ($m^2 g^{-1}$)	S_{dft} ($m^2 g^{-1}$)	V_{tot} ($cm^3 g^{-1}$)	V_{μ} ($cm^3 g^{-1}$)	(%) of V_{μ}
FeNiN−MWCNT	231	195	0.58	0.04	6.9
FeNiN−G	364	359	0.6	0.09	15
FeNiN−CDC	675	671	0.47	0.27	57.5
FeNiN−VC	153	137	0.33	0.02	6
FeNiN−Gr	477	429	0.99	0.06	6
FeNiN−MC	464	454	0.98	0.08	8.2

To assess the ORR electrocatalytic activity of the prepared catalysts derived from the supports, CV was conducted in O_2 and Ar-saturated 0.1 M KOH aqueous solution at a scan rate of 10 mV s^{-1}. All the prepared catalysts display well-defined cathodic reduction peaks around 0.9 V in the O_2-saturated solution, indicating significant electrocatalytic activity for the ORR. For a more in-depth investigation of the ORR activity, LSVs were recorded using the RDE method in O_2-saturated 0.1 M KOH solution at various rotation rates (Figure 26a,c). As demonstrated in Figure 26, the RDE polarisation curves for FeNiN−MWCNT and FeNiN−MC catalysts exhibit a expected increase in current density with higher rotation rates (from 360 to 3100 rpm).

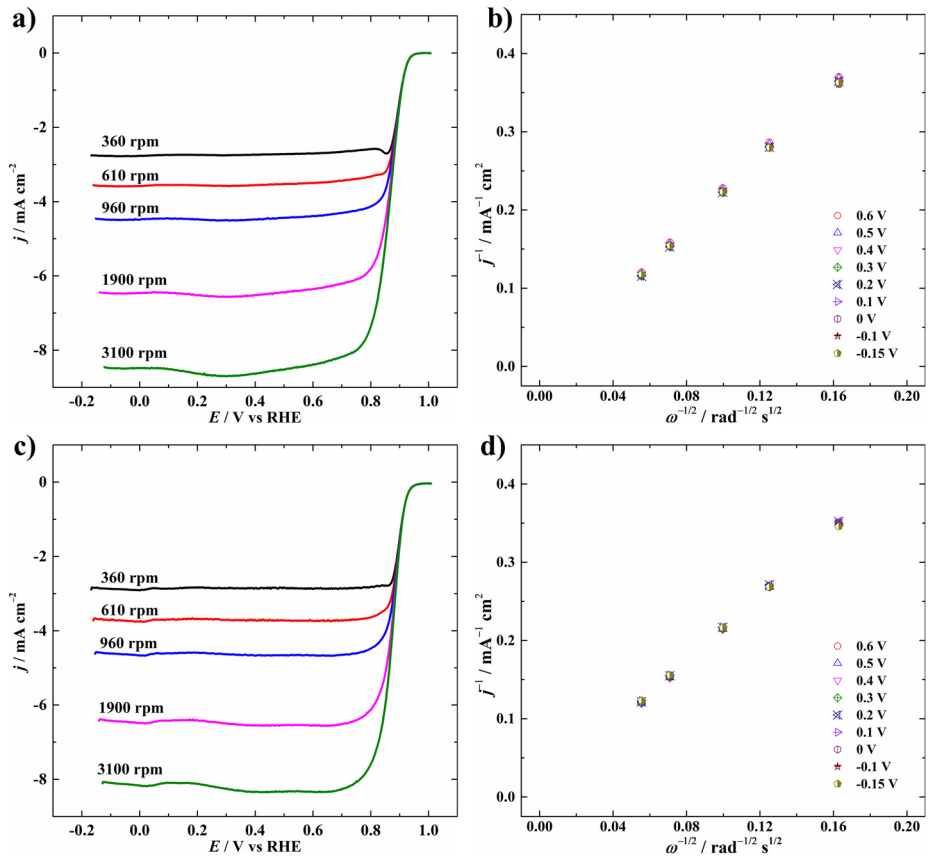

Figure 26. (a, c) ORR polarisation curves recorded at different rotation rates and (b, d) K-L plots for (a, b) FeNiN−MWCNT and (c, d) FeNiN−MC catalysts in O_2-saturated 0.1 M KOH (v=10 mV s^{-1}).

The K-L plots at different potentials are provided in Figures 26b and c. These plots were employed to compute the electron transfer number associated with the ORR. The K-L plots exhibit linear behaviour and their slopes remain relatively constant across the potential range from −0.15 to 0.6 V. This suggests that the number of electrons transferred per O_2 molecule at different potentials, remains almost the same for all the catalysts, with a value of 4 (Figure 27a, inset).

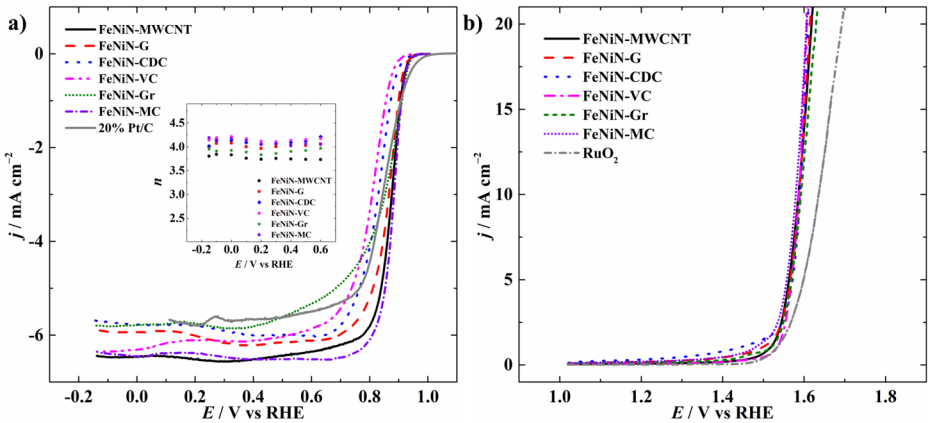

Figure 27. (a) ORR polarisation curves recorded at 1600 rpm in O_2-saturated 0.1 M KOH (v=10 mV s^{-1}), number of transferred electrons per O_2 molecule as a function of potential (inset); and (b) OER polarisation curves in Ar-saturated 0.1 M KOH (v= 10 mV s^{-1}).

Figure 27 displays a comparison of the LSV curves at 1600 rpm for O_2 reduction for all the catalysts in addition to 20% Pt/C. FeNiN-MWCNT and FeNiN-MC catalysts exhibit $E_{1/2}$ of 0.87 and 0.88 V, respectively, which outperform FeNiN-G (0.86 V), FeNiN-CDC (0.83 V), FeNiN-VC (0.81 V) and FeNiN-Gr (0.85 V). Three electrocatalysts, namely, FeNiN-MWCNT, FeNiN-G and FeNiN-MC, demonstrate the ORR activity comparable to the commercial Pt/C catalyst ($E_{1/2}$ = 0.88 V), indicating similar ORR performance to the benchmark Pt/C catalyst. The observed trend in the ORR electrocatalytic activity of the prepared catalysts can be attributed to the metal and nitrogen concentration as well as the pore structure of the catalysts. FeNiN-MC has the highest transition metal and nitrogen content, followed by FeNiN-G, FeNiN-MWCNT, FeNiN-Gr, FeNiN-VC and FeNiN-CDC, which aligns with the ORR activity trend ($E_{1/2}$ and E_{onset} values) except for FeNiN-Gr. The slightly lower ORR activity of FeNiN-Gr can be attributed to the tendency of graphene nanosheets to restack, which is observable in the SEM image and decreases the number of electrocatalytically active sites for ORR. FeNiN-VC exhibits the lowest ORR performance compared to other porous catalysts, namely, FeNiN-CDC and FeNiN-MC. This could be due to the moderate specific surface area of FeNiN-VC (S_{BET} of ~152 m^2 g^{-1}, as listed in Table 10), which might limit the dispersion of metal phthalocyanine and lead to particle agglomeration (Figure 23). Notably, FeNiN-CDC, despite its high microporosity, displayed lower ORR activity than FeNiN-MC, FeNiN-G and FeNiN-Gr, indicating that the extensive presence of micropores might not significantly contribute to improving the ORR activity due to limited accessibility of reactants to the active sites within these micropores. Although high surface area and mesoporous structure of carbon supports are typically associated with enhanced ORR activity, the presence of graphitic

carbon also plays a crucial role in the preparation of transition metal macrocycle-derived catalysts. The importance of graphitic carbon supports becomes apparent when comparing FeNiN-MWCNT and FeNiN-MC catalysts. Despite having only half the S_{BET} of FeNiN-MC, FeNiN-MWCNT exhibits comparable ORR electrocatalytic activity. This can be attributed to the superior interaction between MPcs and the graphitic carbon structure of MWCNT through π-π interactions during the catalyst preparation process, which facilitates the even distribution of active sites.

Subsequently, LSV measurements were performed within a potential range from 1.0 to 1.8 V in Ar-saturated 0.1 M KOH solution to assess the OER activity of the catalysts. As illustrated in Figure 27b, the polarisation curves of all the catalysts exhibit comparable OER electrocatalytic activity with a slightly lower $E_{j=10}$ value when compared to RuO_2 (1.63 V). This similarity in OER performance could be attributed to a similarity in the density of active sites. Investigating active sites in such catalysts is a complex task. Nevertheless, previous literature suggests that metallic particles or oxides can significantly enhance OER electrocatalytic activity [194,195,199,212]. Therefore, it is plausible that the FeNi nanoparticles and metal oxides in the prepared catalysts serve as active sites for the OER, in addition to M-N_x centres. These results indicate that the choice of different carbon support materials has a negligible effect on the OER activity, as evidenced by the comparable $E_{j=10}$ value of 1.59 V among the catalysts.

Table 11. Tafel slopes (mV dec^{-1}) of the prepared catalysts for ORR and OER in 0.1 M KOH solution.

Catalyst	**ORR**	**OER**
FeNiN-MWCNT	−31	62
FeNiN-G	−41	66
FeNiN-CDC	−65	60
FeNiN-VC	−50	59
FeNiN-Gr	−35	65
FeNiN-MC	−32	59
20% Pt/C	−67	-
RuO_2	-	88

For a more comprehensive understanding of the ORR and OER activities of the prepared catalysts, Tafel plots derived from the LSV curves for both the ORR and OER are depicted and the results are summarised in Table 11. In the case of the ORR, the Tafel slope values were found to be the smallest for FeNiN−MWCNT (−31 mV dec^{-1}), followed by FeNiN−Gr, FeNiN−G and FeNiN−MC, all of which exhibited similar slope values. These results suggest a shared reaction mechanism among these catalysts. On the other hand, FeNiN−VC and FeNiN−CDC showed higher Tafel slope values of −50 and

−65 mV dec^{-1}, respectively. These small Tafel slopes are characteristic of catalysts containing iron, signifying a redox-mediated electrocatalysis with a fast one-electron transfer involving Fe(III) to Fe(II) [213,214]. This process generates the Fe(II) active site at low current densities during the negative potential scan, occurring prior to the rate-determining step. These findings are consistent with the involvement of a redox process at Fe centres. The higher Tafel slopes observed, particularly the −65 mV dec^{-1} Tafel slope, may be attributed to the presence of Ni centres, which do not exhibit the fast Ni(III)/(II) redox processes and likely contribute to the ORR through a different mechanism. Therefore, the −65 mV dec^{-1} Tafel slope likely reflects the occurrence of parallel ORR processes at both Fe and Ni centres. In contrast, the lower Tafel slopes of −31 and −40 mV dec^{-1} indicate a preference for the ORR to proceed predominantly at Fe centres. Analogously to the ORR results, Tafel slope values for OER were found to be quite similar and close to 60 mV dec^{-1}, which suggest that the OER on these catalysts follows similar reaction mechanism and M−O formation (2nd step) is the rate-determining step. These Tafel slope values well matched with the previously reported works where the OER proceeds preferentially at Ni centres however Fe plays a beneficial role to increase the OER activity along with Ni centres.

To assess the suitability of electrocatalysts for practical applications in fuel cells and metal-air batteries, their stability for both the ORR and OER is of utmost importance. In this context, FeNiN−MWCNT and FeNiN−MC catalysts were chosen for durability testing, focusing on the ORR and OER stability. An ADT was carried out for the ORR by subjecting the catalysts to repeat potential cycling. As depicted in Figures 28a and c, minimal changes in the $E_{1/2}$ values were observed for both catalysts after 10,000 potential cycles. The $E_{1/2}$ value changed by only 9 mV for FeNiN−MC and 10 mV for FeNiN−MWCNT. These results demonstrate the excellent stability of these catalysts for the ORR in an alkaline environment. The OER stability of the catalysts was also investigated by subjecting them to 1000 cycles in an Ar-saturated 0.1 M KOH (Figures 28b,d). Interestingly, FeNiN−MWCNT exhibited better stability, with a $\Delta E_{j=10}$ of 16 mV, compared to FeNiN−MC, which had a $\Delta E_{j=10}$ of 46 mV. This finding suggests that FeNiN−MWCNT is more stable for the OER, emphasising its potential for practical applications. Overall, the results indicate that both FeNiN−MWCNT and FeNiN−MC materials are promising candidates for use in fuel cells and metal-air batteries, offering excellent stability for both the ORR and OER processes.

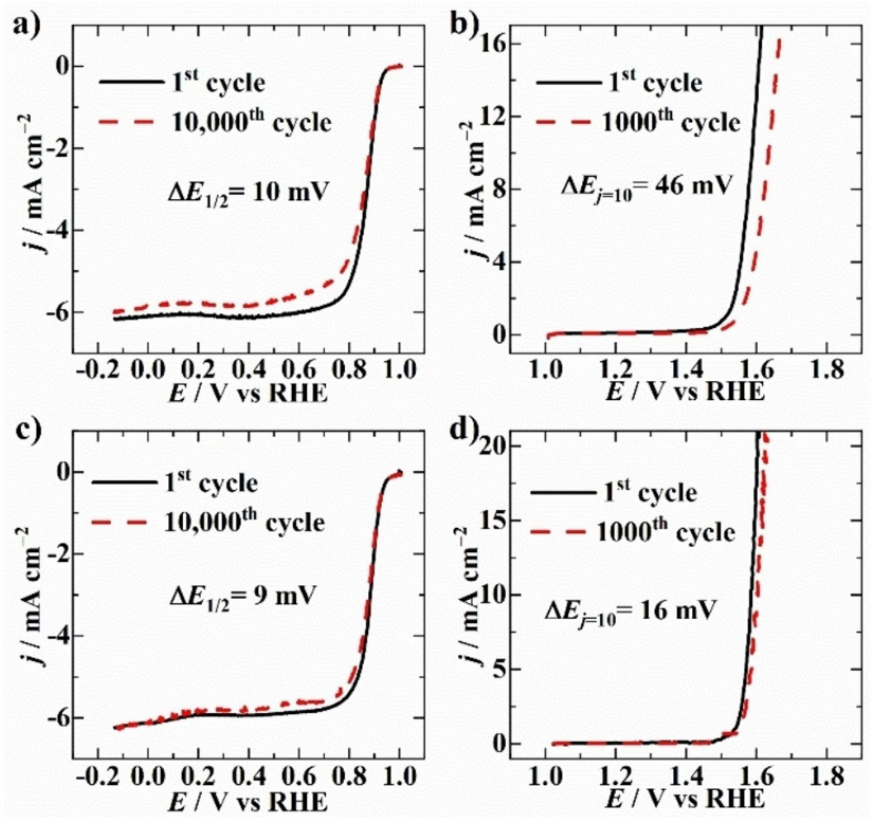

Figure 28. ORR polarisation curves before and after stability test of (a) FeNiN−MC and (c) FeNiN−MWCNT in O_2-saturated 0.1 M KOH; OER polarisation curves before and after stability test of (b) FeNiN−MC and (d) FeNiN−MWCNT in Ar-saturated 0.1 M KOH. v=10 mV s^{-1}, ω=1900 rpm.

Evaluating the performance of the prepared catalysts in fuel cells is a crucial benchmark for assessing their practical applicability. Single-cell fuel cell polarisation and power density curves for FeNiN−MWCNT and FeNiN−MC were conducted in an AEMFC test and the results are presented in Figure 29. For comparison, the Pt/C catalyst was also tested under similar AEMFC conditions. FeNiN−MC exhibited an open-circuit voltage (OCV) of 1.0 V, which was slightly higher than the OCV observed with FeNiN−MWCNT (0.96 V). In terms of current density at 0.6 V, FeNiN−MC reached 528 mA cm^{-2}, while FeNiN−MWCNT achieved a higher value of 638 mA cm^{-2}, representing a 100 mA cm^{-2} advantage over FeNiN−MC and Pt/C. Furthermore, FeNiN−MWCNT demonstrated a P_{max} of 406 mW cm^{-2}, surpassing the performance of FeNiN−MC (386 mW cm^{-2}) and Pt/C (347 mW cm^{-2}). Analysing AEMFC performance compared to existing literature results is challenging due to variations in experimental conditions, such as the use of different anion

exchange membranes, catalyst morphologies and water management strategies. The slight decrease in AEMFC performance for FeNiN−MC compared to FeNiN−MWCNT may be attributed to various factors, including the choice of AEM, the morphology of the catalysts and water management strategies, etc.

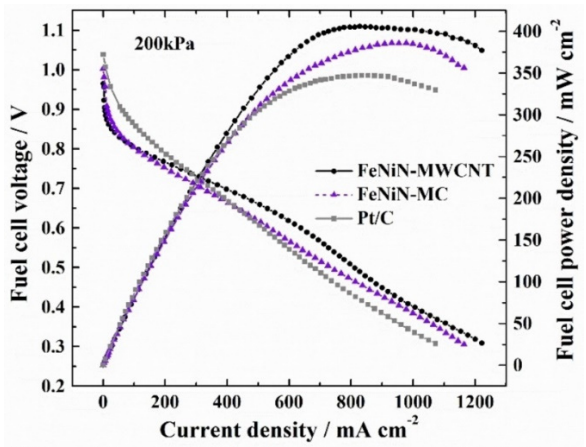

Figure 29. Polarisation curves and power densities for H_2−O_2 AEMFC using AF2-HLE8-10-X anion exchange membrane, Pt−Ru/C as anode catalyst and FeNiN−MWCNT, FeNiN−MC and Pt/C as cathode catalysts. T=65 °C. H_2 and O_2 flow rate is 1 NLPM.

RZABs were fabricated and tested to assess the bifunctional electrocatalytic performance of FeNiN−MWCNT and FeNiN−MC catalyst materials. Figure 30a presents the discharge polarisation curves and corresponding power density curves for different catalysts. FeNiN−MC displayed an impressive OCV value of 1.47 V, while FeNiN−MWCNT achieved 1.45 V. Remarkably, FeNiN−MWCNT exhibited a P_{max} of 84.5 mW cm^{-2}, surpassing both Pt−Ru/C (80.7 mW cm^{-2}) and FeNiN−MC (71.9 mW cm^{-2}) catalysts. However, it is important to note that the NPMCs had twice the catalyst loading on the electrode compared to Pt−Ru/C. Furthermore, the durability of these catalysts, along with the benchmark Pt−Ru/C, was assessed through a galvanostatic charge-discharge cycling test, operated at a current density of 1 mA cm^{-2} (Figure 30b). FeNiN−MWCNT demonstrated superior cycling performance compared to FeNiN−MC and Pt−Ru/C under the same conditions. The initial voltage gap between charge and discharge potential for FeNiN−MWCNT and FeNiN−MC catalysts was 0.58 and 0.55 V, respectively. After 48 h, FeNiN−MWCNT exhibited only slight performance degradation (0.05 V increase in voltage gap). In contrast, FeNiN−MC experienced a larger increase in voltage gap (0.2 V). The enhanced stability of FeNiN−MWCNT can be attributed to the graphitic structure of MWCNTs. TEM images revealed that some metal nanoparticles were encapsulated within MWCNTs, reducing the risk of demetallation in highly alkaline media. This factor likely contributes to the

better stability of FeNiN−MWCNT in RZABs. FeNiN−MWCNT and FeNiN−MC catalysts exhibited comparable OCV values to previously reported RZABs. However, the P_{max} of these materials varied among different RZABs, as multiple factors, including electrode distance, electrolyte concentration, air flow, zinc anode, cathode materials, etc., can influence the performance of RZABs.

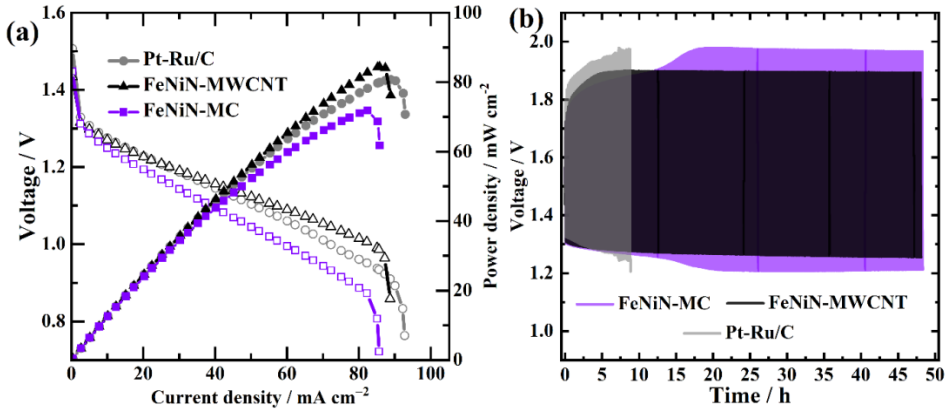

Figure 30. (a) Polarisation and power density curves of the Pt−Ru/C, FeNiN−MWCNT and FeNiN−MC catalysts for discharging. (b) Galvanostatic discharge-charge cycling curves for ZABs with Pt−Ru/C, FeNiN−MC and FeNiN−MWCNT.

7.2.2. Fe and N-doped CDC/G composite material for ORR

The surface morphology of the materials characterised by SEM. Figures 31a,c,e reveal similar morphological structures. Upon closer inspection, one can observe a relatively homogeneous composite of CDC and graphene. CDC particles seem to be interspersed among or deposited on the graphene nanoflakes (Figure 31b,d,e). Additionally, SEM-assisted EDX analysis was performed to determine the bulk concentration of elements and the results are presented in Table 12. The iron content was found to be the same in both iron-containing materials. However, a significantly higher nitrogen content was detected in FeN-CDC/G/DCDA compared to FeN-CDC/G. The increased nitrogen content can be advantageous for stabilising metal particles on the carbon matrix, leading to enhanced electrocatalytic activity and stability.

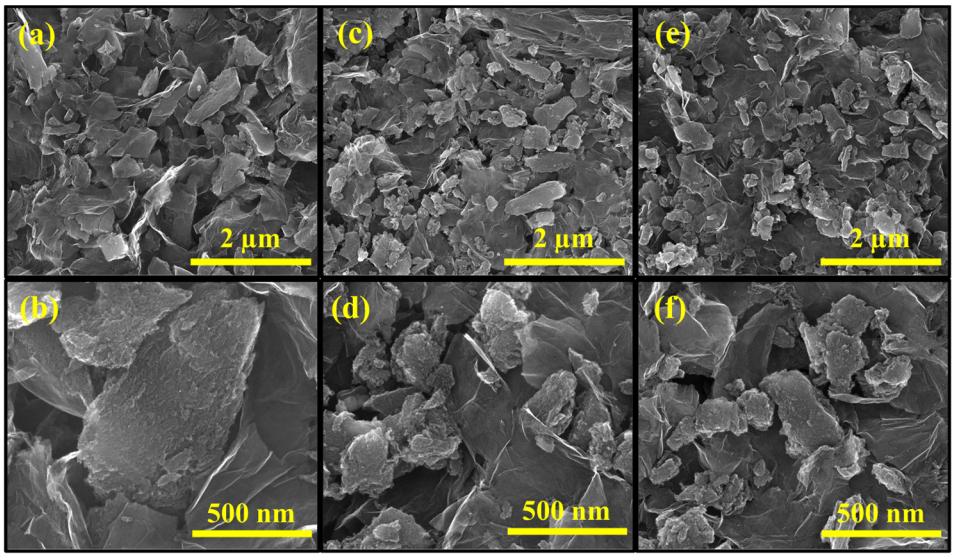

Figure 31. SEM images of (a, b) N-CDC/G/DCDA, (c, d) FeN-CDC/G and (e, f) FeN-CDC/G/DCDA catalysts.

Table 12. Elemental composition of the prepared catalysts determined by SEM-EDX (wt.%).

Catalyst	C	N	O	Fe
FeN-CDC/Gr/DCDA	82.8	8.9	4.7	1.9
FeN-CDC/Gr	88.2	3.5	4.9	1.7
N-CDC/Gr/DCDA	88.9	4.3	3.5	-

Moreover, for further analysis of Fe-containing materials, STEM was employed and the results are displayed in Figure 32. The structure of the CDC/G composite is visible in Figure 32a,d. Both FeN-CDC/G/DCDA and FeN-CDC/G materials contain Fe nanoparticles. Nevertheless, FeN-CDC/G contains significantly larger Fe nanoparticles (approximately 50 nm in size), while FeN-CDC/G/DCDA comprises only 5 nm Fe nanoparticles (Figure 32b,e). The inclusion of DCDA as a nitrogen source aids in preventing the aggregation of Fe nanoparticles during the pyrolysis process. These smaller nanoparticles can offer a higher number of active sites for the ORR, as is evident in Figure 32e,f. In FeN-CDC/G catalyst, Fe nanoparticles are larger and tend to aggregate in one region, while in FeN-CDC/G/DCDA, the nanoparticles are more uniformly distributed and smaller in size. Additionally, a higher nitrogen content is observable in FeN-CDC/G/DCDA compared to FeN-CDC/G.

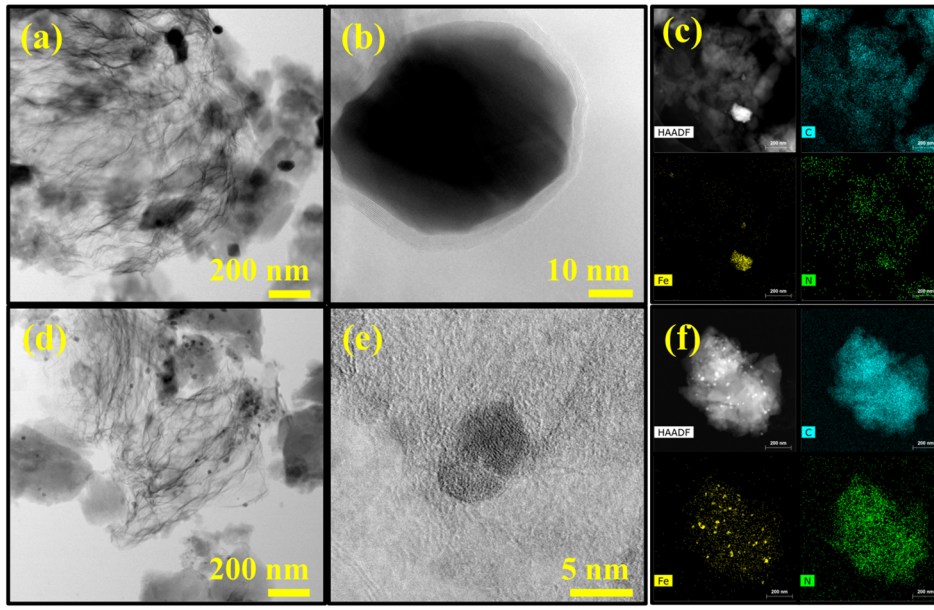

Figure 32. STEM images of (a, b) FeN-CDC/G and (d, e) FeN-CDC/G/DCDA. Elemental mapping of (c) FeN-CDC/G and (f) FeN-CDC/G/DCDA catalysts.

XRD analysis was employed for characterising the materials' structure. Similar to previous parts, the presence of peaks at approximately $2\theta = 25°$ and 43°, which are indicative of graphitic carbon. Other peaks at $2\theta = 37°$ and 61° is attributed to titanium carbide, which is from CDC. These peaks are found in the materials due to the use of ZrO_2 balls in the ball-milling of CDC. Furthermore, additional diffraction peaks at approximately 44° can be associated with the existence of Fe_3C and Fe nanoparticles in FeN-CDC/G, while there was no observable Fe nanoparticle phase.

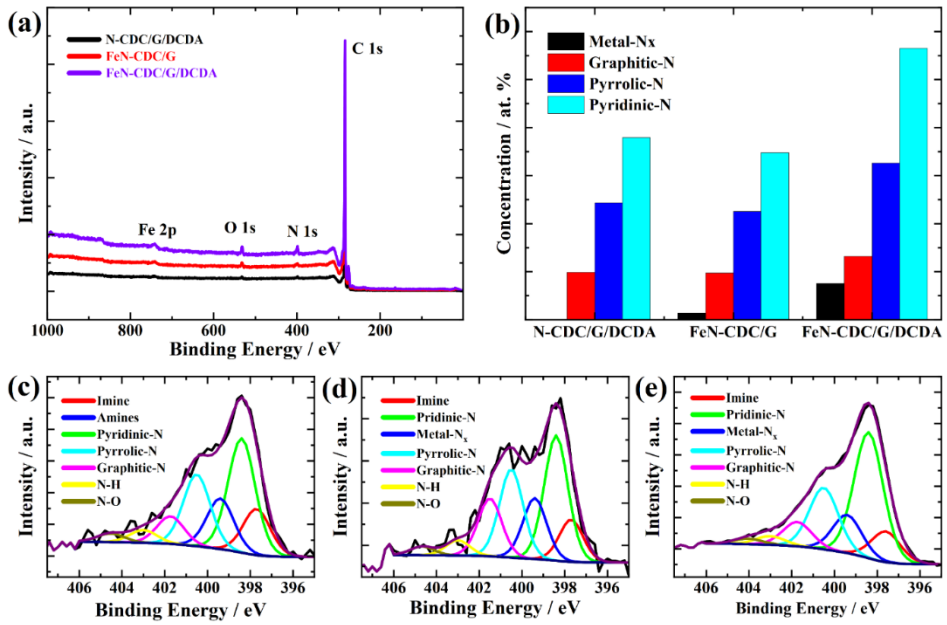

Figure 33. (a) XPS survey spectra of prepared materials. (b) Graphical representation of N-species surface concentration in prepared materials. High-resolution N 1s XPS spectra of (c) N-CDC/G/DCDA, (d) FeN-CDC/G and (e) FeN-CDC/G/DCDA catalysts.

The composition and chemical state of surface elements in the prepared materials were assessed through XPS analysis. The comprehensive XPS survey spectra of the prepared materials reveal the presence of carbon, nitrogen, oxygen and iron in both FeN-CDC/G and FeN-CDC/G/DCDA (Figure 33a). Figure 33b provides the atomic concentration of nitrogen species within the prepared materials. Notably, N-CDC/G/DCDA lacks any M-N_x species and the quantity of this specie increases in the following order: N-CDC/G/DCDA < FeN-CDC/G < FeN-CDC/G/DCDA. Furthermore, the most prominent nitrogen species in all three materials is pyridinic-N, followed by pyrrolic-N, graphitic-N and M-N_x. As previously discussed in the introduction, these nitrogen species play a pivotal role in enhancing the ORR activity. In Figure 33c,d,e, we present high-resolution N 1s XPS spectra for N-CDC/G/DCDA, FeN-CDC/G and FeN-CDC/G/DCDA, respectively. The N 1s spectra were analysed and resolved into seven peaks: oxidic-N (N-O, 404 eV), N-H (403 eV), graphitic-N (401.7 eV), pyrrolic-N (400.5 eV), metal-N (399.4 eV), pyridinic-N (398.4 eV) and imine-N (397.6 eV). The additional nitrogen source, DCDA, contributed to an increase in pyridinic, pyrrolic, graphitic and M-N_x species. The presence of pyridinic-N assists in charge-transfer and is able to induce electronic structural changes in the neighbouring carbon atoms, resultantly facilitating the oxygen adsorption, while graphitic-N contributes to enhancing the limiting diffusion current, thus boosting electrocatalytic activity [215].

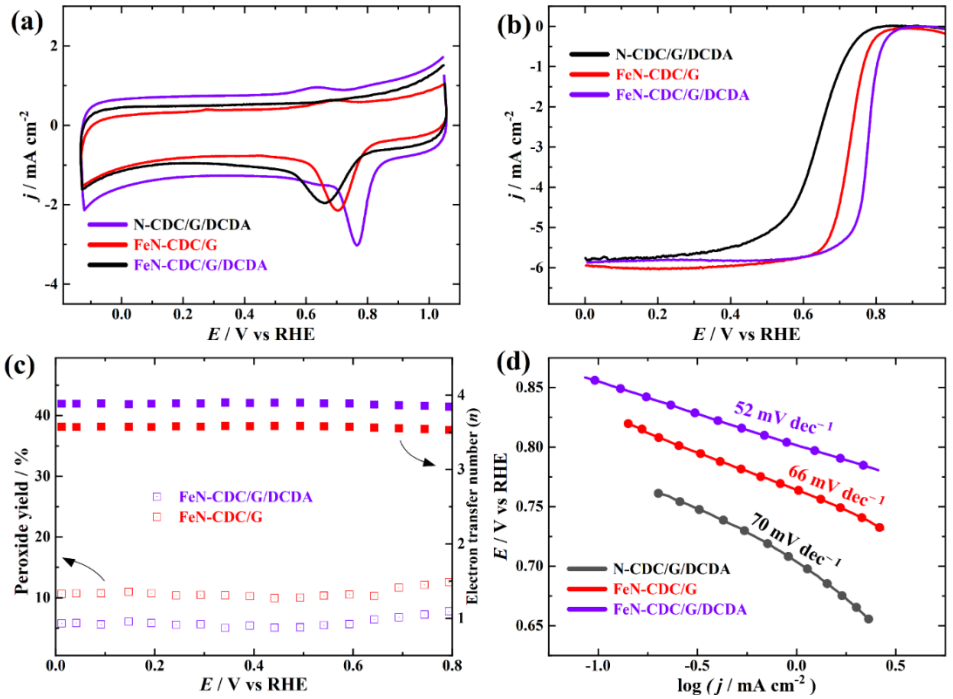

Figure 34. (a) Comparison of CVs at 100 mV s^{-1}, (b) ORR polarisation curves of prepared materials at 1900 rpm, (c) hydrogen peroxide yield and number of transferred electrons as a function of potential, (d) Tafel plots derived from the ORR polarisation curves in oxygen-saturated 0.5 M H_2SO_4 at 10 mV s^{-1}.

After physical characterisation, the electrocatalytic performance of the prepared materials for the ORR was measured in O_2-saturated 0.5 M H_2SO_4 electrolyte. Figure 34a displays the CV curves in an oxygen-saturated electrolyte for the prepared materials. All electrocatalysts exhibit distinct cathodic peaks attributed to the ORR. In the absence of iron, N-CDC/G/DCDA shows a current peak at 0.65 V, whereas the CDC/G composite doped with FePc shifts the peak position towards a more positive value at 0.70 V. Notably, when the composite is doped with iron phthalocyanine in conjunction with DCDA, the ORR peak position further shifts in a positive direction to 0.76 V, indicating a further enhancement in the ORR activity.

The ORR performance of the catalysts was further examined using the rotating ring-disk electrode method and the results in the form of LSV plots are presented in Figure 34b. Notably, both FeN-CDC/G/DCDA and FeN-CDC/G catalysts exhibit superior ORR electrocatalytic activities compared to N-CDC/G/DCDA, as evidenced by their onset potential and half-wave potential. In particular, the FeN-CDC/G/DCDA catalyst demonstrates the highest ORR activity, displaying a more positive E_{onset} of 0.85 V vs. RHE, as well as a higher $E_{1/2}$ of 0.76 V vs. RHE. These values surpass those of the FeN-CDC/G catalyst (0.83 and 0.70 V vs. RHE) and N-CDC/G/DCDA (0.78 and 0.65 V vs. RHE).

The exceptional ORR performance of the FeN-CDC/G/DCDA catalyst can be attributed to its higher number of Fe-N_x active sites and nitrogen doping, which were expected to enhance its electrocatalytic activity. Furthermore, FeN-CDC/G/DCDA also features smaller Fe nanoparticles than FeN-CDC/G, which could be a contributing factor to its superior ORR performance.

In order to further investigate and verify the ORR catalytic pathways of these materials, we also conducted RRDE measurements to monitor the formation of hydrogen peroxide during the ORR process. The results depicted in Figure 34c demonstrate the H_2O_2 formation yield and the *n* value. FeN-CDC/G catalyst exhibited a higher peroxide production, approximately 10% in a wide potential range, while the FeN-CDC/G/DCDA catalyst displayed nearly half the yield of peroxide formation (~5%). Furthermore, the number of transferred electrons for both catalysts was calculated, showing the value of *n* close to 4. However, FeN-CDC/G had a slightly lower *n* value, around 3.5, than FeN-CDC/G/DCDA (*n*=3.9). This indicates that the ORR process on both catalysts follows a 2×2 electron pathway, in which H_2O_2 acts as an intermediate that is subsequently reduced to water. Notably, FeN-CDC/G/DCDA catalyst demonstrated superior performance in reducing H_2O_2 to H_2O compared to FeN-CDC/G counterpart. The combined findings from the RRDE experiments and physico-chemical characterisation suggest that the incorporation of DCDA is advantageous for enhancing the number of M-N_x active sites in the materials and preventing metal aggregation, resulting in improved overall ORR performance, including E_{onset} and $E_{1/2}$. The higher ORR activity of the FeN-CDC/G/CDDA is also supported by the Tafel slope shown in Figure 5d. The FeN-CDC/G/DCDA catalyst displays Tafel slope of −52 mV dec^{-1} at low overpotentials, which is smaller than that of FeN-CDC/G (−66 mV dec^{-1}) and much smaller as compared to N-CDC/G/DCDA (−70 mV dec^{-1}).

7.3. Polymer-based carbon support for bifunctional oxygen electrocatalysts

This part of the thesis focus on the preparation of carbon supports from polymer frameworks for the ORR and OER [V, VI]. In first part CoPc doped on phloroglucinol polymer derived carbon was prepared and tested for RZAB [V] and in second part, bimetallic FeCo-doped atomically dispersed material was prepared for RZAB [VI].

7.3.1. Cobalt phthalocyanine-doped polymer-based materials

In search of more affordable carbon supports, polymer-derived carbon focused. Phloroglucinol-formaldehyde polymer framework was prepared and incorporated with CoPc. After pyrolysing the CoPc-doped phloroglucinol framework, the catalysts were tested for RZAB as electrode materials [V].

The crystalline structure of the catalyst materials was analysed using XRD (Figure 35a). In all XRD patterns, two broad peaks were observed at 26° and 43.5°, corresponding to the (002) and (100) graphitic planes, respectively [159]. No diffraction peaks indicative of metallic Co nanoparticles was detected, suggesting the absence of large Co particles in the prepared catalysts. PC-800 exhibited slightly more intense peaks than the Co-doped materials, suggesting that the introduction of transition metals may influence the graphitic structure [216].

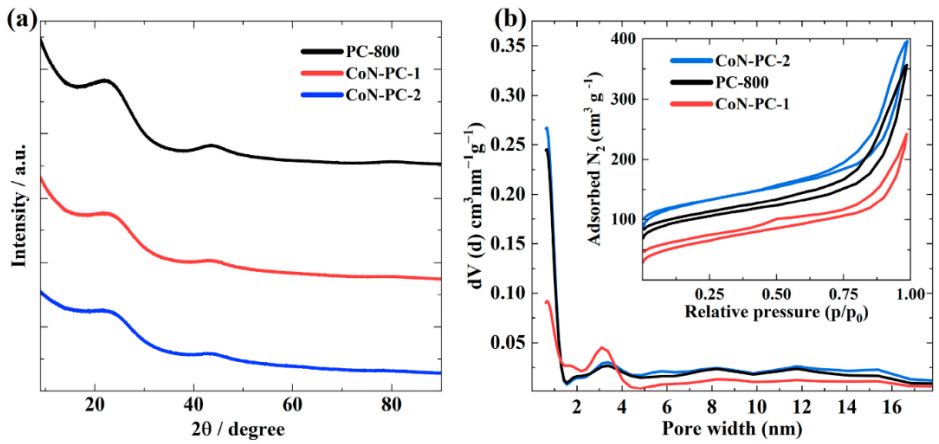

Figure 35. (a) XRD patterns and (b) pore size distribution and N_2 adsorption-desorption isotherms (inset) of the prepared catalysts.

Additionally, N_2 physisorption analysis was conducted to investigate the textural properties of the materials (Figure 35b and Table 13). The obtained isotherms displayed typical type-II adsorption-desorption behaviour with H3 hysteresis, indicating the presence of both micropores and mesopores in all the prepared catalysts [192]. The S_{BET} was determined to be 449 $m^2\ g^{-1}$ for PC-800, 464 $m^2\ g^{-1}$ for CoN-PC-1 and 325 $m^2\ g^{-1}$ for CoN-PC-2. PC-800 exhibited the highest total porosity and microporosity and these properties tended to decrease with the addition of CoPc. The balance between micro- and mesopores is crucial for carbon-based catalyst materials, as it facilitates the diffusion of reactant species during the ORR and OER processes [217]. Mesopores are generally considered more favourable for electrocatalysis, but an excessive increase in mesopores can lead to a reduction in the material's surface area, resulting in fewer active sites. Consequently, the prepared materials are considered suitable for ORR/OER due to their well-balanced micro/mesopore structure [218].

Table 13. Specific surface area (S_{BET}), total pore volume (V_{tot}) and micropore volume (V_{μ}) of catalysts.

Catalyst	S_{BET} ($m^2\ g^{-1}$)	V_{tot} ($cm^3\ g^{-1}$)	V_{μ} ($cm^3\ g^{-1}$)
PC-800	449	0.54	0.15
CoN-PC-1	464	0.43	0.16
CoN-PC-2	325	0.35	0.12

Subsequently, a detailed analysis of the materials was carried out using SEM to investigate their surface morphology. The SEM images are presented in Figure 36, showing that all the materials exhibit relatively uniform morphology characterised by interconnected porous carbon structures. The introduction of CoPc led to slight alterations in the surface morphology. Notably, the surface structure of the materials became somewhat more compact with increasing amounts of CoPc (as observed in the inset of Figure 36b,c). Furthermore, SEM-EDX-assisted elemental mapping was conducted to assess the distribution of dopants in the catalysts and to detect any agglomeration of cobalt (Figure 37). As anticipated, no agglomeration of elements was observed in the elemental mapping analysis, consistent with the XRD results. The bulk concentration of elements was quantified through SEM-EDX and the analysis revealed a high concentration of nitrogen and cobalt, indicating the successful incorporation of CoPc dopants (Table 14). Additionally, the presence of oxygen functionalities arising from carbon-oxygen species and metal oxides was detected and these functionalities are believed to be conducive to the OER [195].

Table 14. Elemental composition of the catalysts determined by SEM-EDX (wt.%).

Catalyst	C	N	O	Co
PC-800	84.4	10.3	5.3	-
CoN-PC-1	82.0	9.1	7.7	1.2
CoN-PC-2	79.9	10.3	7.7	2.2

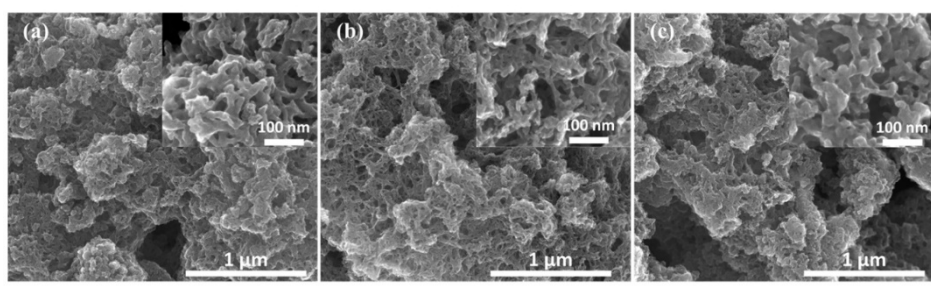

Figure 36. SEM images (inset: higher magnification images) of (a) PC-800, (b) CoN-PC-1 and (c) CoN-PC-2 materials.

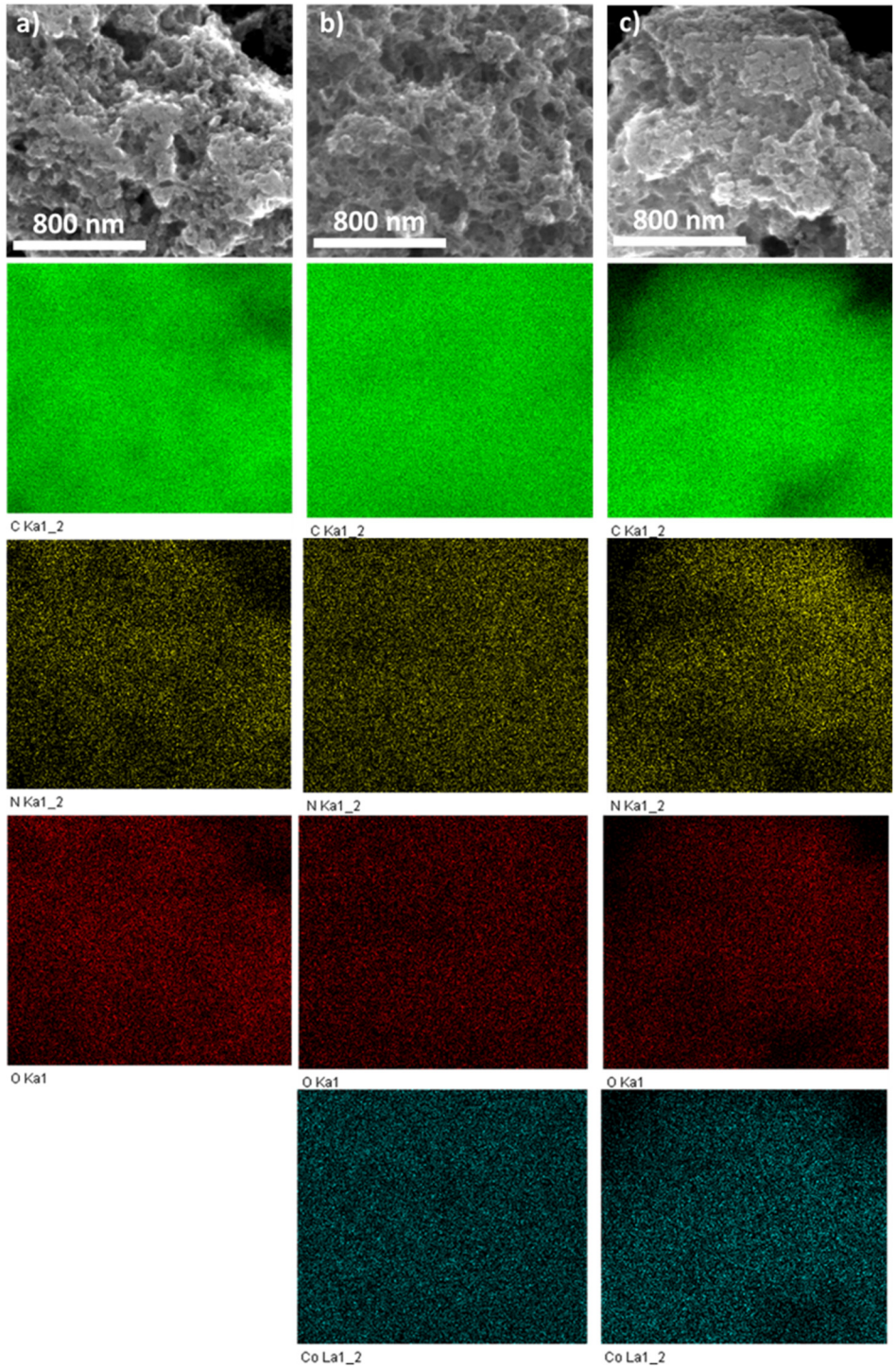

Figure 37. Elemental maps of C, N, O and Co obtained from SEM-EDX of (a) PC-800, (b) CoN-PC-1 and (c) CoN-PC-2 materials.

XPS measurements were performed to analyse the surface elemental composition and the different states of dopants present in the prepared catalysts (Figure 38). The XPS survey spectrum revealed the presence of carbon (C), nitrogen (N), oxygen (O) and cobalt (Co) on the surface of the catalysts. The nitrogen and oxygen contents were found to be similar in all the prepared catalysts, with the only variation being in the cobalt content, which was expected due to the different amounts of CoPc used during the catalyst preparation. Different nitrogen species, including pyridinic-N, pyrrolic-N, graphitic-N and M-N_x, were identified on the catalyst's surface through the deconvoluted high-resolution N 1s XPS peak (Figure 38 inset). Pyridinic-N and pyrrolic-N were the most prominent nitrogen species in all three materials, followed by graphitic-N and M-N_x (Figure 38d). These findings indicate that the doping with 2-methylimidazole and CoPc increased the concentration of different nitrogen species, promoting the kinetics of the ORR. Transition M-N_x centres are also known to contribute to high ORR activity through either 4-electron or 2×2-electron pathways [219]. Notably, the Co-N-PC-2 catalyst exhibited a relatively higher percentage of pyridinic-N and M-N_x compared to Co-N-PC-1, which could be advantageous for its higher electrocatalytic activity. The deconvolution of the O 1s peak from the XPS spectra revealed the presence of cobalt oxide, carboxyl, hydroxyl groups and chemisorbed water. These oxygen species are known to enhance the electrocatalytic activity of the material [220,221]. The increase in cobalt content resulted in a higher concentration of oxygen species, including metal oxide, carboxyl, hydroxyl groups and chemisorbed water. The formation of metal oxides during the pyrolysis of M-N_4 macrocycles has been reported and is known to enhance ORR/OER activity in alkaline media. Furthermore, individual components of the Co 2p XPS spectra were resolved to quantify the oxidation state of cobalt and determine the composition of each cobalt species. Figure 39 shows two prominent peaks at 780.4 and 796 eV, corresponding to Co $2p_{3/2}$ and Co $2p_{1/2}$, respectively. The deconvoluted peaks observed at 778 and 780.4 eV can be attributed to metallic cobalt and Co-N in the Co $2p_{3/2}$ spectrum, respectively. This further confirms the presence of Co-N_x centres. For CoN-PC-1, the concentration of Co-N (0.11 at%) is lower than that in CoN-PC-2 (0.23 at%).

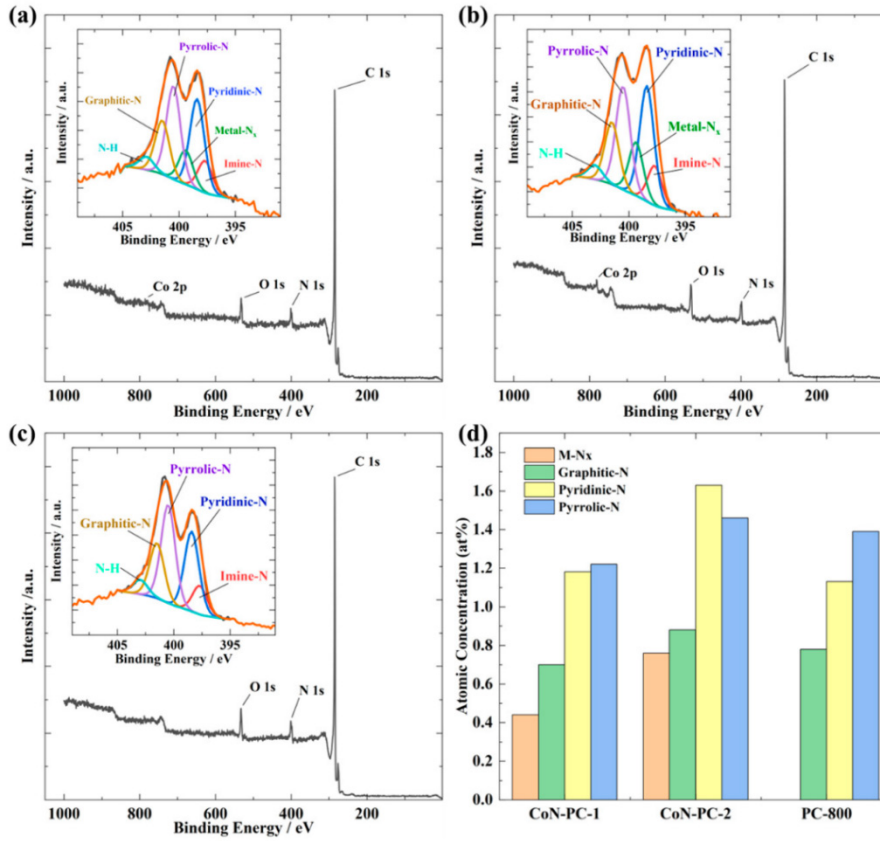

Figure 38. XPS survey spectra and N 1s high-resolution spectra (inset) of (a) CoN-PC-1, (b) CoN-PC-2 and (c) PC-800 materials and (d) graphical representation of nitrogen species surface concentration in the prepared electrocatalysts.

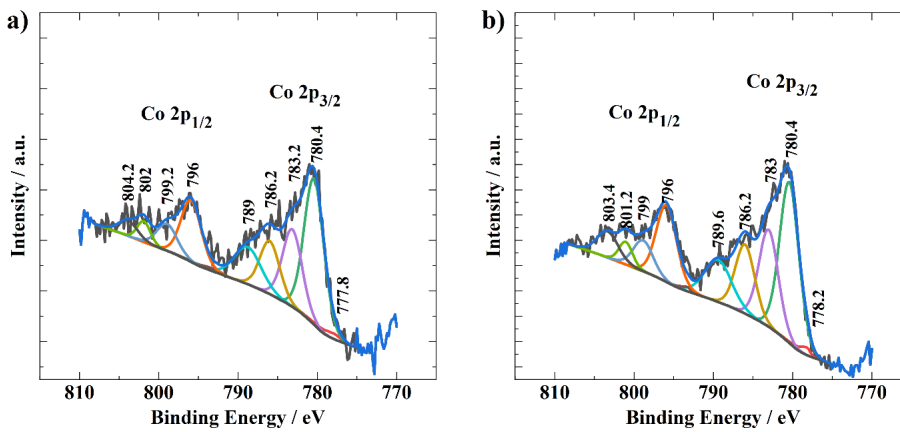

Figure 39. Deconvoluted Co 2p XPS spectra for (a) CoN-PC-1 and (b) CoN-PC-2 catalysts.

Furthermore, the influence of CoPc on the ORR and OER activity was investigated using the RDE method. As expected, PC-800 exhibited the lowest electrocatalytic activity for the ORR, with an E_{onset} of 0.79 V. Additionally, PC-800 followed two reduction pathways during the ORR process. A significant enhancement in the electrocatalytic activity was observed upon the addition of CoPc. Both CoN-PC-1 and CoN-PC-2 electrocatalysts showed nearly identical overall ORR electrocatalytic activity in the RDE experiment, with E_{onset} and $E_{1/2}$ values of 0.88 and 0.81 V, respectively. Commercial Pt/C ($E_{1/2}$ = 0.85 V) was also assessed using the RDE method and the results are presented in Figure 40 and Table 15.

Table 15. Electrochemical results for prepared catalysts in 0.1 M KOH solution.

Catalysts	E_{onset} **(V)**	$E_{1/2}$ **(V)**	$E_{j=10}$ **(V)**
PC-800	0.79	-	-
CoN-PC-1	0.88	0.81	1.73
CoN-PC-2	0.88	0.81	1.70

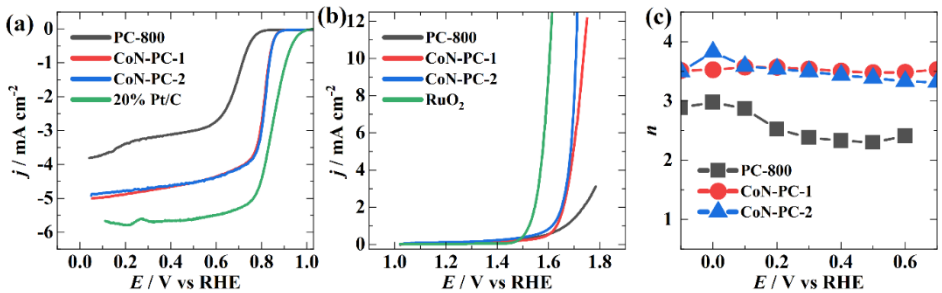

Figure 40. (a) ORR and (b) OER polarisation curves in 0.1 M KOH solution at 1900 rpm and 10 mV s^{-1}. (c) number of transferred electrons per O_2 molecule derived from the K-L plots.

Regarding the OER process, the performance was evaluated in terms of $E_{j=10}$. Among the as-prepared catalysts, CoN-PC-2 demonstrated the most favourable OER activity, with an $E_{j=10}$ value of 1.70 V. CoN-PC-1 showed a slightly higher $E_{j=10}$ value of 1.73 V, while PC-800 did not exhibit comparable activity. This trend was expected, as PC-800 lacks transition metal-containing active sites for OER and an increased OER activity was observed in catalysts with higher metal contents, providing more active sites for OER. The linearity of the K-L plots implies first-order kinetics for ORR (Figure 41) and the electron transfer number (n value) was determined to be close to four (approximately 3.5) for CoN-PC (Figure 40c).

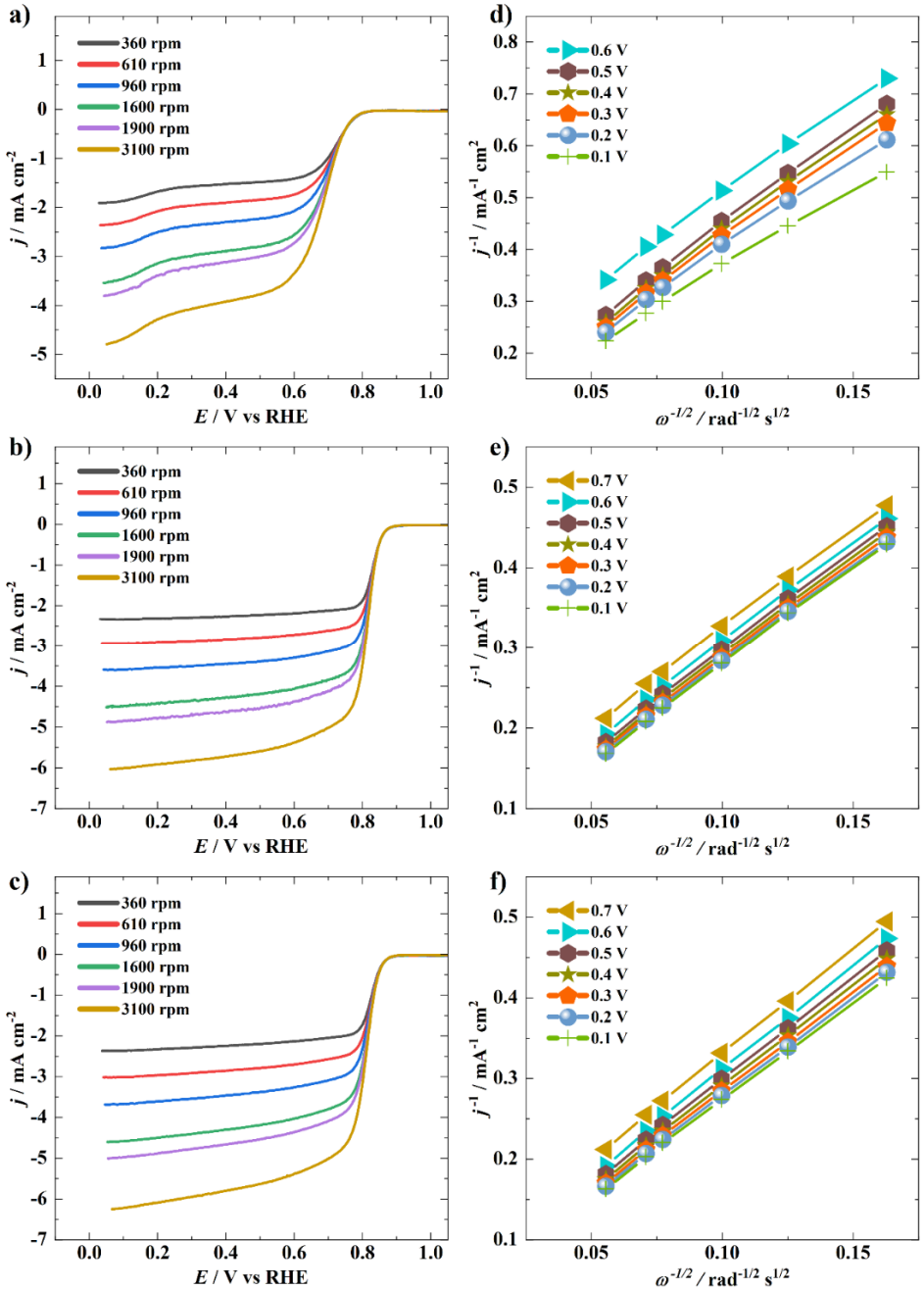

Figure 41. ORR polarisation curves at different rotation rates for (a) PC-800, (b) CoN-PC-1 and (c) CoN-PC-2 in O_2-saturated 0.1 M KOH solution. Koutecky-Levich plots for (d) PC-800, (e) CoN-PC-1 and (f) CoN-PC-2 derived from the respective polarisation curves.

A cyanide poisoning test was also conducted to confirm the presence of the M-N_x active sites in the catalyst materials. In principle, cyanide ions strongly bind to the M-N_x sites, impairing the catalysts' ORR activity [34]. LSV curves were obtained in a 0.1 M KOH solution containing 10 mM NaCN. It is evident from Figure 42 that the ORR activity of the catalysts significantly decreased with the addition of cyanide ions. These test results further confirm the existence of M-N_x centres in the catalysts, as identified in the XPS analysis.

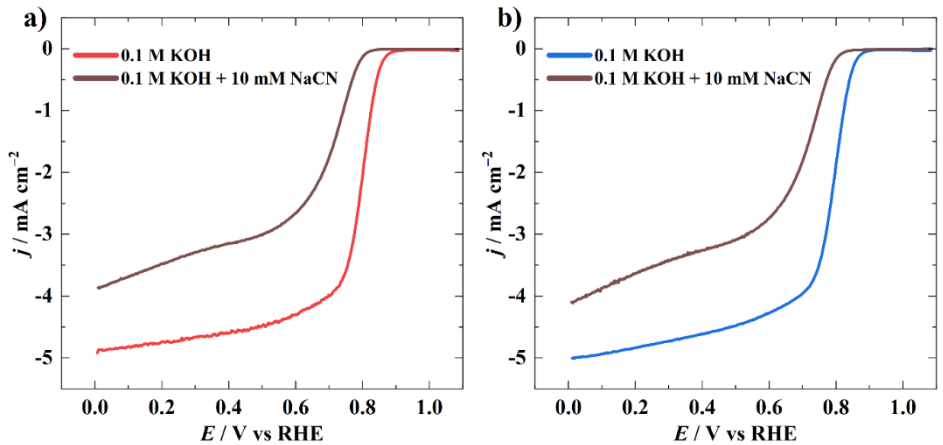

Figure 42. ORR polarisation curves for (a) CoN-PC-1 and (b) CoN-PC-2 catalysts in O_2-saturated 0.1 M KOH solution containing 10 mM NaCN at 1900 rpm (v= 10 mV s^{-1}).

To assess the electrochemical stability of the synthesised catalysts, 10,000 repeated potential cycles were conducted in an O_2-saturated 0.1 M KOH solution, as shown in Figure 43a,b. CoN-PC-1 exhibited good stability, with only a 14 mV shift in $E_{1/2}$. In contrast, there was no observable difference in $E_{1/2}$ for CoN-PC-2. This remarkable stability can be attributed to the hierarchical porous structures within the CoN-PC catalysts, which help mitigate the dissolution and aggregation of metal during the rigorous electrocatalytic process. This structural feature stabilises the M-N_x active sites and accelerates the electron transfer process, collectively promoting excellent electrochemical stability. To assess the stability of the OER, chronoamperometric measurements were conducted at a potential of 1.7 V in an Ar-saturated 0.1 M KOH solution (Figure 43c). After 3 h, CoN-PC-2 retained 79% of the initial OER current, while CoN-PC-1 maintained 51%. The higher stability of CoN-PC-2 was attributed to its higher Co content, which helps stabilise the carbon matrix and mitigate the loss of active sites.

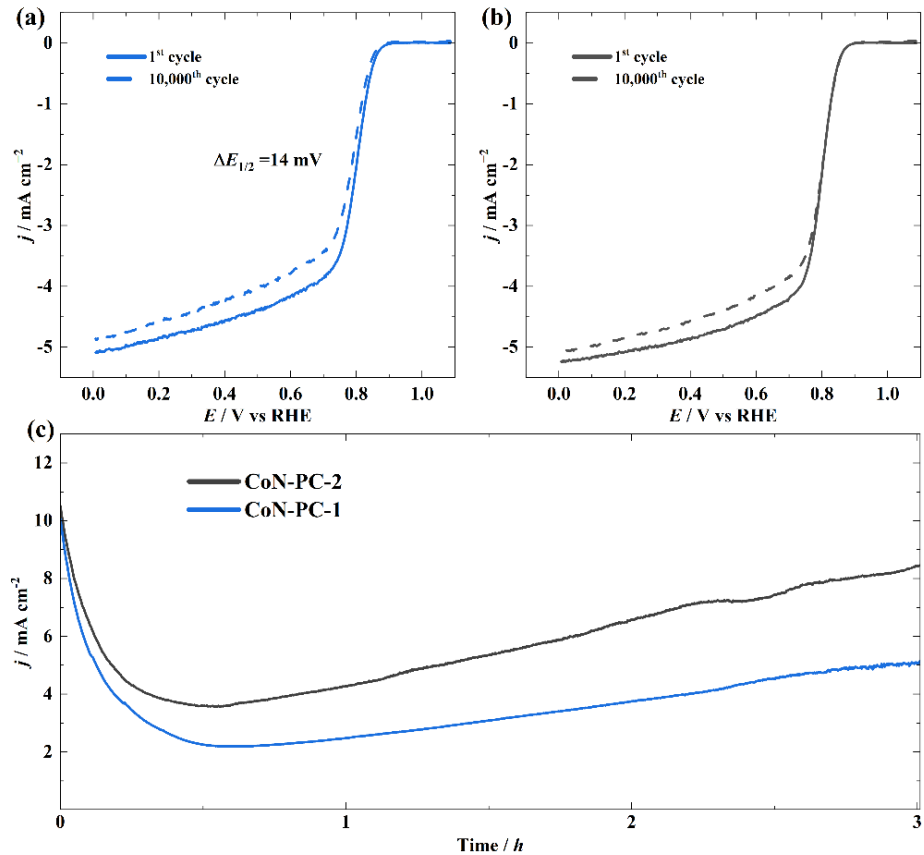

Figure 43. Polarisation curves of ORR before and after stability test for (**a**) CoN-PC-1 and (**b**) CoN-PC-2 catalysts in O_2-saturated 0.1 M KOH solution at 1900 rpm with a scan rate of 10 mV s^{-1}. (c) OER stability test for CoN-PC-1 and CoN-PC-2 at 1.7 V for 3 h (ω = 1900 rpm).

The performance of the developed CoN-PC-1 and CoN-PC-2 catalyst materials in terms of oxygen bifunctional electrocatalysis at the cathode was assessed by assembling and testing RZABs. The discharge polarisation curves and power density curves for the catalysts are presented in Figure 44a. Impressively, both CoN-PC-1 and CoN-PC-2 catalysts exhibited OCV values as high as 1.45 and 1.47 V, respectively. As shown in Figure 44a, CoN-PC-2 achieved a higher P_{max} of 158 mW cm^{-2}, slightly surpassing CoN-PC-1 (155 mW cm^{-2}). Additionally, a galvanostatic charge-discharge cycling test (10 min per cycle) was conducted at a current density of 5 mA cm^{-2} to evaluate the durability of both catalysts (Figure 44b). Under the same conditions, the CoN-PC-2 catalyst demonstrated excellent cycling performance compared to CoN-PC-1. Interestingly, both CoN-PC-1 and CoN-PC-2 catalysts initially had a voltage gap of approximately 0.9 V between their charge and discharge potentials. However, after 45 h of cycling,

the voltage gap of CoN-PC-2 increased to 1.08 V, while RZABs based on CoN-PC-1 failed twice within 30 h. The higher stability of CoN-PC-2 can be attributed to its higher metal content, which can provide sustainable active sites for both ORR and OER and it also experiences lower carbon decomposition in highly alkaline media. Nonetheless, comparing different RZABs can be challenging due to various factors such as electrode distance, air flow, Zn anode, electrolyte volume, etc.

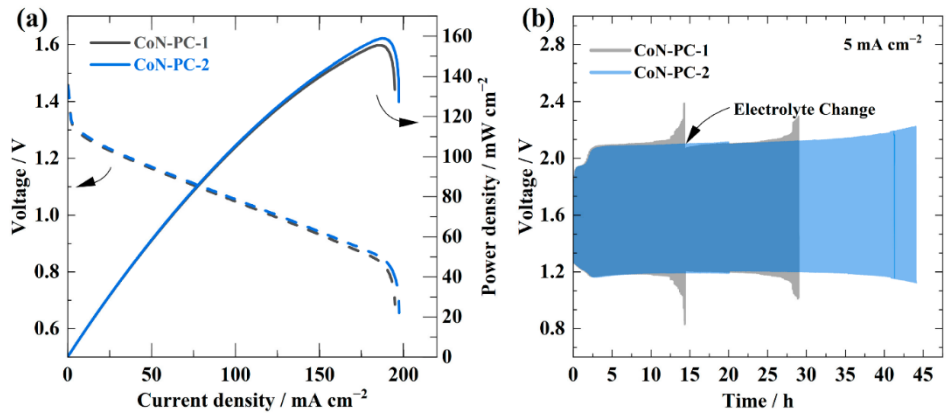

Figure 44. (a) Polarisation and power density curves of CoN-PC-1 and CoN-PC-2 catalysts for discharging. (b) Stability test for RZABs using CoN-PC-1 and CoN-PC-2 catalysts by galvanostatic discharge-change cycling at 5 mA cm^{-2}.

7.3.2. Zinc-assisted synthesis of polymer framework-based bimetal catalysts

This part of the thesis aims to provide an efficient way to synthesise atomically dispersed bimetallic catalyst for oxygen electrocatalysis from transition metal embedded polymer framework. Herein, iron and cobalt-doped carbon-based catalyst derived from phloroglucinol-dicyandiamide-formaldehyde framework (PDF) is prepared utilising zinc nitrate as template. Prepared Fe- and Co-doped carbon catalyst (FeCoN-PDF-T_2-2) exhibits excellent bifunctional catalytic activity and tested in RZAB.

Nitrogen physisorption analysis was performed to investigate the textural characteristics of the prepared materials and to assess the influence of metal doping and the zinc template, as detailed in Figure 45a and Table 16. The PDF material without the template was found to have a very low S_{BET}. Treating the PDF materials with zinc nitrate (PDF-T_2) led to a simultaneous increase in both the S_{BET} (421 m^2 g^{-1}) and pore size (~3.5 nm), indicating that the zinc template helps achieve a high surface area in PDF materials. A similar trend was observed for metal-incorporated PDF (MN-PDF-T_2-2, where M = Fe, Co). The shape of the N_2 physisorption isotherms of template-treated materials conforms to the IUPAC classification, resembling a type IV isotherm with H2 hysteresis

[192]. This pattern indicates a combination of micro-mesoporous materials. In a comparative analysis of the four materials employed, namely PDF-T_2 (421 m^2 g^{-1}), FeN-PDF-T_2-2 (291 m^2 g^{-1}), CoN-PDF-T_2-2 (408 m^2 g^{-1}) and FeCoN-PDF-T_2-2 (414 m^2 g^{-1}), the FeN-PDF-T_2-2 material exhibits a relatively lower S_{BET}, possibly due to the formation of carbon nanotubes during the pyrolysis process of Fe-incorporated PDF (further discussed in SEM and STEM sections). Apart from smaller mesopores of 2–10 nm, larger mesopores ranging from 10 to 25 nm are also evident (Figure 45a). It is worth noting that various transition metals have different effects on the textural properties of PDF materials owing to their specific interaction with the polymer network during the synthesis procedure. The material prepared with cobalt tends to exhibit a higher micropore content, as listed in Table 16, while the incorporation of iron favours the development of mesopores. Consequently, zinc-templated metal-doped carbon materials with a similar porous structure was prepared, combining meso- and micropores, featuring smaller (~3.5 nm) and larger (around 10-25 nm) mesopores.

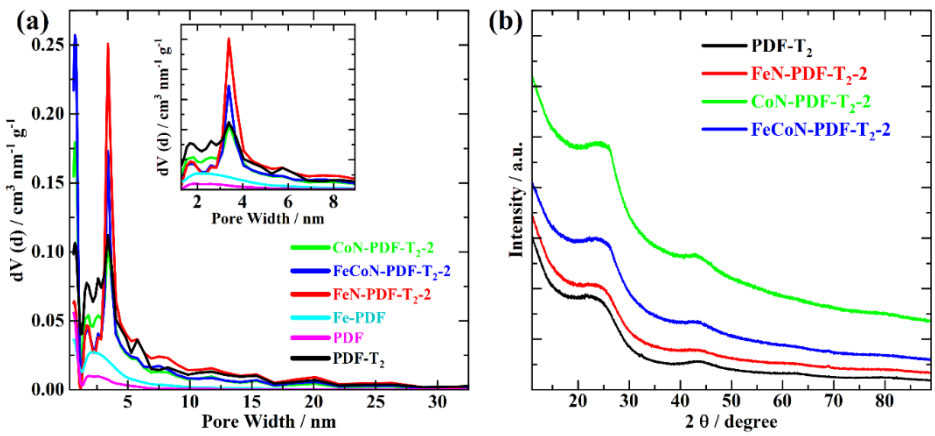

Figure 45. (a) Pore-size distribution and (b) XRD patterns of the prepared materials.

Table 16. Textural properties of PDF materials. Specific surface area (S_{BET}), microporous SSA and pore volume (S_{micro}, V_{micro}), mesoporous *SSA* and pore volume (S_{meso}, V_{meso}) and total pore volume (V_{tot}).

Catalyst	S_{BET} (m^2 g^{-1})	S_{dft} (m^2 g^{-1})	S_{micro} (m^2 g^{-1})	S_{meso} (m^2 g^{-1})	V_{micro} (cm^3 g^{-1})	V_{tot} (cm^3 g^{-1})
PDF	71	98	83	15	0.03	0.06
Fe-PDF	104	118	76	42	0.04	0.13
PDF-T_2	421	387	226	161	0.11	0.52
CoN-PDF-T_2-2	408	406	284	122	0.12	0.42
FeN-PDF-T_2-2	291	297	115	182	0.06	0.47
FeCoN-PDF-T_2-2	414	478	351	127	0.14	0.44

The catalyst materials were subjected to XRD analysis to investigate their crystallographic structure (see Fig. 45b). The XRD analysis reveals that all samples consist of carbon with unbounded layers, which might be beneficial for enhancing mass transfer in electrochemical processes. The most characteristic peaks were observed at around 25° and 43°, corresponding to the (002) and (100) graphitic carbon planes [159]. Importantly, no diffraction peaks were identified that could be attributed to transition metals, signifying the absence of sizable metal nanoparticles in the prepared catalysts.

The defect densities of the as-synthesised catalysts were analysed using Raman spectroscopy. The comparative first-order Raman spectra of the samples are shown in Figure 46a. All spectra were fitted using a five-band model, where G band (~1590 cm^{-1}) corresponds to the stretching vibrations of the sp^2 carbon atoms in the ideal graphitic lattice and various D bands (D1, D2, D3 and D4) correspond to different types of structural defects. The I_D/I_G ratio (peak intensity ratio) is a commonly used parameter to quantify the structural imperfection in graphene materials. However, for highly disordered carbon materials, the Raman band typically labelled as G is a superposition of the G and D2 bands, making it challenging to separate them. To evaluate the degree of structural disorder in the catalyst materials, several parameters were considered, including the full widths at half-maximum (FWHM) of the D1 and G bands, I_{D1}/I_G (the ratio of the areas under the bands) and R2, which is a ratio related to the areas of the indicated bands. The R2 parameter is a reliable measure of defect densities in disordered carbon materials. A value of $R2 > 0.5$ indicates highly disordered carbon, while $R2 < 0.5$ suggests highly graphitised carbons. The analysis showed that the structural disorder factor (R2 value) of the carbon materials increased progressively in the sequence of PDF-T_2 (0.62), CoN-PDF-T_2-2 (0.71), FeCoN-PDF-T_2-2 (0.76) and FeN-PDF-T_2-2 (0.84) materials. These highly abundant defect sites can provide an increased number of electrocatalytically active sites, which is beneficial for enhancing electron transfer rates.

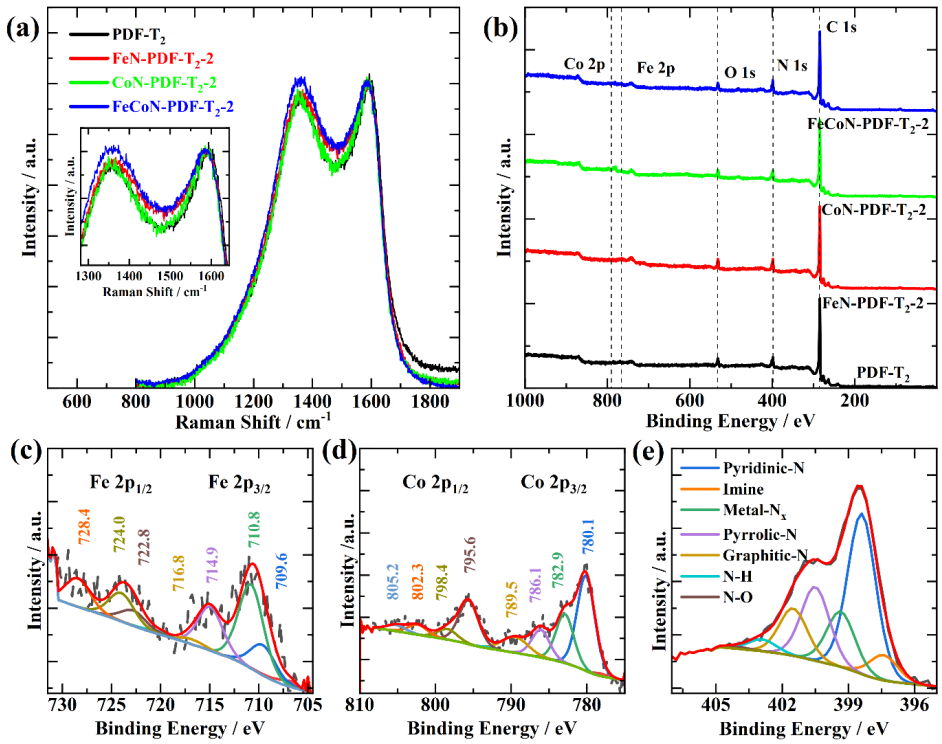

Figure 46. (a) Raman spectra of the catalysts. (b) XPS survey spectra of the prepared catalysts. Deconvoluted detailed XPS spectra of (c) Fe 2p, (d) Co 2p and (e) N 1s, peak corresponding binding energy values of the species present in FeCoN-PDF-T_2-2.

XPS was utilised to investigate the chemical states, surface composition and bonding configurations of elements in the materials. The XPS survey spectra of the materials revealed the presence of carbon (C), nitrogen (N), oxygen (O) and the transition metal elements iron (Fe) and cobalt (Co) in the respective materials (Figure 46b). Detailed XPS analysis of the Fe 2p spectrum for FeCoN-PDF-T_2-2 and FeN-PDF-T_2-2 catalysts showed two prominent peaks at 710.8 and 724 eV, corresponding to the Fe $2p_{3/2}$ and Fe $2p_{1/2}$ spin-orbit splitting levels. Deconvolution of the Fe $2p_{3/2}$ peak into peaks at 709.6 and 710.8 eV revealed the presence of Fe^{2+} and Fe^{3+} states, indicating that the valence of iron in the catalyst materials lies between +2 and +3 (Figure 46c). Similarly, two peaks at around 780.1 and 795.6 eV in the Co 2p spectrum (Figure 46d) correspond to the Co $2p_{3/2}$ and Co $2p_{1/2}$ levels. These peaks indicate the presence of cobalt mainly as Co^{2+} and Co^{3+}. The presence of high-intensity satellite peaks at 782.9 and 798.4 eV suggests the predominance of Co^{3+} states, while a smaller pre-peak at 778.2 eV indicates the presence of some metallic Co^0 states. Additionally, the peaks at 786.1, 789.5, 802.3 and 805.2 eV can be attributed to satellite peaks of cobalt [222].

Deconvoluted high-resolution N 1s XPS spectra revealed the presence of various N-species in the prepared materials, including pyridinic-N, M-N_x, pyrrolic-N and graphitic-N (Figure 46e). Among these nitrogen species, pyridinic-N was the dominant one in all the prepared materials, followed by pyrrolic-N, M-N_x and graphitic-N. It is important to note that these nitrogen species play a crucial role in enhancing the ORR kinetics, with a particular emphasis on pyridinic-N and M-N_x [67,105]. Interestingly, the PDF catalysts containing cobalt exhibited a higher content of metal-coordinated nitrogen sites compared to their iron counterparts. For instance, FeN-PDF-T_2-2 contained 13.4% M-N_x sites, whereas FeCoN-PDF-T_2-2 had 14.7% and CoN-PDF-T_2-2 had the highest proportion at 19.0%. These M-N_x sites are known to facilitate the adsorption and activation of O_2 molecules, thereby accelerating the reaction kinetics of ORR [67]. Furthermore, pyrrolic-N and graphitic-N were also identified in the materials. These nitrogen species can contribute to enhancing the ORR in alkaline media by improving reaction kinetics (pyrrolic-N) and limiting current density (graphitic-N) [73,74].

A detailed examination of the surface morphology of the materials was conducted using SEM. Figure 47 illustrates the distinct structures observed for the developed materials. The PDF materials exhibit a foamy porous structure with high roughness (as seen in Figure 47a,c,e,g). The presence of this porous morphology is attributed to the use of zinc nitrate as a template, which can generate nitrogen oxides during the heat treatment process, leading to the formation of this specific structural configuration. The morphology of PDF-T_2 (Figure 47a,b) appears denser in comparison to the metal-doped the PDF materials. The introduction of transition metals during the synthesis process of PDF materials initiated the partial formation of CNTs during the heat treatment stage (Figures 47d,h). The occurrence of CNT formation in these materials seems to exhibit a trend. Specifically, the iron-doped PDF (Figure 47d) material has a higher quantity of CNT and more flattened sheet-like structures compared to the Co- or FeCo-PDF materials. Such open structures are expected to enhance the mass-transfer properties of the materials. In addition, SEM-EDX analysis was performed to determine the bulk elemental composition of the materials and the data are presented in Table 17. The nitrogen and oxygen content were found to be approximately 12 and 10 wt.%, respectively, for all catalyst materials. Furthermore, the total metal content assessed by EDX analysis was nearly 2.5 wt.%.

Table 17. Elemental composition of as-prepared PDF materials by SEM-EDX (wt.%).

Catalyst	C	N	O	Fe	Co
PDF-T_2	73.6	12.1	9.0	-	-
FeN-PDF-T_2-2	72.5	11.6	9.2	2.7	0.0
CoN-PDF-T_2-2	71.1	12.6	10.4	0.0	2.9
FeCo N-PDF-T_2-2	72.0	12.3	10.7	0.7	0.9

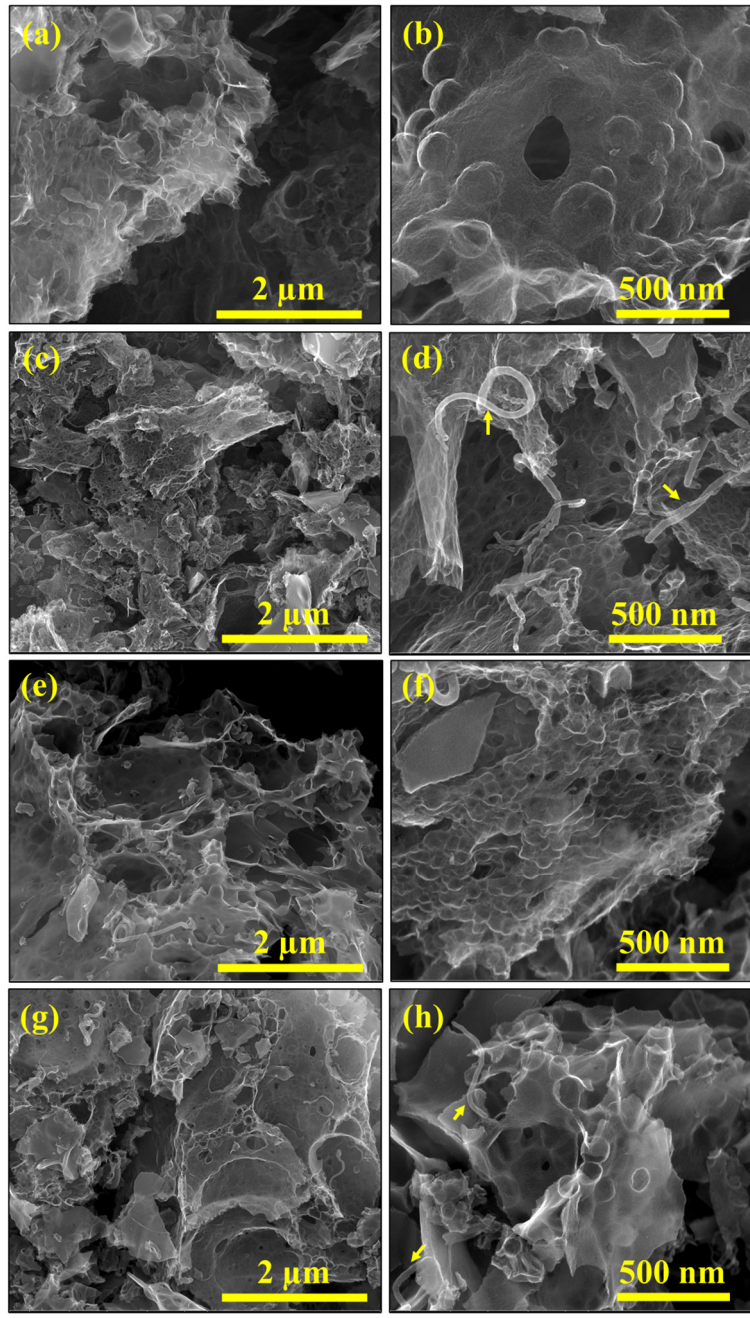

Figure 47. SEM images of (a, b) PDF-T_2, (c, d) FeN-PDF-T_2-2, (e, f) CoN-PDF-T_2-2 and (g, h) FeCoN-PDF-T_2-2 materials. (Arrows point out some of the CNTs in materials.)

The STEM was used to gain insights into the structure of the prepared FeCo-PDF-T_2-2 catalyst (Figure 48). The STEM images reveal a foamy carbon structure and no visible metal aggregates are observed (Figure 48a). Figure 48b shows the formation of long graphitic carbon layers within the catalyst material. This structure is advantageous for enhancing electrical conductivity and corrosion resistance. Furthermore, the high-magnification HAADF-STEM image (Figure 48c) reveals the presence of bright spots highlighted in yellow circles. These bright spots indicate the formation of highly abundant atomically dispersed metal sites within the catalyst. The elemental mappings confirm a uniform distribution of the doping elements (Fe, Co and N), providing further evidence of well-dispersed iron, cobalt and nitrogen species (Figure 48d). These findings are consistent with the XRD results, which did not show any peaks indicative of metal aggregates.

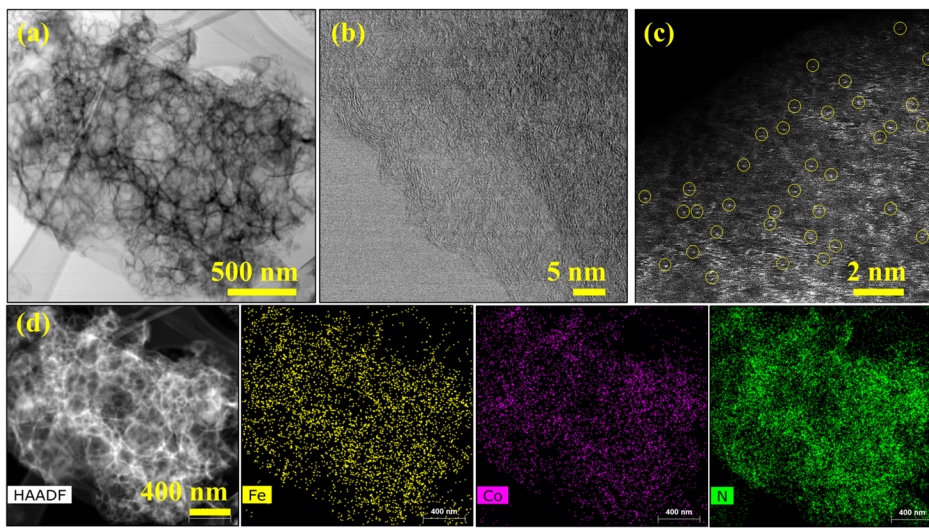

Figure 48. (a, b) Bright field, (c) high-angle annular dark field (HAADF) images of FeCo-PDF-T_2-2 (yellow circle highlighting some of the atomic metal) and (d) low magnification HAADF-STEM image and corresponding EDX maps of Fe, Co and N of the FeCoN-PDF-T_2-2 materials.

The optimisation of the catalyst's preparation involved adjusting the metal and template content. To optimise the metal content, Fe-doped PDF material was used and several catalyst materials were prepared with varying mass ratios of Fe, while keeping the ratio of PDF to zinc nitrate at 1:2. These catalyst materials are labelled as FeN-PDF-T_2-x, where x = 1, 2, 3. Figure 49a shows the ORR polarisation curves for these materials, with FeN-PDF-T_2-2 exhibiting the highest $E_{1/2}$ of 0.86 V, indicating optimal metal content. Subsequently, the zinc nitrate ratio was also optimised and the results are presented in Figure 49b. The

use of zinc nitrate as a template significantly improved the ORR activity and the optimal template ratio was found to be 1:2.

Based on these results, bimetal-doped PDF materials were prepared using iron and cobalt as the metal centres, aiming to create a bifunctional catalyst for oxygen electrocatalysis. As shown in Figure 49c, CoN-PDF-T_2-2 had a lower $E_{1/2}$ value of 0.82 V, while FeCoN-PDF-T_2-2 displayed a similar $E_{1/2}$ value of 0.85 V compared to FeN-PDF-T_2-2. The excellent ORR activity can be attributed to the presence of single atomic sites in the catalysts and the textural properties of the catalysts. However, a slight difference in limiting current density was observed upon introducing cobalt, which could be due to textural and morphological variations in the catalysts (as discussed in the BET and SEM results). For comparison, the commercial 20% Pt/C catalyst was also tested for ORR, showing slightly superior values (E_{onset} = 1.01 V, $E_{1/2}$ = 0.88 V).

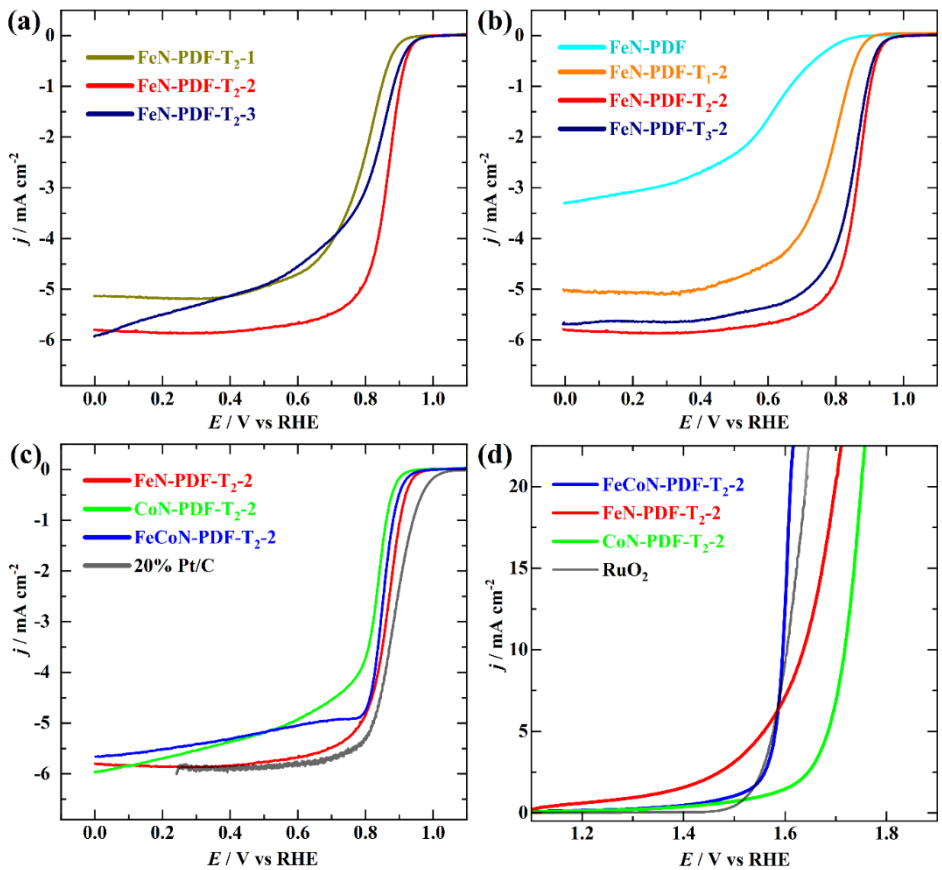

Figure 49. ORR polarisation curves recorded at 1600 rpm in O_2-saturated 0.1 M KOH (v = 10 mV s^{-1}) for (a) FeN-PDF-T_2 catalysts at different metal content, (b) FeN-PDF at different template ratios, (c) bimetallic Fe and Co-doped PDF and (d) OER polarisation curves recorded in Ar-saturated 1 M KOH at 1600 rpm and scan rate of 10 mV s^{-1}.

The catalyst materials were also tested for the OER, as shown in Figure 49d. The FeCoN-PDF-T_2-2 catalyst was found to be the most active for OER, with an $E_{j=10}$ value of only 1.60 V, which is similar to that of RuO_2 and lower than that of FeN-PDF-T_2-2 ($E_{j=10}$ = 1.64 V) and CoN-PDF-T_2-2 ($E_{j=10}$ = 1.70 V). The higher OER activity of FeCoN-PDF-T_2-2 can be attributed to the synergistic effect of iron and cobalt. The difference between $E_{1/2}$ and $E_{j=10}$, defined as ΔE, was calculated to evaluate the overall activity of catalysts in oxygen-involved reactions. The FeCoN-PDF-T_2-2 material exhibited a ΔE value of 0.75 V, while FeN-PDF-T_2-2 and CoN-PDF-T_2-2 catalysts had ΔE values of 0.78 and 0.88 V, respectively. A smaller ΔE indicates superior performance of catalyst materials as a bifunctional electrocatalyst. The improved bifunctional performance can be attributed to the increased surface area, the presence of defect sites and the synergistic effect resulting from the incorporation of both iron and cobalt single-metal atom sites.

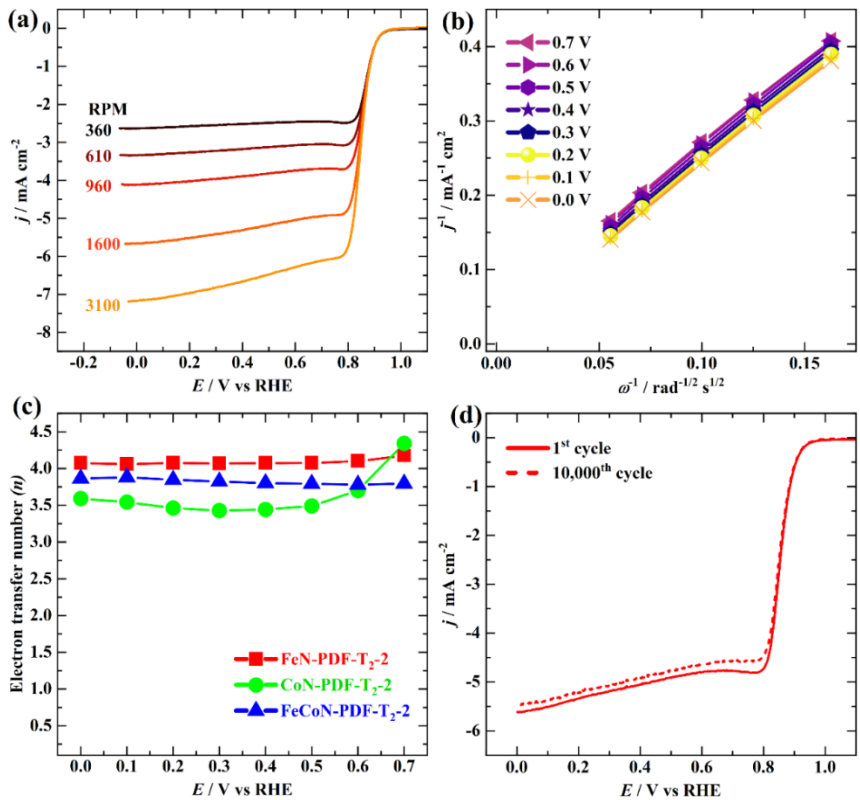

Figure 50. (a) ORR polarisation curves at different rotation rates in O_2-saturated 0.1 M KOH for FeCoN-PDF-T_2-2, (b) Koutecky-Levich plots for ORR derived from RDE polarisation data for FeCoN-PDF-T_2-2, (c) electron transfer number as a function of potential for the prepared catalysts and (d) ORR polarisation curves of FeCoN-PDF-T_2-2 before and after stability test.

To investigate the ORR pathway, a series of RDE polarisation curves were measured at various rotation rates (Figure 50a). These RDE data were used to construct the K-L plots, which are used to calculate the *n* involved in the ORR process (Figure 50b). The linearity observed in the K-L plots indicates first-order kinetics towards O_2 concentration in the electrolytes. The *n* for all the catalysts is close to four, suggesting that the ORR proceeds via a 4-electron pathway (Figure 50c). It appears that the cobalt content slightly reduces the selectivity for ORR, as the *n* for CoN-PDF-T_2-2 is 3.5 and the *n* value increased when iron was incorporated (*n* = 3.8 for FeCoN-PDF-T_2-2).

The stability of the electrocatalysts is a crucial criterion for assessing the ORR performance. After 10,000 potential cycles between 0.6 and 1.0 V, FeCoN-PDF-T_2-2 exhibited negligible change in the $E_{1/2}$ value, indicating the outstanding electrochemical stability of the catalyst (Figure 50d). A minor decrement in the limiting current density was observed, which may be attributed to the loss of some active sites from the catalyst over prolonged cycling.

The FeCoN-PDF-T_2-2 catalyst demonstrated remarkable performance when used as the cathode material in RZAB. The RZAB showed a notably high OCV reaching up to 1.53 V, along with an impressive P_{max} of 258 mW cm^{-2} (Figure 51a). This performance surpasses that of a commercial PtRu/C catalyst (OCV = 1.46 V, P_{max} = 185 mW cm^{-2}). To evaluate the cycling performance, galvanostatic discharge-charge cycles were conducted over 25 h, equivalent to 275 cycles (Figure 51b). Remarkably, the FeCoN-PDF-T_2-2-based RZAB demonstrated stable cycling performance for both discharge and charge processes. In contrast, the PtRu/C-based RZAB failed within 17 h, highlighting the superior stability of FeCoN-PDF-T_2-2 in practical RZABs. Furthermore, there was only a slight change in voltage efficiency during the discharge and charge processes over 25 h. The initial voltage gap for charging and discharging potential for FeCoN-PDF-T_2-2 was 0.87 V, whereas it was 1.39 V for PtRu/C (Figure 51c). After 25 h, a slight increase in the voltage gap was observed (0.2 V), possibly due to carbon corrosion of the catalyst or carbon paper used as a gas diffusion layer. Overall, the FeCoN-PDF-T_2-2 catalyst exhibits exceptional electrocatalytic performance for both the ORR and the OER, enabling the assembly of a highly efficient RZAB with outstanding OCV and P_{max}. This surpasses the performance of a commercial PtRu/C catalyst in both P_{max} and stability, making it a promising candidate for practical RZAB applications.

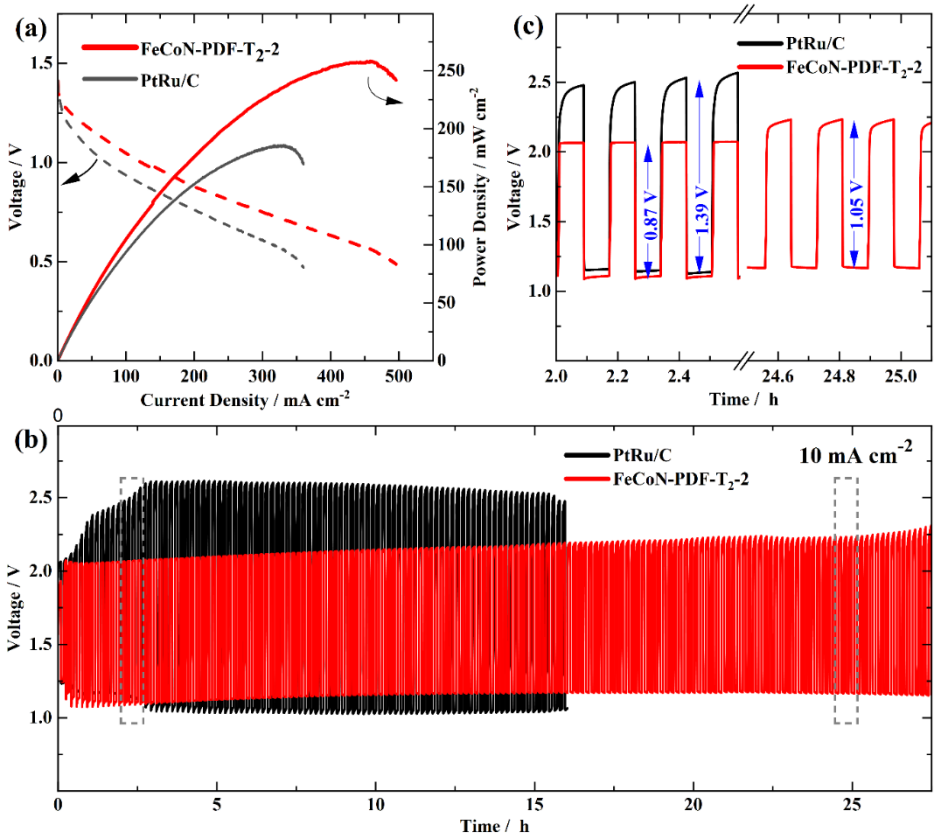

Figure 51. (a) Discharge polarisation curves and corresponding power density curves for RZABs based on FeCoN-PDF-T_2-2 and PtRu/C catalysts, (b, c) Galvanostatic discharge-charge curves for assembled RZABs.

8. SUMMARY

The aim of this doctoral thesis revolved around the development of transition metal-based non-precious metal catalysts for the bifunctional electrocatalysis of oxygen reduction reaction (ORR) and oxygen evolution reaction (OER). Furthermore, the research aimed to assess the suitability and performance of these catalysts in anion exchange membrane fuel cells (AEMFCs) and rechargeable zinc-air batteries (RZABs). To achieve this goal, the catalyst materials doped with transition metals and nitrogen were synthesised using a high-temperature pyrolysis process, employing various transition metal phthalocyanines and diverse nanocarbon supports. Subsequently, the catalysts exhibiting superior performance were integrated into the cathode of single-cell AEMFCs or RZABs and characterised by various physico-chemical methods.

In the first part of the thesis, one-step pyrolysis method was utilised for the synthesis of mixed transition metal-nitrogen-carbon (M-N-C)-type catalysts. In this process, various metal phthalocyanine combinations (e.g., FeNi, FeMn, FeCo, NiCo, MnCo and MnNi) were doped on multiwalled carbon nanotubes (MWCNT) to investigate their performance for the ORR and OER in an alkaline electrolyte [I,II]. The presence of catalytic M-N_x centres, which was verified in all catalyst materials by X-ray photoelectron spectroscopy (XPS), can significantly enhance both the ORR and OER kinetics. Among the prepared catalysts, FeCoN-MWCNT exhibited the highest activity for the ORR, while FeNiN-MWCNT excelled in the OER [II]. However, when considering bifunctional properties and the lowest ΔE value, FeCoN-MWCNT, FeNiN-MWCNT and NiCoN-CNT catalysts demonstrated superior performance with comparable ΔE values [I,II]. In electrochemical device tests, the FeCoN-MWCNT catalyst achieved an impressive peak power density (P_{max}) of 692 mW cm^{-2} in AEMFC [II], FeNiN-MWCNT showed comparable performance to the state-of-the-art RuO_2 in an anion exchange membrane electrolyser (AEMEL) [II] and NiCoN-CNT showed good performance in solid-state rechargeable zinc-air battery [I].

In the second part of the thesis, combination of iron phthalocyanine (FePc) and nickel phthalocyanine (NiPc) were again selected to synthesise bimetallic nitrogen-doped nanocarbon catalysts using six different carbon nanomaterials to study the carbon support effect on the ORR and OER performance [III]. These catalyst materials displayed remarkable electrocatalytic activity for both the ORR and OER. Detailed physico-chemical characterisation of the catalysts confirmed the presence of metal nanoparticles, metal-nitrogen centres and metal oxides, which are considered active sites for ORR or OER in alkaline environment. Among these catalysts, highly graphitised FeNiN−MWCNT and highly mesoporous FeNiN−MC catalysts demonstrated the best electrocatalytic activity for ORR, achieving P_{max} of 406 mW cm^{-2} and 386 mW cm^{-2} in AEMFCs, respectively [III]. Additionally, FeNiN−MWCNT exhibited a P_{max} of 85 mW cm^{-2} in RZABs. Importantly, these catalyst materials exhibited remarkable stability with minimal degradation during galvanostatic charge-

discharge cycling in RZABs. The results obtained from the AEMFC and RZAB experiments suggest significant potential for bimetallic phthalocyanine-derived electrocatalysts in these electrochemical energy conversion devices. Later, FePc was doped onto a composite of carbide-derived carbon (CDC) and graphene (G) to prepare highly micro- and mesoporous catalysts [IV]. FeN-CDC/G/DCDA with additional nitrogen source dicyandiamide (DCDA) exhibited good ORR activity in acidic media with half-wave potential ($E_{1/2}$) of 0.76 V vs RHE [IV].

Third part of the thesis aimed to develop carbon supports from polymer-framework [V,VI]. The controlled synthesis of phloroglucinol-formaldehyde networks should result in a combination of micro- and mesoporous carbon structures. Cobalt- and nitrogen-doped porous carbon material was created through the utilisation of phloroglucinol-formaldehyde polymer networks, in conjunction with 2-methylimidazole and cobalt phthalocyanine as precursor materials [V]. The higher cobalt content and hierarchical porous structure within CoN-PC-2 catalyst displayed robust bifunctional electrocatalytic activity for both the ORR and OER in alkaline media. It exhibited $E_{1/2}$ of 0.81 V for ORR and $E_{j=10}$ of 1.70 V for OER. Furthermore, CoN-PC-2 exhibited impressive performance in RZABs, as evidenced by an open-circuit voltage (OCV) of 1.47 V, P_{max} of 158 mW cm^{-2} and notable stability over 45 h [V]. Next, a cost-effective method was introduced for the synthesis of atomically dispersed catalysts derived from phloroglucinol-dicyandiamide-formaldehyde (PDF) frameworks. The zinc-templated atomically dispersed bimetal-doped FeCoN-PDF-T_2-2 catalyst demonstrated exceptional bifunctional electrocatalytic activity for both the ORR and OER, due to the highly mesoporous structure and atomically dispersed metal sites [VI]. Specifically, FeCoN-PDF-T_2-2 exhibited a low ΔE value of 0.75 V, comparable to commercial PtRu/C catalysts. The outstanding bifunctional electrocatalytic activity was attributed to well-dispersed active sites, as confirmed through scanning transmission electron microscopy (STEM) measurements and the synergistic effects of iron and cobalt, RZABs based on FeCoN-PDF-T_2-2 achieved a remarkable P_{max} of 258 mW cm^{-2}, outperforming PtRu/C-based RZABs (P_{max}=185 mW cm^{-2}) [VI]. These results present a simple synthesis route for the development of bifunctional electrocatalysts derived from polymer materials for ORR and OER, potentially opening new avenues for highly stable atomically dispersed electrocatalysts in renewable electrochemical energy storage devices.

The research conducted in this doctoral thesis offers insights into the ORR and OER catalyst development for various electrochemical energy technologies, such as AEMFCs and RZABs. The study explores the specific advantages of bimetallic M-N-C catalysts incorporating iron along with other OER-active metals (Co, Ni), which demonstrate superior performance. The study also emphasises the effect of different synthesis techniques and structural attributes of these catalysts, which play a pivotal role in enhancing their remarkable bifunctional electrocatalytic activity. Consequently, this doctoral thesis signifies a valuable addition to the scope of bifunctional ORR/OER electrocatalysis using non-precious metal catalysts.

9. REFERENCES

[1] H. Nazir, N. Muthuswamy, C. Louis, S. Jose, J. Prakash, M.E.M. Buan, C. Flox, S. Chavan, X. Shi, P. Kauranen, T. Kallio, G. Maia, K. Tammeveski, N. Lymperopoulos, E. Carcadea, E. Veziroglu, A. Iranzo, A.M. Kannan, Is the H_2 economy realizable in the foreseeable future? Part III: H_2 usage technologies, applications, and challenges and opportunities, Int. J. Hydrog. Energy 45 (2020) 28217–28239. https://doi.org/10.1016/j.ijhydene.2020.07.256.

[2] I. Staffell, D. Scamman, A.V. Abad, P. Balcombe, P.E. Dodds, P. Ekins, N. Shah, K.R. Ward, The role of hydrogen and fuel cells in the global energy system, Energy Environ. Sci. 12 (2019) 463–491. https://doi.org/10.1039/c8ee01157e.

[3] W.F. Pickard, A.Q. Shen, N.J. Hansing, Parking the power: Strategies and physical limitations for bulk energy storage in supply–demand matching on a grid whose input power is provided by intermittent sources, Renew. Sustain. Energy Rev. 13 (2009) 1934–1945. https://doi.org/10.1016/j.rser.2009.03.002.

[4] H.A. Firouzjaie, W.E. Mustain, Catalytic advantages, challenges, and priorities in alkaline membrane fuel cells, ACS Catal. 10 (2020) 225–234. https://doi.org/10.1021/acscatal.9b03892.

[5] J. Fu, R. Liang, G. Liu, A. Yu, Z. Bai, L. Yang, Z. Chen, Recent progress in electrically rechargeable zinc–air batteries, Adv. Mater. 31 (2019) 1805230. https://doi.org/10.1002/adma.201805230.

[6] R. Othman, A.L. Dicks, Z. Zhu, Non precious metal catalysts for the PEM fuel cell cathode, Int. J. Hydrog. Energy 37 (2012) 357–372. https://doi.org/10.1016/j.ijhydene.2011.08.095.

[7] Y. Liu, X. Yue, K. Li, J. Qiao, D.P. Wilkinson, J. Zhang, PEM fuel cell electrocatalysts based on transition metal macrocyclic compounds, Coord. Chem. Rev. 315 (2016) 153–177. https://doi.org/10.1016/j.ccr.2016.02.002.

[8] M.A. Abdelkareem, T. Wilberforce, K. Elsaid, E.T. Sayed, E.A.M. Abdelghani, A.G. Olabi, Transition metal carbides and nitrides as oxygen reduction reaction catalyst or catalyst support in proton exchange membrane fuel cells (PEMFCs), Int. J. Hydrog. Energy 46 (2021) 23529–23547. https://doi.org/10.1016/j.ijhydene.2020.08.250.

[9] Y. Kumar, M. Mooste, K. Tammeveski, Recent progress of transition metal-based bifunctional electrocatalysts for rechargeable zinc–air battery application, Curr. Opin. Electrochem. 38 (2023) 101229. https://doi.org/10.1016/j.coelec.2023.101229.

[10] M.M. Hossen, M.S. Hasan, M.R.I. Sardar, J. bin Haider, Mottakin, K. Tammeveski, P. Atanassov, State-of-the-art and developmental trends in platinum group metal-free cathode catalyst for anion exchange membrane fuel cell (AEMFC), Appl. Catal. B Environ. 325 (2023) 121733. https://doi.org/10.1016/j.apcatb.2022.121733.

[11] A.K. Ipadeola, A.B. Haruna, L. Gaolatlhe, A.K. Lebechi, J. Meng, Q. Pang, K. Eid, A.M. Abdullah, K.I. Ozoemena, Efforts at enhancing bifunctional electrocatalysis and related events for rechargeable zinc-air batteries, ChemElectroChem 8 (2021) 3998–4018. https://doi.org/10.1002/celc.202100574.

[12] A. Sarapuu, J. Lilloja, S. Akula, J.H. Zagal, S. Specchia, K. Tammeveski, Recent advances in non-precious metal single-atom electrocatalysts for oxygen reduction reaction in low-temperature polymer-electrolyte fuel cells, ChemCatChem (2023) e202300849. https://doi.org/10.1002/cctc.202300849.

[13] M. Luo, W. Sun, B.B. Xu, H. Pan, Y. Jiang, Interface engineering of air electrocatalysts for rechargeable zinc–air batteries, Adv. Energy Mater. 11 (2021) 2002762. https://doi.org/10.1002/aenm.202002762.
[14] X. Ren, Q. Lv, L. Liu, B. Liu, Y. Wang, A. Liu, G. Wu, Current progress of Pt and Pt-based electrocatalysts used for fuel cells, Sustain. Energy Fuels 4 (2020) 15–30. https://doi.org/10.1039/c9se00460b.
[15] Q. Shi, C. Zhu, D. Du, Y. Lin, Robust noble metal-based electrocatalysts for oxygen evolution reaction, Chem. Soc. Rev. 48 (2019) 3181–3192. https://doi.org/10.1039/c8cs00671g.
[16] A. Kumar, S. Ibraheem, T. Anh Nguyen, R.K. Gupta, T. Maiyalagan, G. Yasin, Molecular-MN_4 vs atomically dispersed $M{-}N_4{-}C$ electrocatalysts for oxygen reduction reaction, Coord. Chem. Rev. 446 (2021) 214122. https://doi.org/10.1016/j.ccr.2021.214122.
[17] A. Kumar, Y. Zhang, W. Liu, X. Sun, The chemistry, recent advancements and activity descriptors for macrocycles based electrocatalysts in oxygen reduction reaction, Coord. Chem. Rev. 402 (2020) 213047. https://doi.org/10.1016/j.ccr.2019.213047.
[18] S. Aralekallu, L.K. Sannegowda, V. Singh, Developments in electrocatalysts for electrocatalytic hydrogen evolution reaction with reference to bio-inspired phthalocyanines, Int. J. Hydrog. Energy 48 (2023) 16569–16592. https://doi.org/10.1016/j.ijhydene.2023.01.169.
[19] S. Yamazaki, Metalloporphyrins and related metallomacrocycles as electrocatalysts for use in polymer electrolyte fuel cells and water electrolyzers, Coord. Chem. Rev. 373 (2018) 148–166. https://doi.org/10.1016/j.ccr.2017.09.016.
[20] D. Wang, X. Pan, P. Yang, R. Li, H. Xu, Y. Li, F. Meng, J. Zhang, M. An, Transition metal and nitrogen co-doped carbon-based electrocatalysts for the oxygen reduction reaction: from active site insights to the rational design of precursors and structures, ChemSusChem 14 (2021) 33–55. https://doi.org/10.1002/cssc.202002137.
[21] V.K. Vashistha, A. Kumar, Design and synthesis of MnN_4 macrocyclic complex for efficient oxygen reduction reaction electrocatalysis, Inorg. Chem. Commun. 112 (2020) 107700. https://doi.org/10.1016/j.inoche.2019.107700.
[22] Y. Hong, L. Li, B. Huang, X. Tang, W. Zhai, T. Hu, K. Yuan, Y. Chen, Molecular control of carbon-based oxygen reduction electrocatalysts through metal macrocyclic complexes functionalization, Adv. Energy Mater. 11 (2021) 2100866. https://doi.org/10.1002/aenm.202100866.
[23] T. Marshall-Roth, N.J. Libretto, A.T. Wrobel, K.J. Anderton, M.L. Pegis, N.D. Ricke, T.V. Voorhis, J.T. Miller, Y. Surendranath, A pyridinic Fe-N_4 macrocycle models the active sites in Fe/N-doped carbon electrocatalysts, Nat. Commun. 11 (2020) 5283. https://doi.org/10.1038/s41467-020-18969-6.
[24] F. Xiao, Y.-C. Wang, Z.-P. Wu, G. Chen, F. Yang, S. Zhu, K. Siddharth, Z. Kong, A. Lu, J.-C. Li, C.-J. Zhong, Z.-Y. Zhou, M. Shao, Recent advances in electrocatalysts for proton exchange membrane fuel cells and alkaline membrane fuel cells, Adv. Mater. 33 (2021) 2006292. https://doi.org/10.1002/adma.202006292.
[25] K. Jiao, J. Xuan, Q. Du, Z. Bao, B. Xie, B. Wang, Y. Zhao, L. Fan, H. Wang, Z. Hou, S. Huo, N.P. Brandon, Y. Yin, M.D. Guiver, Designing the next generation of proton-exchange membrane fuel cells, Nature 595 (2021) 361–369. https://doi.org/10.1038/s41586-021-03482-7.

[26] B. Yang, Z. Cunman, Progress in constructing high-performance anion exchange Membrane: Molecular design, microphase controllability and In-device property, Chem. Eng. J. 457 (2023) 141094. https://doi.org/10.1016/j.cej.2022.141094.
[27] M. Mandal, Recent advancement on anion exchange membranes for fuel cell and water electrolysis, ChemElectroChem 8 (2021) 36–45. https://doi.org/10.1002/celc.202001329.
[28] N. Chen, Y.M. Lee, Anion exchange polyelectrolytes for membranes and ionomers, Prog. Polym. Sci. 113 (2021) 101345. https://doi.org/10.1016/j.progpolymsci.2020.101345.
[29] P.C. Okonkwo, O.O. Ige, E.M. Barhoumi, P.C. Uzoma, W. Emori, A. Benamor, A.M. Abdullah, Platinum degradation mechanisms in proton exchange membrane fuel cell (PEMFC) system: A review, Int. J. Hydrog. Energy 46 (2021) 15850–15865. https://doi.org/10.1016/j.ijhydene.2021.02.078.
[30] J. Cui, Q. Chen, X. Li, S. Zhang, Recent advances in non-precious metal electrocatalysts for oxygen reduction in acidic media and PEMFCs: an activity, stability and mechanism study, Green Chem. 23 (2021) 6898–6925. https://doi.org/10.1039/d1gc01040a.
[31] M. Hren, M. Božič, D. Fakin, K. Stana Kleinschek, S. Gorgieva, Alkaline membrane fuel cells: anion exchange membranes and fuels, Sustain. Energy Fuels 5 (2021) 604–637. https://doi.org/10.1039/d0se01373k.
[32] J. Zhang, W. Zhu, T. Huang, C. Zheng, Y. Pei, G. Shen, Z. Nie, D. Xiao, Y. Yin, M.D. Guiver, Recent insights on catalyst layers for anion exchange membrane fuel cells, Adv. Sci. 8 (2021) 2100284. https://doi.org/10.1002/advs.202100284.
[33] J. Masa, W. Xia, M. Muhler, W. Schuhmann, On the role of metals in nitrogen-doped carbon electrocatalysts for oxygen reduction, Angew. Chem. Int. Ed. 54 (2015) 10102–10120. https://doi.org/10.1002/anie.201500569.
[34] C. Zúñiga, C. Candia-Onfray, R. Venegas, K. Muñoz, J. Urra, M. Sánchez-Arenillas, J.F. Marco, J.H. Zagal, F.J. Recio, Elucidating the mechanism of the oxygen reduction reaction for pyrolyzed Fe-N-C catalysts in basic media, Electrochem. Commun. 102 (2019) 78–82. https://doi.org/10.1016/j.elecom.2019.04.005.
[35] N. Ziv, A.N. Mondal, T. Weissbach, S. Holdcroft, D.R. Dekel, Effect of CO2 on the properties of anion exchange membranes for fuel cell applications, J. Membr. Sci. 586 (2019) 140–150. https://doi.org/10.1016/j.memsci.2019.05.053.
[36] H. Yanagi, K. Fukuta, Anion exchange membrane and ionomer for alkaline membrane fuel cells (AMFCs), ECS Trans. 16 (2008) 257. https://doi.org/10.1149/1.2981860.
[37] S. Suzuki, H. Muroyama, T. Matsui, K. Eguchi, Influence of CO_2 dissolution into anion exchange membrane on fuel cell performance, Electrochim. Acta. 88 (2013) 552–558. https://doi.org/10.1016/j.electacta.2012.10.105.
[38] N. Ramaswamy, S. Mukerjee, Alkaline Anion-exchange membrane fuel cells: challenges in electrocatalysis and interfacial charge transfer, Chem. Rev. 119 (2019) 11945–11979. https://doi.org/10.1021/acs.chemrev.9b00157.
[39] R. Gutru, Z. Turtayeva, F. Xu, G. Maranzana, B. Vigolo, A. Desforges, A comprehensive review on water management strategies and developments in anion exchange membrane fuel cells, Int. J. Hydrog. Energy 45 (2020) 19642–19663. https://doi.org/10.1016/j.ijhydene.2020.05.026.
[40] Louis maiche, US243454A, United State Patent, 28 June 1881.

[41] J.-N. Liu, C.-X. Zhao, J. Wang, D. Ren, B.-Q. Li, Q. Zhang, A brief history of zinc–air batteries: 140 years of epic adventures, Energy Environ. Sci. 15 (2022) 4542–4553. https://doi.org/10.1039/d2ee02440c.
[42] J. Pan, Y.Y. Xu, H. Yang, Z. Dong, H. Liu, B.Y. Xia, Advanced architectures and relatives of air electrodes in Zn–air batteries, Adv. Sci. 5 (2018) 1700691. https://doi.org/10.1002/advs.201700691.
[43] D. Linden, Fuel Energy Abstracts: Handbook of batteries, 2nd ed.; Elsevier: Amsterdam, Netherlands, 1995.
[44] X.-W. Lv, Z. Wang, Z. Lai, Y. Liu, T. Ma, J. Geng, Z.-Y. Yuan, Rechargeable zinc–air batteries: advances, challenges, and prospects, Small (2023) 2306396. https://doi.org/10.1002/smll.202306396.
[45] L. Wei, E.H. Ang, Y. Yang, Y. Qin, Y. Zhang, M. Ye, Q. Liu, C.C. Li, Recent advances of transition metal based bifunctional electrocatalysts for rechargeable zinc-air batteries, J. Power Sources 477 (2020) 228696. https://doi.org/10.1016/j.jpowsour.2020.228696.
[46] T. Noor, L. Yaqoob, N. Iqbal, Recent advances in electrocatalysis of oxygen evolution reaction using noble-metal, transition-metal, and carbon-based materials, ChemElectroChem 8 (2021) 447–483. https://doi.org/10.1002/celc.202001441.
[47] M.T. Tsehaye, F. Alloin, C. Iojoiu, R.A. Tufa, D. Aili, P. Fischer, S. Velizarov, Membranes for zinc-air batteries: Recent progress, challenges and perspectives, J. Power Sources 475 (2020) 228689. https://doi.org/10.1016/j.jpowsour.2020.228689.
[48] M.K. Singla, P. Nijhawan, A.S. Oberoi, Hydrogen fuel and fuel cell technology for cleaner future: a review, Environ. Sci. Pollut. Res. 28 (2021) 15607–15626. https://doi.org/10.1007/s11356-020-12231-8.
[49] P. A. Christensen, A. Hamnett, D. Linares-Moya, Oxygen reduction and fuel oxidation in alkaline solution, Phys. Chem. Chem. Phys. 13 (2011) 5206–5214. https://doi.org/10.1039/c0cp02365e.
[50] Y. Yang, C.R. Peltier, R. Zeng, R. Schimmenti, Q. Li, X. Huang, Z. Yan, G. Potsi, R. Selhorst, X. Lu, W. Xu, M. Tader, A.V. Soudackov, H. Zhang, M. Krumov, E. Murray, P. Xu, J. Hitt, L. Xu, H.-Y. Ko, B.G. Ernst, C. Bundschu, A. Luo, D. Markovich, M. Hu, C. He, H. Wang, J. Fang, R.A.Jr. DiStasio, L.F. Kourkoutis, A. Singer, K.J.T. Noonan, L. Xiao, L. Zhuang, B.S. Pivovar, P. Zelenay, E. Herrero, J.M. Feliu, J. Suntivich, E.P. Giannelis, S. Hammes-Schiffer, T. Arias, M. Mavrikakis, T.E. Mallouk, J.D. Brock, D.A. Muller, F.J. DiSalvo, G.W. Coates, H.D. Abruña, Electrocatalysis in alkaline media and alkaline membrane-based energy technologies, Chem. Rev. 122 (2022) 6117–6321. https://doi.org/10.1021/acs.chemrev.1c00331.
[51] K. Zhang, R. Zou, Advanced transition metal-based OER electrocatalysts: current status, opportunities, and challenges, Small 17 (2021) 2100129. https://doi.org/10.1002/smll.202100129.
[52] J. Shan, Y. Zheng, B. Shi, K. Davey, S.-Z. Qiao, Regulating electrocatalysts via surface and interface engineering for acidic water electrooxidation, ACS Energy Lett. 4 (2019) 2719–2730. https://doi.org/10.1021/acsenergylett.9b01758.
[53] I.C. Man, H.-Y. Su, F. Calle-Vallejo, H.A. Hansen, J.I. Martínez, N.G. Inoglu, J. Kitchin, T.F. Jaramillo, J.K. Nørskov, J. Rossmeisl, Universality in oxygen evolution electrocatalysis on oxide surfaces, ChemCatChem 3 (2011) 1159–1165. https://doi.org/10.1002/cctc.201000397.

[54] N.-T. Suen, S.-F. Hung, Q. Quan, N. Zhang, Y.-J. Xu, H.M. Chen, Electrocatalysis for the oxygen evolution reaction: recent development and future perspectives, Chem. Soc. Rev. 46 (2017) 337–365. https://doi.org/10.1039/C6CS00328A.

[55] A. Damjanovic, B. Jovanovic, Anodic oxide films as barriers to charge transfer in O_2 evolution at Pt in acid solutions, J. Electrochem. Soc. 123 (1976) 374. https://doi.org/ 10.1149/1.2132828.

[56] T. Binninger, R. Mohamed, K. Waltar, E. Fabbri, P. Levecque, R. Kötz, T.J. Schmidt, Thermodynamic explanation of the universal correlation between oxygen evolution activity and corrosion of oxide catalysts, Sci. Rep. 5 (2015) 12167. https://doi.org/10.1038/srep12167.

[57] Y.-C. Zhang, S. Ullah, R. Zhang, L. Pan, X. Zhang, J.-J. Zou, Manipulating electronic delocalization of Mn_3O_4 by manganese defects for oxygen reduction reaction, Appl. Catal. B Environ. 277 (2020) 119247. https://doi.org/10.1016/j.apcatb.2020.119247.

[58] J. Sun, L. Du, B. Sun, G. Han, Y. Ma, J. Wang, H. Huo, C. Du, G. Yin, Bifunctional $LaMn_{0.3}Co_{0.7}O_3$ perovskite oxide catalyst for oxygen reduction and evolution reactions: the optimized e_g electronic structures by manganese dopant, ACS Appl. Mater. Interfaces 12 (2020) 24717–24725. https://doi.org/10.1021/acsami.0c03983.

[59] A. Pendashteh, J.S. Sanchez, J. Palma, M. Anderson, R. Marcilla, Anchored $NiCoMnS_4$ nanoparticles on N-doped rGO: High-performance bifunctional electrocatalysts for rechargeable Zn-Air batteries, Energy Storage Mater. 20 (2019) 216–224. https://doi.org/10.1016/j.ensm.2019.04.018.

[60] J. Luo, X. Tian, J. Zeng, Y. Li, H. Song, S. Liao, Limitations and improvement strategies for early-transition-metal nitrides as competitive catalysts toward the oxygen reduction reaction, ACS Catal. 6 (2016) 6165–6174. https://doi.org/10.1021/acscatal.6b01618.

[61] H. Shang, W. Sun, R. Sui, J. Pei, L. Zheng, J. Dong, Z. Jiang, D. Zhou, Z. Zhuang, W. Chen, J. Zhang, D. Wang, Y. Li, Engineering Isolated $Mn–N_2C_2$ atomic interface sites for efficient bifunctional oxygen reduction and evolution reaction, Nano Lett. 20 (2020) 5443–5450. https://doi.org/10.1021/acs.nanolett.0c01925.

[62] M. Liu, X. Xiao, Q. Li, L. Luo, M. Ding, B. Zhang, Y. Li, J. Zou, B. Jiang, Recent progress of electrocatalysts for oxygen reduction in fuel cells, J. Colloid Interface Sci. 607 (2022) 791–815. https://doi.org/10.1016/j.jcis.2021.09.008.

[63] W. Xiong, H. Yin, T. Wu, H. Li, Challenges and Opportunities of Transition Metal Oxides as Electrocatalysts, Chem. Eur. J. 29 (2023) e202202872. https://doi.org/10.1002/chem.202202872.

[64] R. Jacobs, J. Hwang, Y. Shao-Horn, D. Morgan, Assessing correlations of perovskite catalytic performance with electronic structure descriptors, Chem. Mater. 31 (2019) 785–797. https://doi.org/10.1021/acs.chemmater.8b03840.

[65] C. Mu, J. Mao, J. Guo, Q. Guo, Z. Li, W. Qin, Z. Hu, K. Davey, T. Ling, S.-Z. Qiao, Rational design of spinel cobalt vanadate oxide Co_2VO_4 for superior electrocatalysis, Adv. Mater. 32 (2020) 1907168. https://doi.org/10.1002/adma.201907168.

[66] Z. Pan, H. Chen, J. Yang, Y. Ma, Q. Zhang, Z. Kou, X. Ding, Y. Pang, L. Zhang, Q. Gu, C. Yan, J. Wang, $CuCo_2S_4$ nanosheets@N-doped carbon nanofibers by sulfurization at room temperature as bifunctional electrocatalysts in flexible

quasi-solid-state Zn–air batteries, Adv. Sci. 6 (2019) 1900628. https://doi.org/10.1002/advs.201900628.
[67] C.-X. Zhao, B.-Q. Li, J.-N. Liu, Q. Zhang, Intrinsic electrocatalytic activity regulation of M–N–C single-atom catalysts for the oxygen reduction reaction, Angew. Chem. Int. Ed. 60 (2021) 4448–4463. https://doi.org/10.1002/anie.202003917.
[68] W.-C. Chen, G. Yang, Y. Zhao, G.-Q. Yuan, J.-S. Ye, H.-Y. Liu, X.-Y. Xiao, Porous carbon polyhedrons with exclusive Metal-N_X moieties for efficient oxygen reduction reaction, Int. J. Hydrog. Energy 46 (2021) 39882–39891. https://doi.org/10.1016/j.ijhydene.2021.09.244.
[69] S. Kattel, P. Atanassov, B. Kiefer, Catalytic activity of Co–N_x/C electrocatalysts for oxygen reduction reaction: a density functional theory study, Phys. Chem. Chem. Phys. 15 (2012) 148–153. https://doi.org/10.1039/C2CP42609A.
[70] J. Woo, H. Choi, Y.J. Sa, H.Y. Kim, T. Lim, J.-H. Jang, S.J. Yoo, J.Y. Kim, C.S. Kim, S.H. Joo, Structural evolution of atomically dispersed Fe Species in Fe–N/C catalysts probed by X-ray absorption and 57Fe Mössbauer spectroscopies, J. Phys. Chem. C 125 (2021) 11928–11938. https://doi.org/10.1021/acs.jpcc.1c01333.
[71] J. Woo, S.Y. Yang, Y.J. Sa, W.-Y. Choi, M.-H. Lee, H.-W. Lee, T.J. Shin, T.-Y. Kim, S.H. Joo, Promoting oxygen reduction reaction activity of Fe–N/C electrocatalysts by silica-coating-mediated synthesis for anion-exchange membrane fuel cells, Chem. Mater. 30 (2018) 6684–6701. https://doi.org/10.1021/acs.chemmater.8b02117.
[72] M.M. Hossen, K. Artyushkova, P. Atanassov, A. Serov, Synthesis and characterization of high performing Fe-N-C catalyst for oxygen reduction reaction (ORR) in Alkaline Exchange Membrane Fuel Cells, J. Power Sources 375 (2018) 214–221. https://doi.org/10.1016/j.jpowsour.2017.08.036.
[73] X. Ning, Y. Li, J. Ming, Q. Wang, H. Wang, Y. Cao, F. Peng, Y. Yang, H. Yu, Electronic synergism of pyridinic- and graphitic-nitrogen on N-doped carbons for the oxygen reduction reaction, Chem. Sci. 10 (2019) 1589–1596. https://doi.org/10.1039/c8sc04596h.
[74] M. Skorupska, A. Ilnicka, J.P. Lukaszewicz, The effect of nitrogen species on the catalytic properties of N-doped graphene, Sci. Rep. 11 (2021) 23970. https://doi.org/10.1038/s41598-021-03403-8.
[75] M. Zerner, M. Gouterman, Porphyrins, Theor. Chim. Acta 4 (1966) 44–63. https://doi.org/10.1007/BF00526010.
[76] S. Juvanen, A. Sarapuu, S. Vlassov, M. Kook, V. Kisand, M. Käärik, A. Treshchalov, J. Aruväli, J. Kozlova, A. Tamm, J. Leis, K. Tammeveski, Iron-containing nitrogen-doped carbon nanomaterials prepared via NaCl template as efficient electrocatalysts for the oxygen reduction reaction, ChemElectroChem 8 (2021) 2288–2297. https://doi.org/10.1002/celc.202100571.
[77] K. Kisand, A. Sarapuu, J.C. Douglin, A. Kikas, A. Treshchalov, M. Käärik, H.-M. Piirsoo, P. Paiste, J. Aruväli, J. Leis, V. Kisand, A. Tamm, D.R. Dekel, K. Tammeveski, Templated nitrogen-, iron-, and cobalt-doped mesoporous nanocarbon derived from an alkylresorcinol mixture for anion-exchange membrane fuel cell application, ACS Catal. 12 (2022) 14050–14061. https://doi.org/10.1021/acscatal.2c03683.
[78] J. Lilloja, M. Mooste, E. Kibena-Põldsepp, A. Sarapuu, A. Kikas, V. Kisand, M. Käärik, J. Kozlova, A. Treshchalov, P. Paiste, J. Aruväli, J. Leis, A. Tamm, S. Holdcroft, K. Tammeveski, Cobalt-, iron- and nitrogen-containing ordered

mesoporous carbon-based catalysts for anion-exchange membrane fuel cell cathode, Electrochim. Acta 439 (2023) 141676. https://doi.org/10.1016/j.electacta.2022.141676.

[79] J. Lilloja, E. Kibena-Põldsepp, A. Sarapuu, A. Konovalova, M. Käärik, J. Kozlova, P. Paiste, A. Kikas, A. Treshchalov, J. Aruväli, A. Zitolo, J. Leis, A. Tamm, V. Kisand, S. Holdcroft, K. Tammeveski, Transition-metal and nitrogen-doped carbon nanotube/graphene composites as cathode catalysts for anion-exchange membrane fuel cells, ACS Appl. Energy Mater. 6 (2023) 5519–5529. https://doi.org/10.1021/acsaem.3c00613.

[80] A. Kumar, G. Zhang, W. Liu, X. Sun, Electrocatalysis and activity descriptors with metal phthalocyanines for energy conversion reactions, J. Electroanal. Chem. 922 (2022) 116799. https://doi.org/10.1016/j.jelechem.2022.116799.

[81] L. Osmieri, A.H.A. Monteverde Videla, P. Ocón, S. Specchia, Kinetics of oxygen electroreduction on Me–N–C (Me = Fe, Co, Cu) catalysts in acidic medium: insights on the effect of the transition metal, J. Phys. Chem. C 121 (2017) 17796–17817. https://doi.org/10.1021/acs.jpcc.7b02455.

[82] U.I. Kramm, J. Herranz, N. Larouche, T.M. Arruda, M. Lefèvre, F. Jaouen, P. Bogdanoff, S. Fiechter, I. Abs-Wurmbach, S. Mukerjee, J.-P. Dodelet, Structure of the catalytic sites in Fe/N/C-catalysts for O_2-reduction in PEM fuel cells, Phys. Chem. Chem. Phys. 14 (2012) 11673–11688. https://doi.org/10.1039/c2cp41957b.

[83] J.-S.M. Lee, Y. Fujiwara, S. Kitagawa, S. Horike, Homogenized bimetallic catalysts from metal–organic framework alloys, Chem. Mater. 31 (2019) 4205–4212. https://doi.org/10.1021/acs.chemmater.9b01093.

[84] K. Zhao, Y. Shu, F. Li, G. Peng, Bimetallic catalysts as electrocatalytic cathode materials for the oxygen reduction reaction in microbial fuel cell: A review, Green Energy Environ. 8 (2023) 1043–1070. https://doi.org/10.1016/j.gee.2022.10.007.

[85] L. Guo, Y. Hu, X. Zhao, X. Peng, X. Zhang, X. Yu, X. Yang, Z. Lu, L. Li, Secondary doping of Mn/Co bimetallic ZIF-derived catalysts for the oxygen reduction reaction, New J. Chem. 47 (2023) 12123–12132. https://doi.org/10.1039/D3NJ01840G.

[86] M. Zhou, Z. Zhu, Y. Ju, Y. Zhai, L. Jiao, M. Liu, W. Yang, J. Tang, Bimetallic FeCo−N−C catalyst for efficient oxygen reduction reaction, Electroanalysis 34 (2022) 1572–1578. https://doi.org/10.1002/elan.202200009.

[87] S. Xia, H. Yang, W. Lu, N. Cai, H. Xiao, X. Chen, Y. Chen, X. Wang, S. Wang, P. Wu, H. Chen, Fe–Co based synergistic catalytic graphitization of biomass: Influence of the catalyst type and the pyrolytic temperature, Energy 239 (2022) 122262. https://doi.org/10.1016/j.energy.2021.122262.

[88] J. Yang, J.K. Cooper, F.M. Toma, K.A. Walczak, M. Favaro, J.W. Beeman, L.H. Hess, C. Wang, C. Zhu, S. Gul, J. Yano, C. Kisielowski, A. Schwartzberg, I.D. Sharp, A multifunctional biphasic water splitting catalyst tailored for integration with high-performance semiconductor photoanodes, Nat. Mater. 16 (2017) 335–341. https://doi.org/10.1038/nmat4794.

[89] S. Niu, W.-J. Jiang, Z. Wei, T. Tang, J. Ma, J.-S. Hu, L.-J. Wan, Se-doping activates FeOOH for cost-effective and efficient electrochemical water oxidation, J. Am. Chem. Soc. 141 (2019) 7005–7013. https://doi.org/10.1021/jacs.9b01214.

[90] R.D.L. Smith, M.S. Prévot, R.D. Fagan, Z. Zhang, P.A. Sedach, M.K.J. Siu, S. Trudel, C.P. Berlinguette, Photochemical route for accessing amorphous metal

oxide materials for water oxidation catalysis, Science 340 (2013) 60–63. https://doi.org/10.1126/science.1233638.
[91] M. Huynh, C. Shi, S.J.L. Billinge, D.G. Nocera, Nature of activated manganese oxide for oxygen evolution, J. Am. Chem. Soc. 137 (2015) 14887–14904. https://doi.org/10.1021/jacs.5b06382.
[92] J. Song, C. Wei, Z.-F. Huang, C. Liu, L. Zeng, X. Wang, Z.J. Xu, A review on fundamentals for designing oxygen evolution electrocatalysts, Chem. Soc. Rev. 49 (2020) 2196–2214. https://doi.org/10.1039/C9CS00607A.
[93] T. Tian, H. Gao, X. Zhou, L. Zheng, J. Wu, K. Li, Y. Ding, Study of the active sites in porous nickel oxide nanosheets by manganese modulation for enhanced oxygen evolution catalysis, ACS Energy Lett. 3 (2018) 2150–2158. https://doi.org/10.1021/acsenergylett.8b01206.
[94] L. Kuai, J. Geng, C. Chen, E. Kan, Y. Liu, Q. Wang, B. Geng, A reliable aerosol-spray-assisted approach to produce and optimize amorphous metal oxide catalysts for electrochemical water splitting, Angew. Chem. Int. Ed. 53 (2014) 7547–7551. https://doi.org/10.1002/anie.201404208.
[95] D. Zhang, L. Meng, J. Shi, N. Wang, S. Liu, C. Li, One-step preparation of optically transparent Ni-Fe oxide film electrocatalyst for oxygen evolution reaction, Electrochim. Acta 169 (2015) 402–408. https://doi.org/10.1016/j.electacta.2015. 04.101.
[96] C. Guo, X. Sun, X. Kuang, L. Gao, M. Zhao, L. Qu, Y. Zhang, D. Wu, X. Ren, Q. Wei, Amorphous Co-doped MoO_x nanospheres with a core–shell structure toward an effective oxygen evolution reaction, J. Mater. Chem. A 7 (2019) 1005–1012. https://doi.org/10.1039/C8TA05552A.
[97] A. Meng, X. Yuan, T. Shen, J. Zhao, G. Song, Y. Lin, Z. Li, Amorphous nickel sulfide nanoparticles anchored on N-doped graphene nanotubes with superior properties for high-performance supercapacitors and efficient oxygen evolution reaction, Nanoscale 12 (2020) 4655–4666. https://doi.org/10.1039/C9NR09654J.
[98] O. Mabayoje, A. Shoola, B.R. Wygant, C.B. Mullins, The role of anions in metal chalcogenide oxygen evolution catalysis: electrodeposited thin films of nickel sulfide as “pre-catalysts,” ACS Energy Lett. 1 (2016) 195–201. https://doi.org/10.1021/acsenergylett.6b00084.
[99] W. Chen, H. Wang, Y. Li, Y. Liu, J. Sun, S. Lee, J.-S. Lee, Y. Cui, In situ electrochemical oxidation tuning of transition metal disulfides to oxides for enhanced water oxidation, ACS Cent. Sci. 1 (2015) 244–251. https://doi.org/10.1021/acscentsci.5b00227.
[100] X. Liu, Q. Yin, C. Dai, G. Li, J. Lian, Y. Zhao, S. Yang, H. Li, Amorphous bimetallic phosphate–carbon precatalyst with deep self-reconstruction toward efficient oxygen evolution reaction and Zn–air batteries, ACS Sustain. Chem. Eng. 9 (2021) 5345–5355. https://doi.org/10.1021/acssuschemeng.0c09339.
[101] X. Xu, F. Song, X. Hu, A nickel iron diselenide-derived efficient oxygen-evolution catalyst, Nat. Commun. 7 (2016) 12324. https://doi.org/10.1038/ncomms12324.
[102] Z. Pu, T. Liu, I.S. Amiinu, R. Cheng, P. Wang, C. Zhang, P. Ji, W. Hu, J. Liu, S. Mu, Transition-Metal Phosphides: Activity Origin, Energy-Related Electrocatalysis Applications, and Synthetic Strategies, Adv. Funct. Mater. 30 (2020) 2004009. https://doi.org/10.1002/adfm.202004009.
[103] J. Zhang, H. Li, P. Guo, H. Ma, X. S. Zhao, Rational design of graphitic carbon based nanostructures for advanced electrocatalysis, J. Mater. Chem. A 4 (2016) 8497–8511. https://doi.org/10.1039/C6TA01657J.

[104] S. Yuan, Q. Gao, C. Ke, T. Zuo, J. Hou, J. Zhang, Mesoporous carbon materials for electrochemical energy storage and conversion, ChemElectroChem 9 (2022) e202101182. https://doi.org/10.1002/celc.202101182.
[105] J. Quílez-Bermejo, E. Morallón, D. Cazorla-Amorós, Metal-free heteroatom-doped carbon-based catalysts for ORR: A critical assessment about the role of heteroatoms, Carbon 165 (2020) 434–454. https://doi.org/10.1016/j.carbon.2020.04.068.
[106] J. Wang, Y. Zhao, B.P. Setzler, S. Rojas-Carbonell, C. Ben Yehuda, A. Amel, M. Page, L. Wang, K. Hu, L. Shi, S. Gottesfeld, B. Xu, Y. Yan, Poly(aryl piperidinium) membranes and ionomers for hydroxide exchange membrane fuel cells, Nat. Energy 4 (2019) 392–398. https://doi.org/10.1038/s41560-019-0372-8.
[107] M.A. Hickner, A.M. Herring, E.B. Coughlin, Anion exchange membranes: Current status and moving forward, J. Polym. Sci. Part B: Polym. Phys. 51 (2013) 1727–1735. https://doi.org/10.1002/polb.23395.
[108] J.R. Varcoe, R.C.T. Slade, Prospects for alkaline anion-exchange membranes in low temperature fuel cells, Fuel Cells 5 (2005) 187–200. https://doi.org/10.1002/fuce.200400045.
[109] W. You, K.J.T. Noonan, G.W. Coates, Alkaline-stable anion exchange membranes: A review of synthetic approaches, Prog. Polym. Sci. 100 (2020) 101177. https://doi.org/10.1016/j.progpolymsci.2019.101177.
[110] G. Merle, M. Wessling, K. Nijmeijer, Anion exchange membranes for alkaline fuel cells: A review, J. Membr. Sci. 377 (2011) 1–35. https://doi.org/10.1016/j.memsci.2011.04.043.
[111] K.F.L. Hagesteijn, S. Jiang, B.P. Ladewig, A review of the synthesis and characterization of anion exchange membranes, J. Mater. Sci. 53 (2018) 11131–11150. https://doi.org/10.1007/s10853-018-2409-y.
[112] T.N. Danks, R.C.T. Slade, J.R. Varcoe, Alkaline anion-exchange radiation-grafted membranes for possible electrochemical application in fuel cells, J. Mater. Chem. 13 (2003) 712–721. https://doi.org/10.1039/B212164F.
[113] W.-H. Lee, E.J. Park, J. Han, D.W. Shin, Y.S. Kim, C. Bae, Poly(terphenylene) anion exchange membranes: The effect of backbone structure on morphology and membrane property, ACS Macro Lett. 6 (2017) 566–570. https://doi.org/10.1021/acsmacrolett.7b00148.
[114] N. Chen, C. Long, Y. Li, C. Lu, H. Zhu, Ultrastable and high ion-conducting polyelectrolyte based on six-membered N-spirocyclic ammonium for hydroxide exchange membrane fuel cell applications, ACS Appl. Mater. Interfaces 10 (2018) 15720–15732. https://doi.org/10.1021/acsami.8b02884.
[115] B. Bauer, H. Strathmann, F. Effenberger, Anion-exchange membranes with improved alkaline stability, Desalination 79 (1990) 125–144. https://doi.org/10.1016/0011-9164(90)85002-R.
[116] B. Zhang, R.B. Kaspar, S. Gu, J. Wang, Z. Zhuang, Y. Yan, A new alkali-stable phosphonium cation based on fundamental understanding of degradation mechanisms, ChemSusChem 9 (2016) 2374–2379. https://doi.org/10.1002/cssc.201600468.
[117] M.T. Kwasny, G.N. Tew, Expanding metal cation options in polymeric anion exchange membranes, J. Mater. Chem. A 5 (2017) 1400–1405. https://doi.org/10.1039/C6TA07990C.
[118] Q. Wei, X. Cao, P. Veh, A. Konovalova, P. Mardle, P. Overton, S. Cassegrain, S. Vierrath, M. Breitwieser, S. Holdcroft, On the stability of anion exchange memb-

rane fuel cells incorporating polyimidazolium ionene (Aemion+®) membranes and ionomers, Sustain. Energy Fuels 6 (2022) 3551–3564. https://doi.org/10.1039/D2SE00690A.
[119] P. Song, Y. Zhang, J. Pan, L. Zhuang, W. Xu, Cheap carbon black-based high-performance electrocatalysts for oxygen reduction reaction, Chem. Commun. 51 (2015) 1972–1975. https://doi.org/10.1039/C4CC07677J.
[120] H. Ren, Y. Wang, Y. Yang, X. Tang, Y. Peng, H. Peng, L. Xiao, J. Lu, H.D. Abruña, L. Zhuang, Fe/N/C nanotubes with atomic Fe sites: A highly active cathode catalyst for alkaline polymer electrolyte fuel cells, ACS Catal. 7 (2017) 6485–6492. https://doi.org/10.1021/acscatal.7b02340.
[121] K. Khan, A.K. Tareen, M. Aslam, Q. Khan, S.A. Khan, Q.U. Khan, A.S. Saleemi, R. Wang, Y. Zhang, Z. Guo, H. Zhang, Z. Ouyang, Novel two-dimensional carbon–chromium nitride-based composite as an electrocatalyst for oxygen reduction reaction, Front. Chem. 7 (2019). https://doi.org/10.3389/fchem.2019.00738.
[122] J. Lilloja, E. Kibena-Põldsepp, A. Sarapuu, J.C. Douglin, M. Käärik, J. Kozlova, P. Paiste, A. Kikas, J. Aruväli, J. Leis, V. Sammelselg, D.R. Dekel, K. Tammeveski, Transition-metal- and nitrogen-doped carbide-derived carbon/carbon nanotube composites as cathode catalysts for anion-exchange membrane fuel cells, ACS Catal. 11 (2021) 1920–1931. https://doi.org/10.1021/acscatal.0c03511.
[123] K. Kisand, A. Sarapuu, D. Danilian, A. Kikas, V. Kisand, M. Rähn, A. Treshchalov, M. Käärik, M. Merisalu, P. Paiste, J. Aruväli, J. Leis, V. Sammelselg, S. Holdcroft, K. Tammeveski, Transition metal-containing nitrogen-doped nanocarbon catalysts derived from 5-methylresorcinol for anion exchange membrane fuel cell application, J. Colloid Interface Sci. 584 (2021) 263–274. https://doi.org/10.1016/j.jcis.2020.09.114.
[124] L. Osmieri, C. Zafferoni, L. Wang, A.H.A. Monteverde Videla, A. Lavacchi, S. Specchia, Polypyrrole-Derived Fe−Co−N−C catalyst for the oxygen reduction reaction: performance in alkaline hydrogen and ethanol fuel cells, ChemElectroChem 5 (2018) 1954–1965. https://doi.org/10.1002/celc.201800420.
[125] W. Zhu, Y. Pei, J.C. Douglin, J. Zhang, H. Zhao, J. Xue, Q. Wang, R. Li, Y. Qin, Y. Yin, D.R. Dekel, M.D. Guiver, Multi-scale study on bifunctional Co/Fe–N–C cathode catalyst layers with high active site density for the oxygen reduction reaction, Appl. Catal. B Environ. 299 (2021) 120656. https://doi.org/10.1016/j.apcatb.2021.120656.
[126] J. Lilloja, E. Kibena-Põldsepp, A. Sarapuu, M. Käärik, J. Kozlova, P. Paiste, A. Kikas, A. Treshchalov, J. Leis, A. Tamm, V. Kisand, S. Holdcroft, K. Tammeveski, Transition metal and nitrogen-doped mesoporous carbons as cathode catalysts for anion-exchange membrane fuel cells, Appl. Catal. B Environ. 306 (2022) 121113. https://doi.org/10.1016/j.apcatb.2022.121113.
[127] J.G. Kim, J. Cho, S. Han, H. Lee, E. Yuk, B. Bae, S.S. Jang, C. Pak, Boosting activity toward oxygen reduction reaction of a mesoporous FeCuNC catalyst via heteroatom doping-induced electronic state modulation, J. Mater. Chem. A 10 (2022) 5361–5372. https://doi.org/10.1039/D1TA07264A.
[128] S. Hanif, N. Iqbal, X. Shi, T. Noor, G. Ali, A.M. Kannan, NiCo–N-doped carbon nanotubes based cathode catalyst for alkaline membrane fuel cell, Renew. Energy 154 (2020) 508–516. https://doi.org/10.1016/j.renene.2020.03.060.
[129] M. Wang, H. Zhang, G. Thirunavukkarasu, I. Salam, J.R. Varcoe, P. Mardle, X. Li, S. Mu, S. Du, Ionic Liquid-Modified Microporous ZnCoNC-Based Electro-

catalysts for Polymer Electrolyte Fuel Cells, ACS Energy Lett. 4 (2019) 2104–2110. https://doi.org/10.1021/acsenergylett.9b01407.
[130] J. Lilloja, M. Mooste, E. Kibena-Põldsepp, A. Sarapuu, B. Zulevi, A. Kikas, H.-M. Piirsoo, A. Tamm, V. Kisand, S. Holdcroft, A. Serov, K. Tammeveski, Mesoporous iron-nitrogen co-doped carbon material as cathode catalyst for the anion exchange membrane fuel cell, J. Power Sources Adv. 8 (2021) 100052. https://doi.org/10.1016/j.powera.2021.100052.
[131] R. Praats, M. Käärik, A. Kikas, V. Kisand, J. Aruväli, P. Paiste, M. Merisalu, A. Sarapuu, J. Leis, V. Sammelselg, J.C. Douglin, D.R. Dekel, K. Tammeveski, Electroreduction of oxygen on cobalt phthalocyanine-modified carbide-derived carbon/carbon nanotube composite catalysts, J. Solid State Electrochem. 25 (2021) 57–71. https://doi.org/10.1007/s10008-020-04543-z.
[132] J. Lilloja, E. Kibena-Põldsepp, A. Sarapuu, M. Kodali, Y. Chen, T. Asset, M. Käärik, M. Merisalu, P. Paiste, J. Aruväli, A. Treshchalov, M. Rähn, J. Leis, V. Sammelselg, S. Holdcroft, P. Atanassov, K. Tammeveski, Cathode catalysts based on cobalt- and nitrogen-doped nanocarbon composites for anion exchange membrane fuel cells, ACS Appl. Energy Mater. 3 (2020) 5375–5384. https://doi.org/10.1021/acsaem.0c00381.
[133] R. Praats, M. Käärik, A. Kikas, V. Kisand, J. Aruväli, P. Paiste, M. Merisalu, J. Leis, V. Sammelselg, J.H. Zagal, S. Holdcroft, N. Nakashima, K. Tammeveski, Electrocatalytic oxygen reduction reaction on iron phthalocyanine-modified carbide-derived carbon/carbon nanotube composite electrocatalysts, Electrochim. Acta 334 (2020) 135575. https://doi.org/10.1016/j.electacta.2019.135575.
[134] H. Adabi, P.G. Santori, A. Shakouri, X. Peng, K. Yassin, I.G. Rasin, S. Brandon, D.R. Dekel, N.U. Hassan, M.-T. Sougrati, A. Zitolo, J.R. Varcoe, J.R. Regalbuto, F. Jaouen, W.E. Mustain, Understanding how single-atom site density drives the performance and durability of PGM-free Fe–N–C cathodes in anion exchange membrane fuel cells, Mater. Today Adv. 12 (2021) 100179. https://doi.org/10.1016/j.mtadv.2021.100179.
[135] Q. He, L. Zeng, J. Wang, J. Jiang, L. Zhang, J. Wang, W. Ding, Z. Wei, Polymer-coating-induced synthesis of FeN_x enriched carbon nanotubes as cathode that exceeds 1.0 W cm^{-2} peak power in both proton and anion exchange membrane fuel cells, J. Power Sources 489 (2021) 229499. https://doi.org/10.1016/j.jpowsour.2021.229499.
[136] Z. Xiao, P. Sun, Z. Qiao, K. Qiao, H. Xu, S. Wang, D. Cao, Atomically dispersed Fe-Cu dual-site catalysts synergistically boosting oxygen reduction for hydrogen fuel cells, Chem. Eng. J. 446 (2022) 137112. https://doi.org/10.1016/j.cej.2022.137112.
[137] S. Park, M. Her, H. Shin, W. Hwang, Y.-E. Sung, Maximizing the active site densities of single-atomic Fe–N–C electrocatalysts for high-performance anion membrane fuel cells, ACS Appl. Energy Mater. 4 (2021) 1459–1466. https://doi.org/10.1021/acsaem.0c02650.
[138] J.Y. Jung, J.-H. Jang, J.-G. Kim, K.-S. Lee, H.-K. Lim, P. Kim, R.P.H. Chang, J.-W. Park, S.J. Yoo, N.D. Kim, Flash bottom-up arc synthesis of nanocarbons as a universal route for fabricating single-atom electrocatalysts, Small Methods 5 (2021) 2100239. https://doi.org/10.1002/smtd.202100239.
[139] Z. Jiang, X. Liu, X.-Z. Liu, S. Huang, Y. Liu, Z.-C. Yao, Y. Zhang, Q.-H. Zhang, L. Gu, L.-R. Zheng, L. Li, J. Zhang, Y. Fan, T. Tang, Z. Zhuang, J.-S. Hu, Interfacial

assembly of binary atomic metal-N_x sites for high-performance energy devices, Nat. Commun. 14 (2023) 1822. https://doi.org/10.1038/s41467-023-37529-2.
[140] S. Huang, Z. Qiao, P. Sun, K. Qiao, K. Pei, L. Yang, H. Xu, S. Wang, Y. Huang, Y. Yan, D. Cao, The strain induced synergistic catalysis of FeN_4 and MnN_3 dual-site catalysts for oxygen reduction in proton- /anion- exchange membrane fuel cells, Appl. Catal. B Environ. 317 (2022) 121770. https://doi.org/10.1016/j.apcatb.2022.121770.
[141] A. Friedman, M. Mizrahi, N. Levy, N. Zion, M. Zachman, L. Elbaz, Application of molecular catalysts for the oxygen reduction reaction in alkaline fuel cells, ACS Appl. Mater. Interfaces 13 (2021) 58532–58538. https://doi.org/10.1021/acsami.1c16311.
[142] R. Zeng, Y. Yang, X. Feng, H. Li, L.M. Gibbs, F.J. DiSalvo, H.D. Abruña, Non-precious transition metal nitrides as efficient oxygen reduction electrocatalysts for alkaline fuel cells, Sci. Adv. 8 (2022) eabj1584. https://doi.org/10.1126/sciadv.abj1584.
[143] X. Huang, X. Zhang, W. Hu, S. Lv, Y. Huang, Altering the MOF-74 derivatives for efficient oxygen electrocatalysis through synergistic multi-metals and nitrogen modification, J. Mater. Sci. 55 (2020) 10773–10784. https://doi.org/10.1007/s10853-020-04698-0.
[144] X. Peng, V. Kashyap, B. Ng, S. Kurungot, L. Wang, J.R. Varcoe, W.E. Mustain, High-performing PGM-free AEMFC cathodes from carbon-supported cobalt ferrite nanoparticles, Catalysts 9 (2019) 264. https://doi.org/10.3390/ catal9030264.
[145] L. Chai, Z. Hu, X. Wang, L. Zhang, T.-T. Li, Y. Hu, J. Pan, J. Qian, S. Huang, Fe_7C_3 nanoparticles with in situ grown CNT on nitrogen doped hollow carbon cube with greatly enhanced conductivity and ORR performance for alkaline fuel cell, Carbon 174 (2021) 531–539. https://doi.org/10.1016/j.carbon.2020.12.070.
[146] Z.-W. Chang, F.-L. Meng, H.-X. Zhong, X.-B. Zhang, Anchoring iron-EDTA complex on graphene toward the synthesis of highly efficient Fe-N-C oxygen reduction electrocatalyst for fuel cells, Chin. J. Chem. 36 (2018) 287–292. https://doi.org/10.1002/cjoc.201700752.
[147] A. Carlson, P. Shapturenka, B. Eriksson, G. Lindbergh, C. Lagergren, R. Wreland Lindström, Electrode parameters and operating conditions influencing the performance of anion exchange membrane fuel cells, Electrochim. Acta 277 (2018) 151–160. https://doi.org/10.1016/j.electacta.2018.04.137.
[148] F. Gao, Y. Zhang, Z. Wu, H. You, Y. Du, Universal strategies to multi-dimensional noble-metal-based catalysts for electrocatalysis, Coord. Chem. Rev. 436 (2021) 213825. https://doi.org/10.1016/j.ccr.2021.213825.
[149] H. Chang, L.-N. Shi, Y.-H. Chen, P.-F. Wang, T.-F. Yi, Advanced MOF-derived carbon-based non-noble metal oxygen electrocatalyst for next-generation rechargeable Zn-air batteries, Coord. Chem. Rev. 473 (2022) 214839. https://doi.org/10.1016/j.ccr.2022.214839.
[150] M. Mechili, C. Vaitsis, N. Argirusis, P.K. Pandis, G. Sourkouni, C. Argirusis, Research progress in transition metal oxide based bifunctional electrocatalysts for aqueous electrically rechargeable zinc-air batteries, Renew. Sustain. Energy Rev. 156 (2022) 111970. https://doi.org/10.1016/j.rser.2021.111970.
[151] J. Liu, Z. Luo, D. Qian, L. Peng, D. Sun-Waterhouse, G.I.N. Waterhouse, electronic tuning of core–shell CoNi nanoalloy/N-doped few-layer graphene for efficient oxygen electrocatalysis in rechargeable zinc–air batteries, J. Phys. Chem. Lett. 13 (2022) 6743–6748. https://doi.org/10.1021/acs.jpclett.2c01687.

[152] B. Wang, G. Li, High performance bifunctional electrocatalysts designed based on transition-metal sulfides for rechargeable Zn–air batteries, Chem. Eur. J. 28 (2022) e202202062. https://doi.org/10.1002/chem.202202062.
[153] H. Liu, J. Guan, S. Yang, Y. Yu, R. Shao, Z. Zhang, M. Dou, F. Wang, Q. Xu, Metal–organic-framework-derived Co_2P nanoparticle/multi-doped porous carbon as a trifunctional electrocatalyst, Adv. Mater. 32 (2020) 2003649. https://doi.org/10.1002/adma.202003649.
[154] Q. Zhou, Z. Zhang, J. Cai, B. Liu, Y. Zhang, X. Gong, X. Sui, A. Yu, L. Zhao, Z. Wang, Z. Chen, Template-guided synthesis of Co nanoparticles embedded in hollow nitrogen doped carbon tubes as a highly efficient catalyst for rechargeable Zn-air batteries, Nano Energy 71 (2020) 104592. https://doi.org/10.1016/j.nanoen.2020.104592.
[155] L. Yan, Y. Xu, P. Chen, S. Zhang, H. Jiang, L. Yang, Y. Wang, L. Zhang, J. Shen, X. Zhao, L. Wang, A freestanding 3D heterostructure film stitched by MOF-derived carbon nanotube microsphere superstructure and reduced graphene oxide sheets: A superior multifunctional electrode for overall water splitting and Zn–air batteries, Adv. Mater. 32 (2020) 2003313. https://doi.org/10.1002/adma.202003313.
[156] X. Wang, Z. Liao, Y. Fu, C. Neumann, A. Turchanin, G. Nam, E. Zschech, J. Cho, J. Zhang, X. Feng, Confined growth of porous nitrogen-doped cobalt oxide nanoarrays as bifunctional oxygen electrocatalysts for rechargeable zinc–air batteries, Energy Storage Mater. 26 (2020) 157–164. https://doi.org/10.1016/j.ensm.2019.12.043.
[157] J. Liu, C. Wang, H. Sun, H. Wang, F. Rong, L. He, Y. Lou, S. Zhang, Z. Zhang, M. Du, CoO_x/CoN_y nanoparticles encapsulated carbon-nitride nanosheets as an efficiently trifunctional electrocatalyst for overall water splitting and Zn-air battery, Appl. Catal. B Environ. 279 (2020) 119407. https://doi.org/10.1016/j.apcatb.2020.119407.
[158] M. Wang, S. Ji, H. Wang, X. Wang, V. Linkov, R. Wang, Foamed carbon-supported nickel-iron oxides interspersed with bamboo-like carbon nanotubes for high-performance rechargeable zinc-air batteries, Small 18 (2022) 2204474. https://doi.org/10.1002/smll.202204474.
[159] X. Hao, Z. Jiang, B. Zhang, X. Tian, C. Song, L. Wang, T. Maiyalagan, X. Hao, Z.-J. Jiang, N-doped carbon nanotubes derived from graphene oxide with embedment of FeCo nanoparticles as bifunctional air electrode for rechargeable liquid and flexible all-solid-state zinc–air batteries, Adv. Sci. 8 (2021) 2004572. https://doi.org/10.1002/advs.202004572.
[160] D. Lyu, S. Yao, A. Ali, Z.Q. Tian, P. Tsiakaras, P.K. Shen, N, S codoped carbon matrix-encapsulated Co_9S_8 nanoparticles as a highly efficient and durable bifunctional oxygen redox electrocatalyst for rechargeable Zn–air batteries, Adv. Energy Mater. 11 (2021) 2101249. https://doi.org/10.1002/aenm.202101249.
[161] Z. Zhang, X. Zhao, S. Xi, L. Zhang, Z. Chen, Z. Zeng, M. Huang, H. Yang, B. Liu, S.J. Pennycook, P. Chen, Atomically dispersed cobalt trifunctional electrocatalysts with tailored coordination environment for flexible rechargeable Zn–air battery and self-driven water splitting, Adv. Energy Mater. 10 (2020) 2002896. https://doi.org/10.1002/aenm.202002896.
[162] S. Ramakrishnan, J. Balamurugan, M. Vinothkannan, A.R. Kim, S. Sengodan, D.J. Yoo, Nitrogen-doped graphene encapsulated FeCoMoS nanoparticles as advanced trifunctional catalyst for water splitting devices and zinc–air batteries,

Appl. Catal. B Environ. 279 (2020) 119381. https://doi.org/10.1016/j.apcatb.2020.119381.
[163] N.K. Wagh, S.S. Shinde, C.H. Lee, J.-Y. Jung, D.-H. Kim, S.-H. Kim, C. Lin, S.U. Lee, J.-H. Lee, Densely colonized isolated Cu-N single sites for efficient bifunctional electrocatalysts and rechargeable advanced Zn-air batteries, Appl. Catal. B Environ. 268 (2020) 118746. https://doi.org/10.1016/j.apcatb.2020.118746.
[164] S. Ramakrishnan, D.B. Velusamy, S. Sengodan, G. Nagaraju, D.H. Kim, A.R. Kim, D.J. Yoo, Rational design of multifunctional electrocatalyst: An approach towards efficient overall water splitting and rechargeable flexible solid-state zinc–air battery, Appl. Catal. B Environ. 300 (2022) 120752. https://doi.org/10.1016/j.apcatb.2021.120752.
[165] C.-X. Zhao, J.-N. Liu, B.-Q. Li, D. Ren, X. Chen, J. Yu, Q. Zhang, Multiscale Construction of Bifunctional Electrocatalysts for Long-Lifespan Rechargeable Zinc–Air Batteries, Adv. Funct. Mater. 30 (2020) 2003619. https://doi.org/10.1002/adfm.202003619.
[166] T.T. Nguyen, J. Balamurugan, K.-T. Lau, N.H. Kim, J.H. Lee, Novel cobalt-doped molybdenum oxynitride quantum dot@N-doped carbon nanosheets with abundant oxygen vacancies for long-life rechargeable zinc–air batteries, J. Mater. Chem. A 9 (2021) 9092–9104. https://doi.org/10.1039/D0TA12414A.
[167] Y. Jiang, Y.-P. Deng, R. Liang, N. Chen, G. King, A. Yu, Z. Chen, Linker-Compensated metal–organic framework with electron delocalized metal sites for bifunctional oxygen electrocatalysis, J. Am. Chem. Soc. 144 (2022) 4783–4791. https://doi.org/10.1021/jacs.1c10295.
[168] G. Janani, S. Surendran, H. Choi, M.-K. Han, U. Sim, In situ grown $CoMn_2O_4$ 3D-tetragons on carbon cloth: Flexible electrodes for efficient rechargeable zinc–air battery powered water splitting systems, Small 17 (2021) 2103613. https://doi.org/10.1002/smll.202103613.
[169] Y. Go, K. Min, H. An, K. Kim, S. Eun Shim, S.-H. Baeck, Oxygen-vacancy-rich $CoFe/CoFe_2O_4$ embedded in N-doped hollow carbon spheres as a highly efficient bifunctional electrocatalyst for Zn–air batteries, Chem. Eng. J. 448 (2022) 137665. https://doi.org/10.1016/j.cej.2022.137665.
[170] L. Yan, Z. Xu, W. Hu, J. Ning, Y. Zhong, Y. Hu, Formation of sandwiched leaf-like CNTs-Co/$ZnCo_2O_4$@NC-CNTs nanohybrids for high-power-density rechargeable Zn-air batteries, Nano Energy 82 (2021) 105710. https://doi.org/10.1016/j.nanoen.2020.105710.
[171] J.H. Hong, G.D. Park, Y.C. Kang, Aerosol-assisted synthesis of bimetallic nanoparticle-loaded bamboo-like N-doped carbon nanotubes as an efficient bifunctional oxygen catalyst for Zn-air batteries, Int. J. Energy Res. 46 (2022) 5215–5225. https://doi.org/10.1002/er.7513.
[172] L. Yan, H. Wang, J. Shen, J. Ning, Y. Zhong, Y. Hu, Formation of mesoporous Co/CoS/Metal-N-C@S, N-codoped hairy carbon polyhedrons as an efficient trifunctional electrocatalyst for Zn-air batteries and water splitting, Chem. Eng. J. 403 (2021) 126385. https://doi.org/10.1016/j.cej.2020.126385.
[173] A. Wang, C. Zhao, M. Yu, W. Wang, Trifunctional Co nanoparticle confined in defect-rich nitrogen-doped graphene for rechargeable Zn-air battery with a long lifetime, Appl. Catal. B Environ. 281 (2021) 119514. https://doi.org/10.1016/j.apcatb.2020.119514.

[174] F. Luo, J. Zhu, S. Ma, M. Li, R. Xu, Q. Zhang, Z. Yang, K. Qu, W. Cai, Z. Chen, Regulated coordination environment of Ni single atom catalyst toward high-efficiency oxygen electrocatalysis for rechargeable Zinc-air batteries, Energy Storage Mater. 35 (2021) 723–730. https://doi.org/10.1016/j.ensm.2020.12.006.
[175] N.-F. Yu, C. Wu, W. Huang, Y.-H. Chen, D.-Q. Ruan, K.-L. Bao, H. Chen, Y. Zhang, Y. Zhu, Q.-H. Huang, W.-H. Lai, Y.-X. Wang, H.-G. Liao, S.-G. Sun, Y.-P. Wu, J. Wang, Highly efficient Co_3O_4/Co@NCs bifunctional oxygen electrocatalysts for long life rechargeable Zn-air batteries, Nano Energy 77 (2020) 105200. https://doi.org/10.1016/j.nanoen.2020.105200.
[176] Z. Lei, Y. Tan, Z. Zhang, W. Wu, N. Cheng, R. Chen, S. Mu, X. Sun, Defects enriched hollow porous Co-N-doped carbons embedded with ultrafine CoFe/Co nanoparticles as bifunctional oxygen electrocatalyst for rechargeable flexible solid zinc-air batteries, Nano Res. 14 (2021) 868–878. https://doi.org/10.1007/s12274-020-3127-8.
[177] T. Liu, J. Mou, Z. Wu, C. Lv, J. Huang, M. Liu, A Facile and Scalable Strategy for Fabrication of Superior Bifunctional Freestanding Air Electrodes for Flexible Zinc–Air Batteries, Adv. Funct. Mater. 30 (2020) 2003407. https://doi.org/10.1002/adfm.202003407.
[178] G. Yang, J. Zhu, P. Yuan, Y. Hu, G. Qu, B.-A. Lu, X. Xue, H. Yin, W. Cheng, J. Cheng, W. Xu, J. Li, J. Hu, S. Mu, J.-N. Zhang, Regulating Fe-spin state by atomically dispersed Mn-N in Fe-N-C catalysts with high oxygen reduction activity, Nat. Commun. 12 (2021) 1734. https://doi.org/10.1038/s41467-021-21919-5.
[179] J.-T. Ren, L. Chen, Y.-S. Wang, W.-W. Tian, L.-J. Gao, Z.-Y. Yuan, FeNi nanoalloys encapsulated in N-Doped CNTs tangled with N-doped carbon nanosheets as efficient multifunctional catalysts for overall water splitting and rechargeable Zn–air batteries, ACS Sustain. Chem. Eng. 8 (2020) 223–237. https://doi.org/10.1021/acssuschemeng.9b05238.
[180] Z. Pei, Z. Yuan, C. Wang, S. Zhao, J. Fei, L. Wei, J. Chen, C. Wang, R. Qi, Z. Liu, Y. Chen, A Flexible rechargeable zinc–air battery with excellent low-temperature adaptability, Angew. Chem. Int. Ed. 59 (2020) 4793–4799. https://doi.org/10.1002/anie.201915836.
[181] Y. Tan, Z. Zhang, Z. Lei, L. Yu, W. Wu, Z. Wang, N. Cheng, Electronic modulation optimizes OH* intermediate adsorption on Co-Nx-C sites via coupling CoNi alloy in hollow carbon nanopolyhedron toward efficient reversible oxygen electrocatalysis, Appl. Catal. B Environ. 304 (2022) 121006. https://doi.org/10.1016/j.apcatb.2021.121006.
[182] P. Zhu, J. Gao, S. Liu, Facile in situ coupling CoFe/Co nanoparticles and N-doped carbon nanotubes/graphitic nanosheets as bifunctional oxygen electrocatalysts for rechargeable Zn-air batteries, J. Power Sources 449 (2020) 227512. https://doi.org/10.1016/j.jpowsour.2019.227512.
[183] J. Han, H. Bao, J.-Q. Wang, L. Zheng, S. Sun, Z.L. Wang, C. Sun, 3D N-doped ordered mesoporous carbon supported single-atom Fe-N-C catalysts with superior performance for oxygen reduction reaction and zinc-air battery, Appl. Catal. B Environ. 280 (2021) 119411. https://doi.org/10.1016/j.apcatb.2020.119411.
[184] Y. Wu, X. Wu, T. Tu, P. Zhang, J. Li, Y. Zhou, L. Huang, S. Sun, Controlled synthesis of FeN_x-CoN_x dual active sites interfaced with metallic Co nanoparticles as bifunctional oxygen electrocatalysts for rechargeable Zn-air batteries,

Appl. Catal. B Environ. 278 (2020) 119259. https://doi.org/10.1016/j.apcatb.2020.119259.
[185] S. Zhao, Y. Yang, Z. Tang, Insight into Structural Evolution, Active Sites, and Stability of Heterogeneous Electrocatalysts, Angew. Chem. Int. Ed. 61 (2022) e202110186. https://doi.org/10.1002/anie.202110186.
[186] Z.-F. Huang, J. Wang, Y. Peng, C.-Y. Jung, A. Fisher, X. Wang, Design of efficient bifunctional oxygen reduction/evolution electrocatalyst: Recent advances and perspectives, Adv. Energy Mater. 7 (2017) 1700544. https://doi.org/10.1002/aenm.201700544.
[187] K. Zeng, X. Zheng, C. Li, J. Yan, J.-H. Tian, C. Jin, P. Strasser, R. Yang, Recent advances in non-noble bifunctional oxygen electrocatalysts toward large-scale production, Adv. Funct. Mater. 30 (2020) 2000503. https://doi.org/10.1002/adfm.202000503.
[188] S. Gottesfeld, D.R. Dekel, M. Page, C. Bae, Y. Yan, P. Zelenay, Y.S. Kim, Anion exchange membrane fuel cells: Current status and remaining challenges, J. Power Sources 375 (2018) 170–184. https://doi.org/10.1016/j.jpowsour.2017.08.010.
[189] A.G. Wright, J. Fan, B. Britton, T. Weissbach, H.-F. Lee, E.A. Kitching, T.J. Peckham, S. Holdcroft, Hexamethyl-p-terphenyl poly(benzimidazolium): a universal hydroxide-conducting polymer for energy conversion devices, Energy Environ. Sci. 9 (2016) 2130–2142. https://doi.org/10.1039/C6EE00656F.
[190] P. Serp, M. Corrias, P. Kalck, Carbon nanotubes and nanofibers in catalysis, Appl. Catal. Gen. 253 (2003) 337–358. https://doi.org/10.1016/S0926-860X(03)00549-0.
[191] I.V. Stankevich, M.V. Nikerov, D.A. Bochvar, The structural chemistry of crystalline carbon: Geometry, stability, and electronic spectrum, Russ. Chem. Rev. 53 (1984) 640. https://doi.org/10.1070/RC1984v053n07ABEH003084.
[192] M. Thommes, K. Kaneko, A.V. Neimark, J.P. Olivier, F. Rodriguez-Reinoso, J. Rouquerol, K.S.W. Sing, Physisorption of gases, with special reference to the evaluation of surface area and pore size distribution (IUPAC Technical Report), Pure Appl. Chem. 87 (2015) 1051–1069. https://doi.org/10.1515/pac-2014-1117.
[193] S. Kabir, K. Artyushkova, A. Serov, P. Atanassov, Role of nitrogen moieties in N-Doped 3D-graphene nanosheets for oxygen electroreduction in acidic and alkaline media, ACS Appl. Mater. Interfaces 10 (2018) 11623–11632. https://doi.org/10.1021/acsami.7b18651.
[194] A. Moysiadou, X. Hu, Stability profiles of transition metal oxides in the oxygen evolution reaction in alkaline medium, J. Mater. Chem. A 7 (2019) 25865–25877. https://doi.org/10.1039/C9TA10308B.
[195] F. Song, L. Bai, A. Moysiadou, S. Lee, C. Hu, L. Liardet, X. Hu, Transition metal oxides as electrocatalysts for the oxygen evolution reaction in alkaline solutions: An application-inspired renaissance, J. Am. Chem. Soc. 140 (2018) 7748–7759. https://doi.org/10.1021/jacs.8b04546.
[196] C.L.I. Flores, M.D.L. Balela, Electrocatalytic oxygen evolution reaction of hierarchical micro/nanostructured mixed transition cobalt oxide in alkaline medium, J. Solid State Electrochem. 24 (2020) 891–904. https://doi.org/10.1007/s10008-020-04530-4.
[197] H. Osgood, S.V. Devaguptapu, H. Xu, J. Cho, G. Wu, Transition metal (Fe, Co, Ni, and Mn) oxides for oxygen reduction and evolution bifunctional catalysts in alkaline media, Nano Today 11 (2016) 601–625. https://doi.org/10.1016/j.nantod.2016.09.001.

[198] J. Quílez-Bermejo, M. Melle-Franco, E. San-Fabián, E. Morallón, D. Cazorla-Amorós, Towards understanding the active sites for the ORR in N-doped carbon materials through fine-tuning of nitrogen functionalities: an experimental and computational approach, J. Mater. Chem. A 7 (2019) 24239–24250. https://doi.org/10.1039/C9TA07932G.
[199] L. Zhang, Q. Fan, K. Li, S. Zhang, X. Ma, First-row transition metal oxide oxygen evolution electrocatalysts: regulation strategies and mechanistic under standings, Sustain. Energy Fuels 4 (2020) 5417–5432. https://doi.org/10.1039/D0SE01087A.
[200] C. Hu, L. Dai, Carbon-Based Metal-Free Catalysts for Electrocatalysis beyond the ORR, Angew. Chem. Int. Ed. 55 (2016) 11736–11758. https://doi.org/10.1002/anie.201509982.
[201] V. Goellner, V. Armel, A. Zitolo, E. Fonda, F. Jaouen, Degradation by hydrogen peroxide of metal-nitrogen-carbon catalysts for oxygen reduction, J. Electrochem. Soc. 162 (2015) H403. https://doi.org/10.1149/2.1091506jes.
[202] Q. Hu, G. Li, G. Li, X. Liu, B. Zhu, X. Chai, Q. Zhang, J. Liu, C. He, Trifunctional electrocatalysis on dual-doped graphene nanorings–integrated boxes for efficient water splitting and Zn–air batteries, Adv. Energy Mater. 9 (2019) 1803867. https://doi.org/10.1002/aenm.201803867.
[203] Y. Ma, M. Wu, L. Li, Z. Li, X. Zhao, R. Lian, W. Zhang, MOF derived Co_9S_8 nanoparticles embedded in 3D N-doped carbon matrix for high-performance K-ion battery anode, Appl. Surf. Sci. 600 (2022) 154159. https://doi.org/10.1016/j.apsusc.2022.154159.
[204] S.M. Abd El Haleem, E.E. Abd El Aal, Electrochemical behaviour of iron in alkaline sulphide solutions, Corros. Eng. Sci. Technol. 43 (2008) 173–178. https://doi.org/10.1179/174327807X234769.
[205] S. De, J. Zhang, R. Luque, N. Yan, Ni-based bimetallic heterogeneous catalysts for energy and environmental applications, Energy Environ. Sci. 9 (2016) 3314–3347. https://doi.org/10.1039/C6EE02002J.
[206] S. Zheng, X. Li, B. Yan, Q. Hu, Y. Xu, X. Xiao, H. Xue, H. Pang, Transition-metal (Fe, Co, Ni) based metal-organic frameworks for electrochemical energy storage, Adv. Energy Mater. 7 (2017) 1602733. https://doi.org/10.1002/aenm.201602733.
[207] Y. Leng, G. Chen, A.J. Mendoza, T.B. Tighe, M.A. Hickner, C.-Y. Wang, Solid-state water electrolysis with an alkaline membrane, J. Am. Chem. Soc. 134 (2012) 9054–9057. https://doi.org/10.1021/ja302439z.
[208] K. Chen, S. Kim, R. Rajendiran, K. Prabakar, G. Li, Z. Shi, C. Jeong, J. Kang, O.L. Li, Enhancing ORR/OER active sites through lattice distortion of Fe-enriched FeNi3 intermetallic nanoparticles doped N-doped carbon for high-performance rechargeable Zn-air battery, J. Colloid Interface Sci. 582 (2021) 977–990. https://doi.org/10.1016/j.jcis.2020.08.101.
[209] Y. Hu, J.O. Jensen, W. Zhang, L.N. Cleemann, W. Xing, N.J. Bjerrum, Q. Li, Hollow spheres of iron carbide nanoparticles encased in graphitic layers as oxygen reduction catalysts, Angew. Chem. Int. Ed. 53 (2014) 3675–3679. https://doi.org/10.1002/anie.201400358.
[210] Y. Su, H. Jiang, Y. Zhu, X. Yang, J. Shen, W. Zou, J. Chen, C. Li, Enriched graphitic N-doped carbon-supported Fe_3O_4 nanoparticles as efficient electrocatalysts for oxygen reduction reaction, J. Mater. Chem. A 2 (2014) 7281–7287. https://doi.org/10.1039/C4TA00029C.

[211] L. Lai, J.R. Potts, D. Zhan, L. Wang, C.K. Poh, C. Tang, H. Gong, Z. Shen, J. Lin, R.S. Ruoff, Exploration of the active center structure of nitrogen-doped graphene-based catalysts for oxygen reduction reaction, Energy Environ. Sci. 5 (2012) 7936–7942. https://doi.org/10.1039/C2EE21802J.
[212] K. Huang, Y. Sun, Y. Zhang, X. Wang, W. Zhang, S. Feng, Hollow-structured metal oxides as oxygen-related catalysts, Adv. Mater. 31 (2019) 1801430. https://doi.org/10.1002/adma.201801430.
[213] J.H. Zagal, M.T.M. Koper, Reactivity descriptors for the activity of molecular MN_4 catalysts for the oxygen reduction reaction, Angew. Chem. Int. Ed. 55 (2016) 14510–14521. https://doi.org/10.1002/anie.201604311.
[214] M.P. Oyarzún, N. Silva, D. Cortés-Arriagada, J.F. Silva, I.O. Ponce, M. Flores, K. Tammeveski, D. Bélanger, A. Zitolo, F. Jaouen, J.H. Zagal, Enhancing the electrocatalytic activity of Fe phthalocyanines for the oxygen reduction reaction by the presence of axial ligands: Pyridine-functionalized single-walled carbon nanotubes, Electrochim. Acta 398 (2021) 139263. https://doi.org/10.1016/j.electacta.2021.139263.
[215] Y. Ha, B. Fei, X. Yan, H. Xu, Z. Chen, L. Shi, M. Fu, W. Xu, R. Wu, Atomically dispersed Co-pyridinic N-C for superior oxygen reduction reaction, Adv. Energy Mater. 10 (2020) 2002592. https://doi.org/10.1002/aenm.202002592.
[216] G. Wu, A. Santandreu, W. Kellogg, S. Gupta, O. Ogoke, H. Zhang, H.-L. Wang, L. Dai, Carbon nanocomposite catalysts for oxygen reduction and evolution reactions: From nitrogen doping to transition-metal addition, Nano Energy 29 (2016) 83–110. https://doi.org/10.1016/j.nanoen.2015.12.032.
[217] W. Niu, K. Marcus, L. Zhou, Z. Li, L. Shi, K. Liang, Y. Yang, Enhancing electron transfer and electrocatalytic activity on crystalline carbon-conjugated g-C_3N_4, ACS Catal. 8 (2018) 1926–1931. https://doi.org/10.1021/acscatal.8b00026.
[218] L. Yang, N. Huang, C. Luo, H. Yu, P. Sun, X. Lv, X. Sun, Atomically dispersed and nanoscaled Co species embedded in micro-/mesoporous carbon nanosheet/nanotube architecture with enhanced oxygen reduction and evolution bifunction for Zn-Air batteries, Chem. Eng. J. 404 (2021) 127112. https://doi.org/10.1016/j.cej.2020.127112.
[219] I. Matanovic, K. Artyushkova, P. Atanassov, Understanding PGM-free catalysts by linking density functional theory calculations and structural analysis: Perspectives and challenges, Curr. Opin. Electrochem. 9 (2018) 137–144. https://doi.org/10.1016/j.coelec.2018.03.009.
[220] H. Zhang, D. Guan, X. Gao, J. Yu, G. Chen, W. Zhou, Z. Shao, Morphology, crystal structure and electronic state one-step co-tuning strategy towards developing superior perovskite electrocatalysts for water oxidation, J. Mater. Chem. A 7 (2019) 19228–19233. https://doi.org/10.1039/C9TA06020K.
[221] Y. Shen, Y. Zhu, J. Sunarso, D. Guan, B. Liu, H. Liu, W. Zhou, Z. Shao, New phosphorus-doped perovskite oxide as an oxygen reduction reaction electrocatalyst in an alkaline solution, Chem. Eur. J. 24 (2018) 6950–6957. https://doi.org/10.1002/chem.201705675.
[222] J.F. Moulder, Handbook of X-ray Photoelectron Spectroscopy: A Reference Book of Standard Spectra for Identification and Interpretation of XPS Data, Physical Electronics Division, Perkin-Elmer Corporation, 1992.

10. SUMMARY IN ESTONIAN

M-N_4 makrotsüklilised katalüsaatorid hapniku redutseerumis- ja eraldumisreaktsiooni elektrokatalüüsis

Doktoritöö eesmärk on arendada siirdemetallidel põhinevaid bifunktsionaalseid mitte-väärismetallkatalüsaatoreid hapniku redutseerumisreaktsiooni ja hapniku eraldumisreaktsiooni jaoks. Uurimistöö siht oli hinnata nende katalüsaatorite sobivust ja jõudlust anioonvahetusmembraaniga kütuseelementide ja taaslaetavate tsink-õhk akude elektroodimaterjalina. Selle saavutamiseks valmistati siirdemetallide ja lämmastikuga dopeeritud katalüsaatormaterjalid kõrgtemperatuursel pürolüüsil, kasutades selleks metalloftalotsüaniine ja mitmesuguseid süsiniknanomaterjale. Katalüsaatoreid, mis näitasid kõige kõrgemat elektrokatalüütilist aktiivsust, rakendati elektroodimaterjalina anioonvahetusmembraaniga kütuseelementides ja taaslaetavates tsink-õhk akudes. Valmistatud katalüsaatormaterjale karakteriseeriti põhjalikult mitmesuguste füüsikalis-keemiliste meetoditega.

Doktoritöö esimeses osas kasutati pürolüüsimeetodit siirdemetall-lämmastik-süsinik (M-N-C) katalüsaatormaterjalide valmistamiseks. Selle käigus kombineeriti omavahel mitut bimetalset metalloftalotsüaniini (FeNi, FeMn, FeCo, NiCo, MnCo ja MnNi), mis kanti mitmeseinaliste süsiniknanotorude (MWCNT) pinnale, et uurida nende elektrokatalüütilist aktiivsust hapniku redutseerumis- ja eraldumisreaktsiooni protsessides leeliselises lahuses [I,II]. Lämmastikuga koordineeritud metallitsentrite (M-N_x) olemasolu katalüsaatori pinnal, mida kinnitasid röntgenfotoelektronspektroskoopia tulemused, tõstis oluliselt M-N-C materjalide elektrokatalüütilist aktiivsust mõlemas protsessis. FeCoN-MWCNT katalüsaator näitas kõrgeimat aktiivsust elektrokeemilisel hapniku redutseerumisel ja FeNiN-MWCNT oli aktiivseim katalüsaator hapniku eraldumisreaktsioonil [I,II]. Parimad bifunktsionaalsed omadused olid FeCoN-MWCNT, FeNiN-MWCNT ja NiCoN-MWCNT katalüsaatoritel, millel oli peaaegu sama ΔE väärtus [I,II]. FeCoN-MWCNT katalüsaatori kasutamisel katoodimaterjalina saadi kõrge anioonvahetusmembraaniga kütuseelemendi jõudlus (692 mW cm^{-2}) [II], FeNiN-MWCNT materjal käitus anioonvahetusmembraaniga elektrolüüseris võrreldavalt RuO_2 katalüsaatoriga [II] ja NiCoN-MWCNT katalüsaatoril oli arvestatav jõudlus taaslaetavas Zn-õhk akus [I].

Doktoritöö teises osas sünteesiti bimetalseid lämmastikuga dopeeritud süsiniknanomaterjale kasutades raudftalotsüaniini (FePc) ja nikkelftalotsüaniini (NiPc) siirdemetalli ja lämmastiku allikana ning kuut süsinikmaterjali katalüsaatorikandjana, et uurida eri süsiniknanomaterjalide mõju hapniku redutseerumis- ja eraldumisreaktsiooni elektrokatalüüsile [III]. Nendel katalüsaatormaterjalidel oli kõrge bifuntsionaalne elektrokatalüütiline aktiivsus nii hapniku redutseerumiskui ka eraldumisreaktsioonil. Füüsikalis-keemiliste meetoditega tehtud uuringud kinnitasid metalli nanoosakeste, metallioksiidide ja M-N_x tsentrite olemasolu katalüsaatorite pinnal, mida peetakse aktiivtsentriteks hapniku redutseerumis- ja eraldumisreaktsioonile aluselises keskkonnas. Valmistatud katalüsaatoritest näitasid kõrgeimat aktiivsust hapniku elektrokatalüütilisel redutseerumisel suure

grafiitsusega FeNiN-MWCNT ja suure mesopoorsusega FeNiN-MC, millega saadi anioonvahetusmembraaniga kütuseelemendis testimisel maksimaalseks võimsustiheduseks vastavalt 406 ja 386 mW cm^{-2} [III]. Peale selle saadi suur võimsustihedus FeNiN-MWCNT materjaliga Zn-õhk akus (85 mW cm^{-2}). Väärib märkimist, et need katalüsaatormaterjalid osutusid küllaltki stabiilseteks galvanostaatiliste laadimis-tühjenemistsüklite käigus Zn-õhk akus. Saadud tulemused osutavad nende materjalide paljulubavale rakenduspotentsiaalile elektrokeemilistes energiamuundamise seadmetes. Hiljem dopeeriti FePc-ga karbiidset päritolu süsinikmaterjali ja grafeeni komposiiti, et valmistada suure mikro- ja mesopoorsusega katalüsaator, mida kasutati hapniku redutseerumisel happelises keskkonnas. FeN-CDC/G/DCDA katalüsaatormaterjaliga, mille valmistamisel kasutati ditsüaandiamiidi (DCDA) täiendava lämmastikuallikana, saavutati poollainepotentsiaal 0,76 V happelises lahuses, mis osutab kõrgele elektrokatalüütilisele aktiivsusele [IV].

Doktoritöö kolmandas osas valmistati katalüsaatormaterjale polümeeride baasil [V,VI]. Kontrollitud floroglütsinool-formaldehüüd polümeervõrgustiku sünteesimisel saadi mikro-mesopoorse struktuuriga süsinikmaterjale. Koobalti ja lämmastikuga dopeeritud poorsed süsinikmaterjalid saadi floroglütsinooli-formaldehüüdi polümeeri abil lisades lähteainetena ka 2-metüülimidasooli ja koobaltftalotsüaniini (CoPc) [V]. Suurema koobaltisisalduse ja hierarhilise poorse struktuuriga CoN-PC-2 katalüsaator näitas kõrget bifunktsionaalset elektrokatalüütilist aktiivsust hapniku redutseerumis- ja eraldumisreaktsioonil. Nimetatud materjaliga saadi poollainepotentsiaal 0,81 V ja $E_{j=10}$ väärtus 1,70 V vs RHE. Enamgi veel, CoN-PC-2 katalüsaatori kasutamine võimaldas saada suure Zn-õhk aku jõudluse, mida näitas avatud ahela potentsiaal 1,47 V ja maksimaalne võimsustihedus 158 mW cm^{-2}. See aku oli 45 tunni vältel stabiilne [V]. Järgnevalt sünteesiti odaval viisil aatomdispergeeritud metallitsentritega katalüsaatormaterjalid floroglütsinool-ditsüaandiamiid-formaldehüüd polümeervõrgustiku baasil. Aatomdispergeeritud metallitsentritega bimetalsel FeCoN-PDF-T_2-2 katalüsaatoril, mille sünteesil kasutati tsingipõhist matriitsi, oli kõrge elektrokatalüütiline aktiivsus hapniku redutseerumis- ja eraldumisreaktsioonil aluselises keskkonnas ning suurepärane stabiilsus [VI]. See katalüsaatormaterjal näitas madalat ΔE väärtust (0,75 V), mis on võrreldav kommertsiaalse PtRu/C katalüsaatoriga saadud tulemusega. Märkimisväärselt kõrget bifunktsionaalset elektrokatalüütilist aktiivsust seostati kõrgdispergeeritud aktiivtsentritega, mida kinnitasid skaneeriva läbistuselektronmikroskoobi abil tehtud mõõtmised, ning raua ja koobalti vahelise sünergeetilise efektiga. FeCoN-PDF-T_2-2 õhuelektroodiga Zn-õhk aku testimisel saadi suurepärane võimsustihedus (258 mW cm^{-2}), mis ületas PtRu/C katalüsaatoriga saadud väärtuse (185 mW cm^{-2}). Saadud tulemused osutavad sellele, et polümeeridel põhinev bifunktsionaalsete katalüsaatorite hõlpsalt teostatav sünteesimeetod avab uue teeraja aatomdispergeeritud ning stabiilsete elektrokatalüsaatorite väljatöötamiseks, mis võiksid leida laiaulatuslikku rakendust elektrokeemilise energiasalvestuse seadmetes.

Doktoritöö raames tehtud uuringud on seotud väga olulise teemaga, milleks on hapniku redutseerumis- ja eraldumisreaktsiooni katalüsaatorite arendamine

elektrokeemilise energiatehnoloogia seadmetele nagu näiteks kõrge jõudlusega anioonvahetusmembraaniga kütuseelementidele ja tsink-õhk akudele. Saadud tulemused näitavad bifunktsionaalsete M-N-C katalüsaatorite suurt potentsiaali kasutamaks neid eelnimetatud seadmetes. Doktoritöö tulemustest nähtub bimetalliliste M-N-C materjalide kasulikkus, kus raua kombineerimine hapniku eraldumisreaktsiooni jaoks aktiivsete metallidega (Co ja Ni) annab parimaid tulemusi. Samuti rõhutatakse töös eri sünteesimeetodite ja katalüsaatormaterjali struktuuri olulist rolli bifunktsionaalse elektrokatalüütilise aktiivsuse tagamisel. Doktoritöö on andnud väärtusliku panuse mitte-väärismetallkatalüsaatorite arendamisse hapniku redutseerumis- ja eraldumisreaktsiooni tarvis.

11. ACKNOWLEDGEMENTS

I wish to express my deep gratitude to my supervisors, Dr. Elo Kibena-Põldsepp, along with Dr. Srinu Akula and Professor Kaido Tammeveski. Their invaluable assistance, time and scientific guidance have been a constant source of support throughout my PhD studies.

I'd like to extend my sincere appreciation to all the members of our working group for fostering a friendly and collaborative environment. I'm also thankful to the co-authors of our publications, with special recognition to Dr. Jekaterina Kozlova for her SEM, TEM and EDX measurements, Dr. Arvo Kikas for XPS measurements, Dr. Alexey Treshchalov for Raman measurements, Dr. Maike Käärik for BET measurements and Dr. Jaan Aruväli for XRD measurements.

I would like to express my gratitude to our esteemed foreign collaborators, John C. Douglin and Professor Dario R. Dekel from Technion, Israel Institute of Technology, for their invaluable contributions to the AEMFC testing in article [II]. Additionally, I extend my thanks to Professor José-Ramón Galán-Mascarós and co-workers from the Barcelona Institute of Science and Technology for their dedicated efforts in conducting the electrolyser testing detailed in [II]. Special appreciation goes to Professor Steven Holdcroft from Simon Fraser University for generously providing the anion-exchange membrane for fuel cell testing. Furthermore, I would like to express my appreciation to Professor José H. Zagal from the University of Santiago de Chile.

Furthermore, I want to acknowledge my family and friends for their unwavering support and motivation. A special note of gratitude goes to my parents, Chandra Devi and Basudev Prasad, for their tireless dedication and support throughout my studies and for believing in me. I am also profoundly thankful to my brothers, Chetan and Chandrapal, for their enduring patience and support throughout my life.

My research work was financially supported by EU though the European Regional Development Fund (TK141 “Advanced materials and high technology devices for energy recuperation systems”) and by Estonian Research Council (grant PRG723).

PUBLICATIONS

CURRICULUM VITAE

Name: Yogesh Kumar
Date of birth: February 18, 1997
Citizenship: Indian
Address: Ravila 14a, 50411 Tartu, Estonia
E-mail: yogeshkum.397@gmail.com

Education:

2019–…	University of Tartu, Faculty of Science and Technology, PhD studies, Chemistry
2014–2019	Indian Institute of Science Education and Research Bhopal, Institute of Chemistry, BSc-MSc Dual Degree

Professional experience:

2021–…	University of Tartu, Institute of Chemistry, chemist

Major scientific publications:

1. **Kumar, Y.,** Kibena-Põldsepp, E., Kozlova, J., Rähn, M., Treshchalov, A., Kikas, A., Kisand, V., Aruväli, J., Tamm, A., Douglin, J.C., Folkman, S.J., Gelmetti, I., Garcés-Pineda, F.A., Galán-Mascarós, J.R., Dekel, D.R., Tammeveski, K. Bifunctional oxygen electrocatalysis on mixed metal phthalocyanine-modified carbon nanotubes prepared via pyrolysis. ACS Applied Materials & Interfaces 13 (2021) 41507−41516.
2. **Kumar, Y.**, Kibena-Põldsepp, E., Kozlova, J., Kikas, A., Käärik, M., Aruväli, J., Kisand, V., Leis, J., Tamm, A., Tammeveski, K. Bimetal phthalocyanine-modified carbon nanotube-based bifunctional catalysts for zinc-air batteries. ChemElectroChem 8 (2021) 2662−2670.
3. **Kumar, Y.**, Kibena-Põldsepp, E., Mooste, M., Kozlova, J., Kikas, A., Aruväli, J., Käärik, M., Kisand, V., Leis, J., Tamm, A., Holdcroft, S., Zagal, J.H., Tammeveski, K. Iron and nickel phthalocyanine-modified nanocarbon materials as cathode catalysts for anion-exchange membrane fuel cells and zinc-air batteries. ChemElectroChem 9 (2022) e202200717.
4. **Kumar, Y.**, Akula, S., Kibena-Põldsepp, E., Käärik, M., Kozlova, J., Kikas, A., Aruväli, J., Kisand, V., Leis, J., Tamm, A., Tammeveski, K. Cobalt phthalocyanine-doped polymer-based electrocatalyst for rechargeable zinc-air batteries. Materials 16 (2023) ARTN 5105.
5. **Kumar, Y.**, Mooste, M., Tammeveski, K. Recent progress of transition metal-based bifunctional electrocatalysts for rechargeable zinc–air battery application. Current Opinion in Electrochemistry 38 (2023) 101229.
6. **Kumar, Y.**, Kibena-Põldsepp, E., Akula, S., Kozlova, J., Kikas, A., Aruväli, J., Kisand, V., Kukli, K., Tammeveski, K. The effect of additional nitrogen source on iron phthalocyanine-based catalysts for oxygen reduction reaction in acidic media. *Electrochemistry Communications* (2023, accepted).

ELULOOKIRJELDUS

Nimi: Yogesh Kumar
Sünniaeg: 18. veebruar 1997
Kodakondsus: India
Aadress: Ravila 14a, 50411 Tartu, Eesti
E-post: yogeshkum.397@gmail.com

Hariduskäik:

2019–…	Tartu Ülikool, Loodus- ja täppisteaduste valdkond, doktoriõpingud, keemia
2014–2019	Teadushariduse ja Uuringute India Instituut Bhopalis (India), Keemia Instituut, bakalaureuse- ja magistrikraad

Töökogemus:

2021–…	Tartu Ülikool, Keemia instituut, keemik

Publikatsioonide loetelu:

1. **Kumar, Y.,** Kibena-Põldsepp, E., Kozlova, J., Rähn, M., Treshchalov, A., Kikas, A., Kisand, V., Aruväli, J., Tamm, A., Douglin, J.C., Folkman, S.J., Gelmetti, I., Garcés-Pineda, F.A., Galán-Mascarós, J.R., Dekel, D.R., Tammeveski, K. Bifunctional oxygen electrocatalysis on mixed metal phthalocyanine-modified carbon nanotubes prepared via pyrolysis. ACS Applied Materials & Interfaces 13 (2021) 41507−41516.
2. **Kumar, Y.**, Kibena-Põldsepp, E., Kozlova, J., Kikas, A., Käärik, M., Aruväli, J., Kisand, V., Leis, J., Tamm, A., Tammeveski, K. Bimetal phthalocyanine-modified carbon nanotube-based bifunctional catalysts for zinc-air batteries. ChemElectroChem 8 (2021) 2662−2670.
3. **Kumar, Y.**, Kibena-Põldsepp, E., Mooste, M., Kozlova, J., Kikas, A., Aruväli, J., Käärik, M., Kisand, V., Leis, J., Tamm, A., Holdcroft, S., Zagal, J.H., Tammeveski, K. Iron and nickel phthalocyanine-modified nanocarbon materials as cathode catalysts for anion-exchange membrane fuel cells and zinc-air batteries. ChemElectroChem 9 (2022) e202200717.
4. **Kumar, Y.**, Akula, S., Kibena-Põldsepp, E., Käärik, M., Kozlova, J., Kikas, A., Aruväli, J., Kisand, V., Leis, J., Tamm, A., Tammeveski, K. Cobalt phthalocyanine-doped polymer-based electrocatalyst for rechargeable zinc-air batteries. Materials 16 (2023) ARTN 5105.
5. **Kumar, Y.**, Mooste, M., Tammeveski, K. Recent progress of transition metal-based bifunctional electrocatalysts for rechargeable zinc–air battery application. Current Opinion in Electrochemistry 38 (2023) 101229.
6. **Kumar, Y.**, Kibena-Põldsepp, E., Akula, S., Kozlova, J., Kikas, A., Aruväli, J., Kisand, V., Kukli, K., Tammeveski, K. The effect of additional nitrogen source on iron phthalocyanine-based catalysts for oxygen reduction reaction in acidic media. *Electrochemistry Communications* (2023, accepted).

DISSERTATIONES CHIMICAE UNIVERSITATIS TARTUENSIS

1. **Toomas Tamm.** Quantum-chemical simulation of solvent effects. Tartu, 1993, 110 p.
2. **Peeter Burk.** Theoretical study of gas-phase acid-base equilibria. Tartu, 1994, 96 p.
3. **Victor Lobanov.** Quantitative structure-property relationships in large descriptor spaces. Tartu, 1995, 135 p.
4. **Vahur Mäemets.** The ^{17}O and ^{1}H nuclear magnetic resonance study of H_2O in individual solvents and its charged clusters in aqueous solutions of electrolytes. Tartu, 1997, 140 p.
5. **Andrus Metsala.** Microcanonical rate constant in nonequilibrium distribution of vibrational energy and in restricted intramolecular vibrational energy redistribution on the basis of slater's theory of unimolecular reactions. Tartu, 1997, 150 p.
6. **Uko Maran.** Quantum-mechanical study of potential energy surfaces in different environments. Tartu, 1997, 137 p.
7. **Alar Jänes.** Adsorption of organic compounds on antimony, bismuth and cadmium electrodes. Tartu, 1998, 219 p.
8. **Kaido Tammeveski.** Oxygen electroreduction on thin platinum films and the electrochemical detection of superoxide anion. Tartu, 1998, 139 p.
9. **Ivo Leito.** Studies of Brønsted acid-base equilibria in water and non-aqueous media. Tartu, 1998, 101 p.
10. **Jaan Leis.** Conformational dynamics and equilibria in amides. Tartu, 1998, 131 p.
11. **Toonika Rinken.** The modelling of amperometric biosensors based on oxidoreductases. Tartu, 2000, 108 p.
12. **Dmitri Panov.** Partially solvated Grignard reagents. Tartu, 2000, 64 p.
13. **Kaja Orupõld.** Treatment and analysis of phenolic wastewater with microorganisms. Tartu, 2000, 123 p.
14. **Jüri Ivask.** Ion Chromatographic determination of major anions and cations in polar ice core. Tartu, 2000, 85 p.
15. **Lauri Vares.** Stereoselective Synthesis of Tetrahydrofuran and Tetrahydropyran Derivatives by Use of Asymmetric Horner-Wadsworth-Emmons and Ring Closure Reactions. Tartu, 2000, 184 p.
16. **Martin Lepiku.** Kinetic aspects of dopamine D_2 receptor interactions with specific ligands. Tartu, 2000, 81 p.
17. **Katrin Sak.** Some aspects of ligand specificity of P2Y receptors. Tartu, 2000, 106 p.
18. **Vello Pällin.** The role of solvation in the formation of iotsitch complexes. Tartu, 2001, 95 p.
19. **Katrin Kollist.** Interactions between polycyclic aromatic compounds and humic substances. Tartu, 2001, 93 p.

20. **Ivar Koppel.** Quantum chemical study of acidity of strong and superstrong Brønsted acids. Tartu, 2001, 104 p.
21. **Viljar Pihl.** The study of the substituent and solvent effects on the acidity of OH and CH acids. Tartu, 2001, 132 p.
22. **Natalia Palm.** Specification of the minimum, sufficient and significant set of descriptors for general description of solvent effects. Tartu, 2001, 134 p.
23. **Sulev Sild.** QSPR/QSAR approaches for complex molecular systems. Tartu, 2001, 134 p.
24. **Ruslan Petrukhin.** Industrial applications of the quantitative structure-property relationships. Tartu, 2001, 162 p.
25. **Boris V. Rogovoy.** Synthesis of (benzotriazolyl)carboximidamides and their application in relations with *N*- and *S*-nucleophyles. Tartu, 2002, 84 p.
26. **Koit Herodes.** Solvent effects on UV-vis absorption spectra of some solvatochromic substances in binary solvent mixtures: the preferential solvation model. Tartu, 2002, 102 p.
27. **Anti Perkson.** Synthesis and characterisation of nanostructured carbon. Tartu, 2002, 152 p.
28. **Ivari Kaljurand.** Self-consistent acidity scales of neutral and cationic Brønsted acids in acetonitrile and tetrahydrofuran. Tartu, 2003, 108 p.
29. **Karmen Lust.** Adsorption of anions on bismuth single crystal electrodes. Tartu, 2003, 128 p.
30. **Mare Piirsalu.** Substituent, temperature and solvent effects on the alkaline hydrolysis of substituted phenyl and alkyl esters of benzoic acid. Tartu, 2003, 156 p.
31. **Meeri Sassian.** Reactions of partially solvated Grignard reagents. Tartu, 2003, 78 p.
32. **Tarmo Tamm.** Quantum chemical modelling of polypyrrole. Tartu, 2003. 100 p.
33. **Erik Teinemaa.** The environmental fate of the particulate matter and organic pollutants from an oil shale power plant. Tartu, 2003. 102 p.
34. **Jaana Tammiku-Taul.** Quantum chemical study of the properties of Grignard reagents. Tartu, 2003. 120 p.
35. **Andre Lomaka.** Biomedical applications of predictive computational chemistry. Tartu, 2003. 132 p.
36. **Kostyantyn Kirichenko.** Benzotriazole – Mediated Carbon–Carbon Bond Formation. Tartu, 2003. 132 p.
37. **Gunnar Nurk.** Adsorption kinetics of some organic compounds on bismuth single crystal electrodes. Tartu, 2003, 170 p.
38. **Mati Arulepp.** Electrochemical characteristics of porous carbon materials and electrical double layer capacitors. Tartu, 2003, 196 p.
39. **Dan Cornel Fara.** QSPR modeling of complexation and distribution of organic compounds. Tartu, 2004, 126 p.
40. **Riina Mahlapuu.** Signalling of galanin and amyloid precursor protein through adenylate cyclase. Tartu, 2004, 124 p.

41. **Mihkel Kerikmäe.** Some luminescent materials for dosimetric applications and physical research. Tartu, 2004, 143 p.
42. **Jaanus Kruusma.** Determination of some important trace metal ions in human blood. Tartu, 2004, 115 p.
43. **Urmas Johanson.** Investigations of the electrochemical properties of polypyrrole modified electrodes. Tartu, 2004, 91 p.
44. **Kaido Sillar.** Computational study of the acid sites in zeolite ZSM-5. Tartu, 2004, 80 p.
45. **Aldo Oras.** Kinetic aspects of dATPαS interaction with $P2Y_1$ receptor. Tartu, 2004, 75 p.
46. **Erik Mölder.** Measurement of the oxygen mass transfer through the air-water interface. Tartu, 2005, 73 p.
47. **Thomas Thomberg.** The kinetics of electroreduction of peroxodisulfate anion on cadmium (0001) single crystal electrode. Tartu, 2005, 95 p.
48. **Olavi Loog.** Aspects of condensations of carbonyl compounds and their imine analogues. Tartu, 2005, 83 p.
49. **Siim Salmar.** Effect of ultrasound on ester hydrolysis in aqueous ethanol. Tartu, 2006, 73 p.
50. **Ain Uustare.** Modulation of signal transduction of heptahelical receptors by other receptors and G proteins. Tartu, 2006, 121 p.
51. **Sergei Yurchenko.** Determination of some carcinogenic contaminants in food. Tartu, 2006, 143 p.
52. **Kaido Tämm.** QSPR modeling of some properties of organic compounds. Tartu, 2006, 67 p.
53. **Olga Tšubrik.** New methods in the synthesis of multisubstituted hydrazines. Tartu. 2006, 183 p.
54. **Lilli Sooväli.** Spectrophotometric measurements and their uncertainty in chemical analysis and dissociation constant measurements. Tartu, 2006, 125 p.
55. **Eve Koort.** Uncertainty estimation of potentiometrically measured ph and pK_a values. Tartu, 2006, 139 p.
56. **Sergei Kopanchuk.** Regulation of ligand binding to melanocortin receptor subtypes. Tartu, 2006, 119 p.
57. **Silvar Kallip.** Surface structure of some bismuth and antimony single crystal electrodes. Tartu, 2006, 107 p.
58. **Kristjan Saal.** Surface silanization and its application in biomolecule coupling. Tartu, 2006, 77 p.
59. **Tanel Tätte.** High viscosity $Sn(OBu)_4$ oligomeric concentrates and their applications in technology. Tartu, 2006, 91 p.
60. **Dimitar Atanasov Dobchev**. Robust QSAR methods for the prediction of properties from molecular structure. Tartu, 2006, 118 p.
61. **Hannes Hagu**. Impact of ultrasound on hydrophobic interactions in solutions. Tartu, 2007, 81 p.
62. **Rutha Jäger.** Electroreduction of peroxodisulfate anion on bismuth electrodes. Tartu, 2007, 142 p.

63. **Kaido Viht.** Immobilizable bisubstrate-analogue inhibitors of basophilic protein kinases: development and application in biosensors. Tartu, 2007, 88 p.
64. **Eva-Ingrid Rõõm.** Acid-base equilibria in nonpolar media. Tartu, 2007, 156 p.
65. **Sven Tamp.** DFT study of the cesium cation containing complexes relevant to the cesium cation binding by the humic acids. Tartu, 2007, 102 p.
66. **Jaak Nerut.** Electroreduction of hexacyanoferrate(III) anion on Cadmium (0001) single crystal electrode. Tartu, 2007, 180 p.
67. **Lauri Jalukse.** Measurement uncertainty estimation in amperometric dissolved oxygen concentration measurement. Tartu, 2007, 112 p.
68. **Aime Lust.** Charge state of dopants and ordered clusters formation in CaF_2:Mn and CaF_2:Eu luminophors. Tartu, 2007, 100 p.
69. **Iiris Kahn**. Quantitative Structure-Activity Relationships of environmentally relevant properties. Tartu, 2007, 98 p.
70. **Mari Reinik.** Nitrates, nitrites, N-nitrosamines and polycyclic aromatic hydrocarbons in food: analytical methods, occurrence and dietary intake. Tartu, 2007, 172 p.
71. **Heili Kasuk.** Thermodynamic parameters and adsorption kinetics of organic compounds forming the compact adsorption layer at Bi single crystal electrodes. Tartu, 2007, 212 p.
72. **Erki Enkvist.** Synthesis of adenosine-peptide conjugates for biological applications. Tartu, 2007, 114 p.
73. **Svetoslav Hristov Slavov**. Biomedical applications of the QSAR approach. Tartu, 2007, 146 p.
74. **Eneli Härk.** Electroreduction of complex cations on electrochemically polished Bi(*hkl*) single crystal electrodes. Tartu, 2008, 158 p.
75. **Priit Möller.** Electrochemical characteristics of some cathodes for medium temperature solid oxide fuel cells, synthesized by solid state reaction technique. Tartu, 2008, 90 p.
76. **Signe Viggor.** Impact of biochemical parameters of genetically different pseudomonads at the degradation of phenolic compounds. Tartu, 2008, 122 p.
77. **Ave Sarapuu.** Electrochemical reduction of oxygen on quinone-modified carbon electrodes and on thin films of platinum and gold. Tartu, 2008, 134 p.
78. **Agnes Kütt.** Studies of acid-base equilibria in non-aqueous media. Tartu, 2008, 198 p.
79. **Rouvim Kadis.** Evaluation of measurement uncertainty in analytical chemistry: related concepts and some points of misinterpretation. Tartu, 2008, 118 p.
80. **Valter Reedo.** Elaboration of IVB group metal oxide structures and their possible applications. Tartu, 2008, 98 p.
81. **Aleksei Kuznetsov.** Allosteric effects in reactions catalyzed by the cAMP-dependent protein kinase catalytic subunit. Tartu, 2009, 133 p.

82. **Aleksei Bredihhin.** Use of mono- and polyanions in the synthesis of multisubstituted hydrazine derivatives. Tartu, 2009, 105 p.
83. **Anu Ploom.** Quantitative structure-reactivity analysis in organosilicon chemistry. Tartu, 2009, 99 p.
84. **Argo Vonk.** Determination of adenosine A_{2A}- and dopamine D_1 receptor-specific modulation of adenylate cyclase activity in rat striatum. Tartu, 2009, 129 p.
85. **Indrek Kivi.** Synthesis and electrochemical characterization of porous cathode materials for intermediate temperature solid oxide fuel cells. Tartu, 2009, 177 p.
86. **Jaanus Eskusson.** Synthesis and characterisation of diamond-like carbon thin films prepared by pulsed laser deposition method. Tartu, 2009, 117 p.
87. **Marko Lätt.** Carbide derived microporous carbon and electrical double layer capacitors. Tartu, 2009, 107 p.
88. **Vladimir Stepanov.** Slow conformational changes in dopamine transporter interaction with its ligands. Tartu, 2009, 103 p.
89. **Aleksander Trummal.** Computational Study of Structural and Solvent Effects on Acidities of Some Brønsted Acids. Tartu, 2009, 103 p.
90. **Eerold Vellemäe.** Applications of mischmetal in organic synthesis. Tartu, 2009, 93 p.
91. **Sven Parkel.** Ligand binding to 5-HT_{1A} receptors and its regulation by Mg^{2+} and Mn^{2+}. Tartu, 2010, 99 p.
92. **Signe Vahur.** Expanding the possibilities of ATR-FT-IR spectroscopy in determination of inorganic pigments. Tartu, 2010, 184 p.
93. **Tavo Romann**. Preparation and surface modification of bismuth thin film, porous, and microelectrodes. Tartu, 2010, 155 p.
94. **Nadežda Aleksejeva.** Electrocatalytic reduction of oxygen on carbon nanotube-based nanocomposite materials. Tartu, 2010, 147 p.
95. **Marko Kullapere.** Electrochemical properties of glassy carbon, nickel and gold electrodes modified with aryl groups. Tartu, 2010, 233 p.
96. **Liis Siinor.** Adsorption kinetics of ions at Bi single crystal planes from aqueous electrolyte solutions and room-temperature ionic liquids. Tartu, 2010, 101 p.
97. **Angela Vaasa.** Development of fluorescence-based kinetic and binding assays for characterization of protein kinases and their inhibitors. Tartu 2010, 101 p.
98. **Indrek Tulp.** Multivariate analysis of chemical and biological properties. Tartu 2010, 105 p.
99. **Aare Selberg.** Evaluation of environmental quality in Northern Estonia by the analysis of leachate. Tartu 2010, 117 p.
100. **Darja Lavõgina.** Development of protein kinase inhibitors based on adenosine analogue-oligoarginine conjugates. Tartu 2010, 248 p.
101. **Laura Herm.** Biochemistry of dopamine D_2 receptors and its association with motivated behaviour. Tartu 2010, 156 p.

102. **Terje Raudsepp.** Influence of dopant anions on the electrochemical properties of polypyrrole films. Tartu 2010, 112 p.
103. **Margus Marandi.** Electroformation of Polypyrrole Films: *In-situ* AFM and STM Study. Tartu 2011, 116 p.
104. **Kairi Kivirand.** Diamine oxidase-based biosensors: construction and working principles. Tartu, 2011, 140 p.
105. **Anneli Kruve.** Matrix effects in liquid-chromatography electrospray mass-spectrometry. Tartu, 2011, 156 p.
106. **Gary Urb.** Assessment of environmental impact of oil shale fly ash from PF and CFB combustion. Tartu, 2011, 108 p.
107. **Nikita Oskolkov.** A novel strategy for peptide-mediated cellular delivery and induction of endosomal escape. Tartu, 2011, 106 p.
108. **Dana Martin.** The QSPR/QSAR approach for the prediction of properties of fullerene derivatives. Tartu, 2011, 98 p.
109. **Säde Viirlaid.** Novel glutathione analogues and their antioxidant activity. Tartu, 2011, 106 p.
110. **Ülis Sõukand.** Simultaneous adsorption of Cd^{2+}, Ni^{2+}, and Pb^{2+} on peat. Tartu, 2011, 124 p.
111. **Lauri Lipping.** The acidity of strong and superstrong Brønsted acids, an outreach for the "limits of growth": a quantum chemical study. Tartu, 2011, 124 p.
112. **Heisi Kurig.** Electrical double-layer capacitors based on ionic liquids as electrolytes. Tartu, 2011, 146 p.
113. **Marje Kasari.** Bisubstrate luminescent probes, optical sensors and affinity adsorbents for measurement of active protein kinases in biological samples. Tartu, 2012, 126 p.
114. **Kalev Takkis.** Virtual screening of chemical databases for bioactive molecules. Tartu, 2012, 122 p.
115. **Ksenija Kisseljova**. Synthesis of aza-β^3-amino acid containing peptides and kinetic study of their phosphorylation by protein kinase A. Tartu, 2012, 104 p.
116. **Riin Rebane.** Advanced method development strategy for derivatization LC/ESI/MS. Tartu, 2012, 184 p.
117. **Vladislav Ivaništšev.** Double layer structure and adsorption kinetics of ions at metal electrodes in room temperature ionic liquids. Tartu, 2012, 128 p.
118. **Irja Helm.** High accuracy gravimetric Winkler method for determination of dissolved oxygen. Tartu, 2012, 139 p.
119. **Karin Kipper.** Fluoroalcohols as Components of LC-ESI-MS Eluents: Usage and Applications. Tartu, 2012, 164 p.
120. **Arno Ratas.** Energy storage and transfer in dosimetric luminescent materials. Tartu, 2012, 163 p.
121. **Reet Reinart-Okugbeni**. Assay systems for characterisation of subtype-selective binding and functional activity of ligands on dopamine receptors. Tartu, 2012, 159 p.

122. **Lauri Sikk.** Computational study of the Sonogashira cross-coupling reaction. Tartu, 2012, 81 p.
123. **Karita Raudkivi.** Neurochemical studies on inter-individual differences in affect-related behaviour of the laboratory rat. Tartu, 2012, 161 p.
124. **Indrek Saar.** Design of GalR2 subtype specific ligands: their role in depression-like behavior and feeding regulation. Tartu, 2013, 126 p.
125. **Ann Laheäär.** Electrochemical characterization of alkali metal salt based non-aqueous electrolytes for supercapacitors. Tartu, 2013, 127 p.
126. **Kerli Tõnurist.** Influence of electrospun separator materials properties on electrochemical performance of electrical double-layer capacitors. Tartu, 2013, 147 p.
127. **Kaija Põhako-Esko.** Novel organic and inorganic ionogels: preparation and characterization. Tartu, 2013, 124 p.
128. **Ivar Kruusenberg.** Electroreduction of oxygen on carbon nanomaterial-based catalysts. Tartu, 2013, 191 p.
129. **Sander Piiskop.** Kinetic effects of ultrasound in aqueous acetonitrile solutions. Tartu, 2013, 95 p.
130. **Ilona Faustova**. Regulatory role of L-type pyruvate kinase N-terminal domain. Tartu, 2013, 109 p.
131. **Kadi Tamm.** Synthesis and characterization of the micro-mesoporous anode materials and testing of the medium temperature solid oxide fuel cell single cells. Tartu, 2013, 138 p.
132. **Iva Bozhidarova Stoyanova-Slavova.** Validation of QSAR/QSPR for regulatory purposes. Tartu, 2013, 109 p.
133. **Vitali Grozovski**. Adsorption of organic molecules at single crystal electrodes studied by *in situ* STM method. Tartu, 2014, 146 p.
134. **Santa Veikšina**. Development of assay systems for characterisation of ligand binding properties to melanocortin 4 receptors. Tartu, 2014, 151 p.
135. **Jüri Liiv.** PVDF (polyvinylidene difluoride) as material for active element of twisting-ball displays. Tartu, 2014, 111 p.
136. **Kersti Vaarmets.** Electrochemical and physical characterization of pristine and activated molybdenum carbide-derived carbon electrodes for the oxygen electroreduction reaction. Tartu, 2014, 131 p.
137. **Lauri Tõntson**. Regulation of G-protein subtypes by receptors, guanine nucleotides and Mn^{2+}. Tartu, 2014, 105 p.
138. **Aiko Adamson.** Properties of amine-boranes and phosphorus analogues in the gas phase. Tartu, 2014, 78 p.
139. **Elo Kibena**. Electrochemical grafting of glassy carbon, gold, highly oriented pyrolytic graphite and chemical vapour deposition-grown graphene electrodes by diazonium reduction method. Tartu, 2014, 184 p.
140. **Teemu Näykki.** Novel Tools for Water Quality Monitoring – From Field to Laboratory. Tartu, 2014, 202 p.
141. **Karl Kaupmees.** Acidity and basicity in non-aqueous media: importance of solvent properties and purity. Tartu, 2014, 128 p.

142. **Oleg Lebedev**. Hydrazine polyanions: different strategies in the synthesis of heterocycles. Tartu, 2015, 118 p.
143. **Geven Piir.** Environmental risk assessment of chemicals using QSAR methods. Tartu, 2015, 123 p.
144. **Olga Mazina.** Development and application of the biosensor assay for measurements of cyclic adenosine monophosphate in studies of G protein-coupled receptor signalinga. Tartu, 2015, 116 p.
145. **Sandip Ashokrao Kadam.** Anion receptors: synthesis and accurate binding measurements. Tartu, 2015, 116 p.
146. **Indrek Tallo.** Synthesis and characterization of new micro-mesoporous carbide derived carbon materials for high energy and power density electrical double layer capacitors. Tartu, 2015, 148 p.
147. **Heiki Erikson.** Electrochemical reduction of oxygen on nanostructured palladium and gold catalysts. Tartu, 2015, 204 p.
148. **Erik Anderson.** *In situ* Scanning Tunnelling Microscopy studies of the interfacial structure between Bi(111) electrode and a room temperature ionic liquid. Tartu, 2015, 118 p.
149. **Girinath G. Pillai.** Computational Modelling of Diverse Chemical, Biochemical and Biomedical Properties. Tartu, 2015, 140 p.
150. **Piret Pikma.** Interfacial structure and adsorption of organic compounds at Cd(0001) and Sb(111) electrodes from ionic liquid and aqueous electrolytes: an *in situ* STM study. Tartu, 2015, 126 p.
151. **Ganesh babu Manoharan.** Combining chemical and genetic approaches for photoluminescence assays of protein kinases. Tartu, 2016, 126 p.
152. **Carolin Siimenson**. Electrochemical characterization of halide ion adsorption from liquid mixtures at Bi(111) and pyrolytic graphite electrode surface. Tartu, 2016, 110 p.
153. **Asko Laaniste.** Comparison and optimisation of novel mass spectrometry ionisation sources. Tartu, 2016, 156 p.
154. **Hanno Evard.** Estimating limit of detection for mass spectrometric analysis methods. Tartu, 2016, 224 p.
155. **Kadri Ligi.** Characterization and application of protein kinase-responsive organic probes with triplet-singlet energy transfer. Tartu, 2016, 122 p.
156. **Margarita Kagan.** Biosensing penicillins' residues in milk flows. Tartu, 2016, 130 p.
157. **Marie Kriisa.** Development of protein kinase-responsive photoluminescent probes and cellular regulators of protein phosphorylation. Tartu, 2016, 106 p.
158. **Mihkel Vestli.** Ultrasonic spray pyrolysis deposited electrolyte layers for intermediate temperature solid oxide fuel cells. Tartu, 2016, 156 p.
159. **Silver Sepp**. Influence of porosity of the carbide-derived carbon on the properties of the composite electrocatalysts and characteristics of polymer electrolyte fuel cells. Tartu, 2016, 137 p.
160. **Kristjan Haav**. Quantitative relative equilibrium constant measurements in supramolecular chemistry. Tartu, 2017, 158 p.

161. **Anu Teearu**. Development of MALDI-FT-ICR-MS methodology for the analysis of resinous materials. Tartu, 2017, 205 p.
162. **Taavi Ivan**. Bifunctional inhibitors and photoluminescent probes for studies on protein complexes. Tartu, 2017, 140 p.
163. **Maarja-Liisa Oldekop**. Characterization of amino acid derivatization reagents for LC-MS analysis. Tartu, 2017, 147 p.
164. **Kristel Jukk**. Electrochemical reduction of oxygen on platinum- and palladium-based nanocatalysts. Tartu, 2017, 250 p.
165. **Siim Kukk**. Kinetic aspects of interaction between dopamine transporter and *N*-substituted nortropane derivatives. Tartu, 2017, 107 p.
166. **Birgit Viira**. Design and modelling in early drug development in targeting HIV-1 reverse transcriptase and Malaria. Tartu, 2017, 172 p.
167. **Rait Kivi**. Allostery in cAMP dependent protein kinase catalytic subunit. Tartu, 2017, 115 p.
168. **Agnes Heering**. Experimental realization and applications of the unified acidity scale. Tartu, 2017, 123 p.
169. **Delia Juronen**. Biosensing system for the rapid multiplex detection of mastitis-causing pathogens in milk. Tartu, 2018, 85 p.
170. **Hedi Rahnel.** ARC-inhibitors: from reliable biochemical assays to regulators of physiology of cells. Tartu, 2018, 176 p.
171. **Anton Ruzanov.** Computational investigation of the electrical double layer at metal–aqueous solution and metal–ionic liquid interfaces. Tartu, 2018, 129 p.
172. **Katrin Kestav.** Crystal Structure-Guided Development of Bisubstrate-Analogue Inhibitors of Mitotic Protein Kinase Haspin. Tartu, 2018, 166 p.
173. **Mihkel Ilisson.** Synthesis of novel heterocyclic hydrazine derivatives and their conjugates. Tartu, 2018, 101 p.
174. **Anni Allikalt.** Development of assay systems for studying ligand binding to dopamine receptors. Tartu, 2018, 160 p.
175. **Ove Oll.** Electrical double layer structure and energy storage characteristics of ionic liquid based capacitors. Tartu, 2018, 187 p.
176. **Rasmus Palm.** Carbon materials for energy storage applications. Tartu, 2018, 114 p.
177. **Jörgen Metsik.** Preparation and stability of poly(3,4-ethylenedioxythiophene) thin films for transparent electrode applications. Tartu, 2018, 111 p.
178. **Sofja Tšepelevitš.** Experimental studies and modeling of solute-solvent interactions. Tartu, 2018, 109 p.
179. **Märt Lõkov.** Basicity of some nitrogen, phosphorus and carbon bases in acetonitrile. Tartu, 2018, 104 p.
180. **Anton Mastitski**. Preparation of α-aza-amino acid precursors and related compounds by novel methods of reductive one-pot alkylation and direct alkylation. Tartu, 2018, 155 p.
181. **Jürgen Vahter**. Development of bisubstrate inhibitors for protein kinase CK2. Tartu, 2019, 186 p.

182. **Piia Liigand.** Expanding and improving methodology and applications of ionization efficiency measurements. Tartu, 2019, 189 p.
183. **Sigrid Selberg.** Synthesis and properties of lipophilic phosphazene-based indicator molecules. Tartu, 2019, 74 p.
184. **Jaanus Liigand.** Standard substance free quantification for LC/ESI/MS analysis based on the predicted ionization efficiencies. Tartu, 2019, 254 p.
185. **Marek Mooste.** Surface and electrochemical characterisation of aryl film and nanocomposite material modified carbon and metal-based electrodes. Tartu, 2019, 304 p.
186. **Mare Oja.** Experimental investigation and modelling of pH profiles for effective membrane permeability of drug substances. Tartu, 2019, 306 p.
187. **Sajid Hussain.** Electrochemical reduction of oxygen on supported Pt catalysts. Tartu, 2019, 220 p.
188. **Ronald Väli.** Glucose-derived hard carbon electrode materials for sodium-ion batteries. Tartu, 2019, 180 p.
189. **Ester Tee.** Analysis and development of selective synthesis methods of hierarchical micro- and mesoporous carbons. Tartu, 2019, 210 p.
190. **Martin Maide.** Influence of the microstructure and chemical composition of the fuel electrode on the electrochemical performance of reversible solid oxide fuel cell. Tartu, 2020, 144 p.
191. **Edith Viirlaid.** Biosensing Pesticides in Water Samples. Tartu, 2020, 102 p.
192. **Maike Käärik.** Nanoporous carbon: the controlled nanostructure, and structure-property relationships. Tartu, 2020, 162 p.
193. **Artur Gornischeff.** Study of ionization efficiencies for derivatized compounds in LC/ESI/MS and their application for targeted analysis. Tartu, 2020, 124 p.
194. **Reet Link.** Ligand binding, allosteric modulation and constitutive activity of melanocortin-4 receptors. Tartu, 2020, 108 p.
195. **Pilleriin Peets.** Development of instrumental methods for the analysis of textile fibres and dyes. Tartu, 2020, 150 p.
196. **Larisa Ivanova.** Design of active compounds against neurodegenerative diseases. Tartu, 2020, 152 p.
197. **Meelis Härmas.** Impact of activated carbon microstructure and porosity on electrochemical performance of electrical double-layer capacitors. Tartu, 2020, 122 p.
198. **Ruta Hecht.** Novel Eluent Additives for LC-MS Based Bioanalytical Methods. Tartu, 2020, 202 p.
199. **Max Hecht.** Advances in the Development of a Point-of-Care Mass Spectrometer Test. Tartu, 2020, 168 p.
200. **Ida Rahu.** Bromine formation in inorganic bromide/nitrate mixtures and its application for oxidative aromatic bromination. Tartu, 2020, 116 p.
201. **Sander Ratso**. Electrocatalysis of oxygen reduction on non-precious metal catalysts. Tartu, 2020, 371 p.
202. **Astrid Darnell.** Computational design of anion receptors and evaluation of host-guest binding. Tartu, 2021, 150 p.

203. **Ove Korjus.** The development of ceramic fuel electrode for solid oxide cells. Tartu, 2021, 150 p.
204. **Merit Oss.** Ionization efficiency in electrospray ionization source and its relations to compounds' physico-chemical properties. Tartu, 2021, 124 p.
205. **Madis Lüsi**. Electroreduction of oxygen on nanostructured palladium catalysts. Tartu, 2021, 180 p.
206. **Eliise Tammekivi.** Derivatization and quantitative gas-chromatographic analysis of oils. Tartu, 2021, 122 p.
207. **Simona Selberg.** Development of Small-Molecule Regulators of Epi-transcriptomic Processes. Tartu, 2021, 122 p.
208. **Olivier Etebe Nonga.** Inhibitors and photoluminescent probes for in vitro studies on protein kinases PKA and PIM. Tartu, 2021, 189 p.
209. **Riinu Härmas.** The structure and H2 diffusion in porous carbide-derived carbon particles. Tartu, 2022, 123 p.
210. **Maarja Paalo.** Synthesis and characterization of novel carbon electrodes for high power density electrochemical capacitors. Tartu, 2022, 144 p.
211. **Jinfeng Zhao.** Electrochemical characteristics of Bi(hkl) and micro-meso-porous carbon electrodes in ionic liquid based electrolytes. Tartu, 2022, 134 p.
212. **Alar Heinsaar.** Investigation of oxygen electrode materials for high-temperature solid oxide cells in natural conditions. Tartu, 2022, 120 p.
213. **Jaana Lilloja.** Transition metal and nitrogen doped nanocarbon cathode catalysts for anion exchange membrane fuel cells. Tartu, 2022, 202 p.
214. **Maris-Johanna Tahk.** Novel fluorescence-based methods for illuminating transmembrane signal transduction by G-protein coupled receptors. Tartu, 2022, 200 p.
215. **Eerik Jõgi.** Development and Applications of E. coli Immunosensor. Tartu, 2022, 103 p.
216. **Alo Rüütel.** Design principles of synthetic molecular receptors for anion-selective electrodes. Tartu, 2022, 109 p.
217. **Tanel Sõrmus.** Development of stimuli-responsive and covalent bisubstrate inhibitors of protein kinases. Tartu, 2022, 148 p.
218. **Oleg Artemchuk.** Autotrophic nitrogen removal processes for nutrient removal from sidestream and mainstream wastewater. Tartu, 2022, 115 p.
219. **Andre Leesment.** Quantitative studies of Brønsted acidity in biphasic systems and gas-phase. Tartu, 2023, 83 p.
220. **Meeli Arujõe-Sado.** Structural effects in aza-peptide bond formation reaction. Tartu, 2023, 83 p.
221. **Jonas Mart Linge.** Electrochemical reduction of oxygen on silver-based catalysts. Tartu, 2023, 269 p.
222. **Tõnis Laasfeld.** Integrating Image Analysis and Quantitative Modeling for a Holistic View of GPCR Ligand Binding Dynamics. Tartu, 2023, 226 p.
223. **Ernesto de Jesus Zapata Flores.** Derivatization Reagents used in negative mode electrospray LC-MS. Tartu, 2023, 107 p.

224. **Patrick Teppor.** Obtaining platinum-free oxygen reduction catalysts through biomass valorization: a case study of peat. Tartu, 2023, 161 p.
225. **Peeter Valk.** Methanol Oxidation on Platinum-Rare-Earth Metal Oxide Activated Catalysts. Tartu, 2023, 162 p.
226. **Shidong Chen.** Unravelling prehistoric plant exploitation in eastern Baltic: organic residue analysis of plant-based materials by multi-method approach. Tartu, 2023, 245 p.